ISTANBUL TECHNICAL UNIVERSITY
ELECTRICAL-ELECTRONICS FACULTY

MONITORING OF BRAIN WITH MICROWAVE IMAGING

SENIOR DESIGN PROJECT

Burak Erdil BİÇER
Nahid GUDRATLİ
Vurghun AHMADOV

ELECTRONICS AND COMMUNICATION ENGINEERING DEPARTMENT

JUNE 2025

ISTANBUL TECHNICAL UNIVERSITY
ELECTRICAL-ELECTRONICS FACULTY

MONITORING OF BRAIN WITH MICROWAVE IMAGING

SENIOR DESIGN PROJECT

Burak Erdil BİÇER
(040200208)

Nahid GUDRATLİ
(040200930)

Vurghun AHMADOV
(040210921)

ELECTRONICS AND COMMUNICATION ENGINEERING DEPARTMENT

Project Advisor: Prof. Dr. Mehmet ÇAYÖREN

JUNE 2025

İSTANBUL TEKNİK ÜNİVERSİTESİ
ELEKTRİK-ELEKTRONİK FAKÜLTESİ

MİKRODALGA GÖRÜNTÜLEME İLE BEYİNİN İZLENMESİ

LİSANS BİTİRME TASARIM PROJESİ

Burak Erdil BİÇER
(040200208)

Nahid GUDRATLİ
(040200930)

Vurghun AHMADOV
(040210921)

Proje Danışmanı: Prof. Dr. Mehmet ÇAYÖREN

ELEKTRONİK VE HABERLEŞME MÜHENDİSLİĞİ BÖLÜMÜ

HAZİRAN, 2025

We are submitting the Senior Design Project Report entitled as “MONITORING OF BRAIN WITH MICROWAVE IMAGING”. The Senior Design Project Report has been prepared as to fulfill the relevant regulations of the Electronics and Communication Engineering Department of Istanbul Technical University. We hereby confirm that we have realized all stages of the Senior Design Project work by ourselves and we have abided by the ethical rules with respect to academic and professional integrity .

Burak Erdil BİÇER .....
(040200208)

Nahid GUDRATLİ .....
(040200930)

Vurghun AHMADOV .....
(040210921)

FOREWORD

We are pleased to present this report of the project titled Monitoring of Brain with Microwave Imaging. This project reflects the enthusiasm and effort of the student team to design a new solution for monitoring the brain. We would like to thank Prof. Dr. Mehmet Çayören for the valuable guidance throughout the entire project. His advice played an important role in deciding the research and development path. We also sincerely appreciate the facilities and technical support by the Medical Devices Research Development and Application Laboratory that allowed us to carry out this research.

June 2025

Burak Erdil BİÇER
Nahid GUDRATLİ
Vurghun AHMADOV

TABLE OF CONTENTS

Page

ABBREVIATIONS

CT	**:** Computed Tomography
DBIM	**:** Distorted Born Iterative Method
DMI	**:** Differential Microwave Imaging
FEM	**:** Finite Element Method
FM	**:** Factorization Method
HFSS	**:** High-Frequency Structure Simulator
IEC	**:** International Electrotechnical Commission
IEEE	**:** Institute of Electrical and Electronics Engineers
IPC	**:** Association Connecting Electronics Industries
ISO	**:** International Organization for Standardization
ITU	**:** International Telecommunication Union
LSM	**:** Linear Sampling Method
MRI	**:** Magnetic Resonance Imaging
PCB	**:** Printed Circuit Board
RF	**:** Radio Frequency
SMA	**:** SubMiniature version A (coax connector)
SVD	**:** Singular Value Decomposition
TSVD	**:** Truncated Singular Value Decomposition
TWI	**:** Through-the-Wall Imaging
VNA	**:** Vector Network Analyzer

SYMBOLS

χ	: Contrast source (electric contrast function)
Δ	: Increment / difference operator
δ	: Dirac delta / small perturbation
ε	: Permittivity
ε_r	: Relative permittivity
λ	: Wavelength in medium
λ_0	: Free-space wavelength
μ	: Permeability
μ_0	: Permeability of free space
π	: Archimedes' constant (≈ 3.1416)
Σ	: Summation / covariance matrix
σ	: Electrical conductivity
Ω	: Domain / solid angle (imaging region)
k	: Wavenumber in medium
k_0	: Free-space wavenumber
k_α	: TSVD truncation index
E	: Total electric-field
$E_{\mathbf{inc}}$	: Incident electric-field at a point
$E_{\mathbf{scat}}$	: Scattered electric-field at a point
G	: Green's function
V	: Volume of the scattering region
u_t	: Total field in Helmholtz formulation
u_i	: Incident field
u_s	: Scattered field
p	: Observation point or receiver location (in 2D)
r	: Radial coordinate
r'	: Source coordinate in integral equations
z	: Cartesian z-coordinate (or spatial point in 2D)
t	: Time
A	: System matrix
x	: Unknown image (contrast) vector
b	: Measured data (scattered-field) vector
U	: Left singular-vector matrix (orthonormal)
V	: Right singular-vector matrix (orthonormal)
σ_i	: ith singular value (diagonal entry of Σ)
u_i	: ith left singular vector (column of U)
v_i	: ith right singular vector (column of V)
L	: Sensing (forward-model) matrix constructed from Green's functions
χ	: Object contrast vector
g	: Green's function in 2D
$H_0^{(2)}$	: Zero-order second-kind Hankel function (Green's function kernel)

Δz	: Differential mesh element thickness (volume element in 2D)
χ_R	: Reconstructed contrast via TSVD
$I(x,y)$	: Normalized magnitude image from TSVD (before smoothing)
$G_\sigma(x,y)$	: Gaussian kernel with standard deviation σ
$I_s(x,y)$	: Smoothed image ($I_s = I * G_\sigma$)
σ	: Standard deviation
p	: Percentile value for adaptive threshold
T_p	: Threshold value corresponding to percentile p
B	: Binary mask after thresholding
S_r	: Circular structuring element of radius r for morphological opening/closing
B_c	: Cleaned mask after morphological opening and closing
C_i	: ith connected component in B_c (labeled region)
A_i	: Area (pixel count) of component C_i
$C_{\max}$	: Largest connected-component in B_c
$A_{\min}$	: Minimum area threshold for component preservation
C_i	: Simulation case label
S_i	: Clinical scenario label
dB	: Decibel
dBm	: Decibel-milliwatts
mW	: Milliwatt
MHz	: Megahertz
cm	: Centimeter
mm	: Millimeter

LIST OF TABLES

Page

LIST OF FIGURES

Page

SUMMARY

This study deals with the design of a portable and low-cost microwave imaging system without ionizing radiation in a simulation environment. The ultimate goal of the project is to enable continuous and reliable monitoring of cerebral hemorrhages such as trauma or stroke under bedside conditions in hospitals or emergency rooms. To this end, the main components of the system design, the data processing algorithms and finally the findings are discussed in detail.

At the beginning of the project, a comprehensive work plan was prepared including antenna design, creation of a suitable brain phantom, acquisition of microwave measurements and image reconstruction in simulation environment. After each antenna optimization cycle performed on the HFSS software, the work plan was reviewed and updated as necessary. This flexible approach not only saved time but also ensured the most efficient use of available resources. In the literature review, the disadvantages of existing imaging modalities (Computed Tomography (CT), Magnetic Resonance (MR), etc.) such as portability and cost were emphasized, and the potential of microwaves to provide dielectric contrast-based, portable solutions was highlighted.

The main method started with the design and optimization of a circular antenna array of sixteen dipoles operating at 900 MHz in the HFSS simulation environment. The dimensions, placement angles and feed spacing of the dipole antennas were determined by avoiding mutual coupling. Matching media with different dielectric constants were tested to maximize the signal penetration into the tissue and to keep the back reflections (S_{11}) below 10 dB. By examining the S-parameter values given by these media, the most suitable matching medium for our application was determined and antenna designs operating at 900 MHz were tested in accordance with this matching medium. Here, the size of the dielectric coefficient is inversely proportional to the length of the dipole antenna, which determines the antenna dimensions operating at the desired operating frequency. The antenna radius was also rearranged by considering the bandwidth. Furthermore, the dielectric properties of this medium minimized reflections at the antenna-phantom interface and increased the transmitter/receiver coupling. Thus, the reliability and reconstruction quality of the acquired signal are significantly improved.

In the data collection phase, S-parameter data from the HFSS was used instead of real hardware. Initial experimental simulations considered two different cases: a healthy brain and a case with a hemorrhage (lesion) in the brain. Separate sets of S-parameters for different bleeding scenarios (single bleeding, growing bleeding, time-dependent bleeding growth, multiple bleeding and additional new lesion) were generated and used as the basis for the data processing algorithms. Thus, system performance and limitations could be systematically analyzed without taking actual measurements.

The inverse scattering problem linearized by the Born approximation is solved in the form $L\chi = b$ on a cartesian grid of size 128×128 in the phase of image reconstruction. Stable solution of this ill-posed system is obtained using the Truncated Singular Value Decomposition (TSVD) approach. Furthermore, the benefits of this approach over the Singular Value Decomision (SVD) approach are covered. It was decided to preserve the mode $k_\alpha = 52$ for non-conducting (lossless) brain models and $k_\alpha = 33$ under realistic conductivity by analyzing the "elbow point" in the TSVD spectrum. Furthermore, these values were found using an interactive interface whereby the user may see how the cut-off point affects the imaging results. Eliminating high-order noise components maximized the information contents. Moreover, a four-stage noise filter chain (skull mask, Gaussian smoothing, adaptive thresholding and morphological cleaning) cut the noise in the generated maps. The intention was to let users view lesion points more precisely.

According to the results, the microwave signal is attenuated by more than 99% in the tissue and only a fraction of the transmitted power reaches the receiving antennas when the brain tissue has realistic conductivity ($\sigma = 0{,}9\,\mathrm{S/m}$). Under these conditions, strong noise dominated the images acquired with the TSVD technique, so drastically lowering the contrast of the lesions. In contrast, in simulations with zero conductivity (lossless), both energy transfer was complete and clear maps were obtained, with hemorrhage contours and foci clearly distinguishable. One major restriction to the clinical relevance of the method was observed as the inability to consistently identify small or deep lesions at reasonable conductivity.

All bleeding foci could be effectively localized in lossless models during the tests on five various clinical scenarios derived from four different conditions; even the smallest lesion was found by TSVD. The TSVD intensity was observed to spread in the field as the lesion diameter grew, suggesting a quantitative means of monitoring bleeding evolution over time. On the realistic conductivity condition, however, small and deep bleeding was visualized with noise while only near-surface and large foci were clearly visible.

These results imply that before the system can be totally used in clinical practice, several developments are required. Specifically, the number of antennas should be raised, horizontal and vertical polarizations should be added and antenna design should be changed in response to intra-tissue losses; different antenna types should be tested; lower operating frequencies should be used; iterative, non-linear algorithms or deep learning-based noise reduction methods should be integrated. In addition, additional equipment such as a multi-port vector network analyzer, an automatic switching matrix and a helmet with tunable dielectric properties, as well as regulatory compliance, will be needed when the actual hardware testing begins.

In short, the study showed that, with the optimal antenna array, suitable matching environment, and TSVD-based inverse solution algorithm, detection of intracranial hemorrhages by differential microwave imaging is feasible even though it was carried out only in a simulation environment. Together with upcoming hardware and algorithmic enhancements, this method provides the foundation for portable devices fit for real-time and bedside monitoring of cerebral hemorrhage.

ÖZET

Bu çalışma, iyonlaştırıcı radyasyon içermeyen, taşınabilir ve düşük maliyetli bir mikrodalga görüntüleme sisteminin simülasyon ortamında tasarlanmasını konu alır. Projenin nihai amacı, travma veya inme gibi beyin kanamalarının, hastanelerde veya acil servislerde yatak başı koşullarda sürekli ve güvenilir biçimde izlenebilmesidir. Bu doğrultuda; öncelikle sistem tasarımının ana bileşenleri, ardından veri işleme algoritmaları ve son olarak elde edilen bulgular detaylı şekilde ele alınmıştır.

Proje başlangıcında, anten dizaynı, uygun beyin fantomu oluşturulması, mikrodalga ölçümlerinin elde edilmesi ve simülasyon ortamında görüntü rekonstrüksiyonu adımlarını içeren kapsamlı bir iş planı hazırlanmıştır. HFSS yazılımı üzerinde gerçekleştirilen her anten optimizasyon döngüsünden sonra iş planı tekrar gözden geçirilmiş ve gerektiğinde güncellenmiştir. Bu esnek yaklaşım sayesinde hem zamandan tasarruf edilmiş hem de eldeki kaynakların en verimli biçimde kullanılması sağlanmıştır. Literatür taramasında ise, mevcut görüntüleme modalitelerinin (Bilgisayarlı Tomografi (BT), Manyetik Rezonans (MR) vb.) taşınabilirlik ve maliyet gibi dezavantajlarına vurgu yapılmış; mikrodalgaların dielektrik kontrast tabanlı, taşınabilir çözümler sunabilme potansiyeli ön plana çıkarılmıştır.

Ana yöntem, HFSS simülasyon ortamında 900 MHz'de çalışan, on altı dipolden oluşan dairesel bir anten dizisinin tasarlanıp optimize edilmesiyle başlamıştır. Dipol antenlerin boyutları, yerleşim açıları ve besleme aralıkları karşılıklı kuplaja girmemesine dikkat edilerek belirlenmiş; sinyalin dokuya maksimum düzeyde geçebilmesi ve sistemde geri yansımaların (S_{11}) -10 dB'nin altında tutulabilmesi için farklı dielektrik sabitlerine sahip eşleştirme ortamları denenmiştir. Bu ortamların vermiş olduğu S-parametre değerleri incelenerek uygulamamıza en uygun olan eşleştirme ortamı belirlenmiş, bu eşleştirme ortamına uygun 900 MHz'de çalışan anten tasarımları denenmiştir. Burada dielektrik katsayısının büyüklüğünün dipol antenin uzunluğuyla ters orantılı olması durumuyla istenilen çalışma frekansında çalışan anten boyutları belirlenmiştir. Anten yarıçapı da bant genişliği göz önünde bulundurularak yeniden düzenlenmştir. Ayrıca, bu ortamın dielektrik özellikleri anten-fantom arayüzünde yansımaları en aza indirgemiş ve verici/alıcı kuplajını artırmıştır. Böylece, elde edilen sinyalin güvenilirliği ve rekonstrüksiyon kalitesi anlamlı ölçüde iyileştirilmiştir.

Veri toplama aşamasında, gerçek donanım yerine, HFSS üzerinden elde edilen S-parametre verileri kullanılmıştır. İlk başta gerçekleştirilen deneme simülasyonlarda iki farklı durum ele alınmıştır: sağlıklı beyin ve beyin içinde kanama (lezyon) bulunan durum. Farklı kanama senaryoları için (tekli kanama, büyüyen kanama, zamana bağlı kanamanın büyümesi, çoklu kanama ve ek yeni lezyon) ayrı ayrı S-parametre kümeleri oluşturulmuş ve veri işleme algoritmalarına temel teşkil etmiştir. Böylece, gerçek

ölçüm alınmadan da sistem performansı ve sınırlamaları sistematik biçimde analiz edilebilmiştir.

Görüntü rekonstrüksiyon aşamasında, Born yaklaşımı ile doğrusal hale getirilen ters saçılma problemi 128×128 boyutunda bir kartesyen ızgara üzerinde $L\chi = b$ formunda çözülmüştür. Kötü koşullanmış (ill-posed) bu sistemin istikrarlı biçimde çözülebilmesi için Kesilmiş Tekil Değer Ayrışımı (TSVD) yöntemi kullanılmıştır. Aynı zamanda bu metodun Tekil Değer Ayrışımı (SVD) metoduna göre avantajarı ele alınmıştır. TSVD spektrumundaki "dirsek noktası" incelenerek, iletken olmayan (kayıpsız) beyin modelleri için $k_\alpha = 52$, gerçekçi iletkenlik altında ise $k_\alpha = 33$ modun korunmasına karar verilmiştir. Ek olarak bu değerlerin belirlenmesinde interaktif bir şekilde kullanıcının kesim noktasının görüntüleme sonuçlarına etkisini gözlemleyebileceği bir arayüz de kullanılmıştır. Yüksek mertebedeki gürültü bileşenleri elenmiş, bilgi içeriği maksimumda tutulmuştur. Ayrıca, dört aşamalı bir gürültü filtre zinciriyle (kafatası maskesi, Gauss yumuşatma, adaptif eşikleme ve morfolojik temizlik) elde edilen haritalardaki gürültüler azaltılmıştır. Böylece kullanıcıların daha net bir şekilde lezyon noktalarını gözlemleyebilmesi amaçlanmıştır.

Sonuçlar, beyin dokusunun gerçekçi iletkenlik değerine ($\sigma = 0{,}9\,\mathrm{S/m}$) sahip olduğu durumda mikrodalga sinyalinin dokuda %99'dan fazla sönümlendiğini ve alıcı antenlere yalnızca gönderilen gücün çok küçük bir kısmının ulaşabildiğini göstermiştir. Bu koşullarda, TSVD algoritması ile elde edilen görüntülerde yoğun gürültü hakim olmuş, lezyonların kontrastı önemli ölçüde azalmıştır. Buna karşın, iletkenliğin sıfırlandığı (kayıpsız) simülasyonlarda hem enerji transferi tam sağlanmış hem de kanama konturlarının ve odaklarının açıkça seçilebildiği net haritalar elde edilmiştir. Özellikle küçük ya da derin lezyonların gerçekçi iletkenlikte güvenilir biçimde tespit edilememesi, yöntemin klinik uygulanabilirliği açısından önemli bir sınırlama olarak kaydedilmiştir.

Dört farklı durumdan elde edilen beş farklı klinik senaryo üzerinde yapılan testlerde, kayıpsız modellerde tüm kanama odakları başarıyla lokalize edilebilmiş; en küçük lezyon dahi TSVD ile tespit edilmiştir. Lezyon çapı arttıkça, TSVD yoğunluğunun da alan içinde yayıldığı ve bunun zamanla kanama progresyonunu takip etmek için nicel bir gösterge olabileceği görülmüştür. Öte yandan, gerçekçi iletkenlik koşulunda yalnızca yüzeye yakın ve büyük odaklar net biçimde görüntülenebilmiş; küçük ve derin kanamalar ise gürültü ile görüntülenebilmiştir.

Bu bulgular, sistemin tam anlamıyla klinik uygulamaya geçebilmesi için çeşitli geliştirmelere ihtiyaç olduğunu göstermektedir. Özellikle doku içi kayıpları telafi etmek amacıyla; anten sayısının artırılması, yatay ve dikey polarizyonların birlikte çalıştığı durumların eklenmesi ve anten tasarımının buna göre yapılması, farklı anten tiplerinin denenmesi, daha düşük çalışma frekanslarının kullanılması ve iteratif, doğrusal olmayan algoritmalar ya da derin öğrenme tabanlı gürültü azaltma yöntemlerinin entegre edilmesi gerekmektedir. Ayrıca, gerçek donanım testlerine geçildiğinde, çoklu portlu vektör ağ analizörü, otomatik anahtarlama matrisi ve dielektrik özellikleri ayarlanabilir bir miğfer gibi ilave ekipmanlara ve regülasyon uyumuna ihtiyaç duyulacaktır.

Sonuç olarak, çalışma yalnızca simülasyon ortamında gerçekleştirilmiş olmasına rağmen, optimize edilen anten dizisi, uygun eşleştirme ortamı ve TSVD tabanlı ters çözüm algoritması ile intrakraniyal kanamaların diferansiyel mikrodalga görüntüleme yöntemiyle tespitinin mümkün olduğunu göstermiştir. Bu yaklaşım, gelecek donanım

ve algoritmik iyileştirmelerle beraber, gerçek zamanlı ve yatak başı beyin kanaması izlemeye uygun, taşınabilir sistemlerin temelini oluşturmaktadır.

1. INTRODUCTION

1.1 Purpose of Project

This project intends to design a portable, non-invasive, and economic system using microwave imaging that will be used for continuous intracranial hemorrhage monitoring. This satisfies the urgent demand for bedside monitoring of brain damage resulting from traumatic events or strokes. Modern imaging methods such as CT and MRI are non-portable systems with rather high cost. These are limiting factors in their practicality for emergency and critical care. Emphasizing cost-effectiveness and portability, the project provides a solution that will greatly help to enable timely and accurate medical intervention [1].

Design and implementation of antennas that are appropriate for operation at 900 MHz is one of the main responsibilities of the project. These antennas should be created such that they interact effectively with the biological tissues while preserving great signal integrity. Furthermore, a matching medium will be developed to improve signal transmission and reception between the antenna and the human head. Integrated into the system, advanced imaging algorithms will help to interpret data acquired and enable real-time visualization of hemorrhagic changes. This work combines machine learning approaches to raise image diagnostic clarity and resolution. Combining several disciplines—including microwave engineering, antenna design, and machine learning—will help to overcome some of the main constraints of current brain imaging systems. A prototype system with real-time and accurate monitoring capability is what is anticipated. This has great potential to transform methods of intracranial monitoring and enhance outcomes for critically ill patients.

1.2 Work Plan

1.2.1 Initial work plan

The work plan contains some significant phases. First, antennas operating at 900 MHz are designed and optimized using HFSS. Then, dielectric matching medium is designed to maximize signal penetration with lowest possible artifacts. There are eight antennas initially arranged this way. Data interpretation calls for sophisticated imaging techniques. At last, neural networks are used to improve resolution and clarity. Performance validation under reasonable conditions will be done using extensive simulations.

1.2.2 Work plan updates

Initially, the system was supposed to run on 8 antennas. Later on, this setup was changed to include 16 antennas in order to improve image coverage and resolution. More antennas help to improve spatial resolution and produce better imaging results [2]. Radar methods were first taken under consideration for microwave imaging. We nevertheless chose to use the linear Truncated Single Value Decomposition (TSVD) technique. Under noisy environments, the TSVD approach offers better image reconstruction accuracy and more computational efficiency.

Vivaldi or patch antennas were first considered for signal transmission and reception. It shifted to dipole antennas. Targeting brain imaging, the dipole antennas have shown better performance in signal penetration, homogeneous radiation pattern, and more straightforward simulation. Earlier the project suggested using an inhomogeneous head phantom for testing and simulation. Later on, though, this was turned to a homogeneous head phantom inside the HFSS simulation environment. Homogeneous phantoms give more consistent baseline results for the validation of an algorithm and simplify the simulation process.

1.3 Literature Review

The literature in microwave imaging for brain monitoring has underlined a non-invasive, low-cost, portable approach of diagnosing and continuously monitoring intracranial conditions including hemorrhages and strokes. This review summarizes knowledge from many studies to show present developments and constraints related to the project.

The basis of microwave imaging is the contrast in electromagnetic characteristics between healthy and diseased brain tissues. It is demonstrated by using the contrast source inversion approaches how differential imaging techniques can be applied to track changes in hemorrhagic volumes over time [3]. Based on variations in electric field measurement in tracking volumetric evolutions, these methods have rather good accuracy even in noisy environments. Likewise, a linear microwave imaging system that generates non-anatomical maps of hemorrhagic areas has been proposed to efficiently localize the changes within affected area while yet maintaining computational efficiency [3].

Conversely, quantitative imaging techniques including DBIM have also experienced remarkable advancements. Mousavi and Majedi (2024), for example, improved DBIM's accuracy by means of first guesses based on structural similarity with MRI-based images. This helps to improve the quality of the rebuilt images, which are crucial in providing contrast between the hemorrhagic and ischemic strokes. Further research on robustness of differential imaging against inaccuracies due to patient specificity revealed that effective monitoring is achievable even with minimum dependence on personalized data [4].

Other works focus on Factorization Method and TSVD. TSVD is a quantitative method based on the Born approximation to linearize the problem for reconstruction of altered dielectric properties in brain tissues. This finds a suitable balance between computational complexity and accuracy by decomposing the scattering operator into singular values and subsequently selecting truncation for stabilization of the solution. This is a computationally effective method that is also frequently applied in bench-marking experimental studies.

There is close relationship between the Factorization Method (FM) and the Linear Sampling Method (LSM). FM offers one method of qualitative inverse scattering. FM reduces the need for noise-level estimates for regularization, which improves its practical uses in experimental environments. It offers a map of geometric features of scatterers by eigenvalue analysis of the scattering operator that is useful for enabling high-reliable localization of hemorrhagic areas.

Improving signal penetration and image resolution has been stressed as mostly dependent on the choice of matching media and optimal antenna configurations. Examining the effects of dielectric properties on transmission and resolution, in [4], Scapaticci et al. (2014) found frequency ranges and medium properties that maximize imaging efficiency while still preserving patient safety.

In spite of these developments, problems including sensitivity to noise, resolution restrictions, and the need of validation in the real world still exist. Most algorithms that reflect the present state-of-the-art assume simplifications, which might not be valid in complex, homogeneous media such as the human brain. An active field of study is overcoming these obstacles by improved integration of machine learning with adaptive imaging methods.

All things considered, the literature examined supports the feasibility of microwave imaging in continuous brain monitoring, particularly in cases of bleeding. This project improves those very foundations by including neural networks with advanced imaging algorithms that improves diagnostic clarity and resolution.

2. METHODS AND RESOURCES

2.1 Methods Used in This Project

Three separate steps include microwave imaging of hemorrhagic strokes: antenna simulation, image reconstruction, and image optimization used by machine learning methods. Fundamentally, a microwave imaging system consists of a computing unit where the image is reconstructed from the measured data, a measurement subsystem in charge of doing microwave measurements, and antennas. The selected measuring configuration simply forms the whole design of the system. Within all these several, conventionally used configurations, where more fixed antennas are used [5], the multi-static measurement arrangement stands out regarding effectiveness and workability.

Then, using a system with sixteen antennas, HFSS simulations were carried out by varying a configuration and type of antenna operating at a given frequency from a literature review. Using Finite Element Method (FEM), which is quite successful in modeling intricate and heterogeneous geometries like the human brain, the simulations were carried out. Figure 2.1 shows the numerical techniques and their application domains [6]. Realistic imaging scenarios involve simulating wave interactions with multi-layered media, thus it is especially efficient. FEM is also a great tool for designing and evaluating brain imaging systems since it supports adaptive meshing, so optimizing computational resources while preserving accuracy. HFSS also provides a library of predefined models, including simplified human brain phantoms.This accelerates the design process and reduce the time needed to create feasible simulation environments. These parameters are exported as s16p files as the measured quantities needed for differential imaging are scattering parameters rather than electric fields. Differential Microwave imaging (DMI) techniques were applied in the imaging stage. In microwave brain imaging, DMI is a sophisticated method emphasizing on [5].

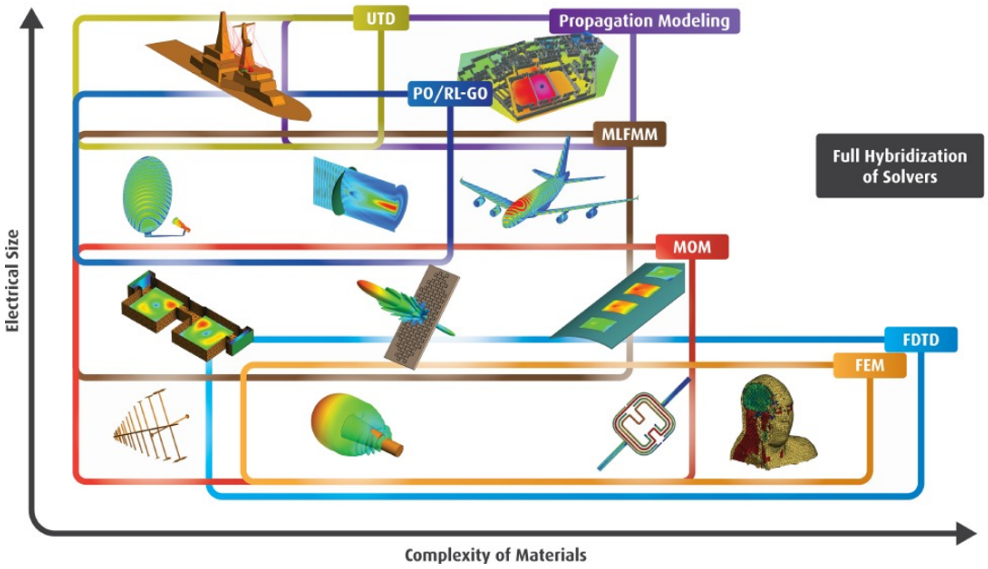

Figure 2.1 : Illustrations of numerical analysis techniques.

For the imaging step, Differential Microwave Imaging (DMI) methods were employed. DMI is an advanced technique used in microwave brain imaging that focuses on detecting and analyzing changes in the electromagnetic properties of brain tissues over time or between two states [5]. This makes it highly suitable for dynamic and real-time monitoring of brain conditions. The complex 3D vectorial problem is simplified into a 2D scalar problem to significantly reduce the computational complexity. Reconstruction methods in microwave imaging are broadly categorized into two types: quantitative methods and qualitative methods, which focus on retrieving the geometrical features of the target. One of the quantitative approaches used in this work is the Truncated Singular Value Decomposition inversion. Another approach applied in this work is the Factorization Method, which is a qualitative method. Both TSVD and FM methods will be applied using Python, which ensures a dual-method approach for the analysis, hence reliability in the imaging process. These methods will be explained later in this report.

Lastly, machine learning techniques after the initial results of imaging will provide the optimum resolution and reliability to the reconstructed images. Such approaches are fundamental when trying to balance resolution and reduce computational complexity in image reconstructions. Moreover, machine learning techniques can find more patterns and/or correlations than typical methods can identify in data. This helps identify hemorrhagic stroke detection and its characterization more accurately.

2.2 Analysis of the Resources for This Project

A microwave imaging system for the detection of hemorrhagic stroke relies on a few important resources in an appropriate manner. With great accuracy, a 16-port Vector Network Analyzer is used as the main measuring tool to calculate the S-parameters that will play a very basic role in analyzing the interaction of electromagnetic waves with the brain phantom and the hemorrhagic stroke model. Especially, employing S-parameters instead of electric field measurements is quite beneficial since VNAs are commercially available with high performance and growing dynamic range. Furthermore ensured by the VNA is that the measurement system's output power does not surpass 10 dBm (10 mW), much below the internationally agreed safety limits for mobile and wireless communication systems. For any practical use, this makes the system safe and realistic. By means of a coordinated multiport configuration of the VNA with the multi-static measurement arrangement, data is simultaneously obtained from the sixteen antennas. In image reconstruction, this offers far faster processing and much improved accuracy. From the lab, the anechoic chamber, shown in Figure 2.2, creates an environment without the interference of external electromagnetic fields, so making the measurements consistent.

Figure 2.2 : ITU Medical Device Research Development and Application Laboratory Equipments: Anechoic Chamber and VNA.

A small water-filled balloon modeling the existence of bleeding inside the brain will help to create the hemorrhagic stroke. To generate a reasonable test scenario, the brain phantom from our laboratory shown in Figure 2.3 mimics the dielectric permittivity and conductivity of actual brain tissues [5]. These instruments taken together offer the basic foundation for accurate data collecting and effective imaging in the project.

Figure 2.3 : Head phantom: front view and top view.

3. MONITORING OF BRAIN WITH MICROWAVE IMAGING

3.1 HFSS Simulations

Proposed setup is realized at ANSYS HFSS software [7]. The dipole antennas are designed to operate at a frequency of 900 MHz which is determined to be the optimal frequency for microwave brain stroke imaging [3, 5, 6]. After simulations, the designed dipole antenna has a total length of 15.6 cm, which closely aligns with theoretical calculations. Furthermore, the radius of the metal arms are determined as 0.3 mm and the feeding gap between metal arms are determined as 0.8mm. These parameters have negligible effect on the resonant frequency as opposed to the total length of the antenna. Return loss results of the single antenna shows that, designed antenna has a bandwidth of 66.4 MHz and operating frequency of 902 MHz as shown in Figure 3.1.

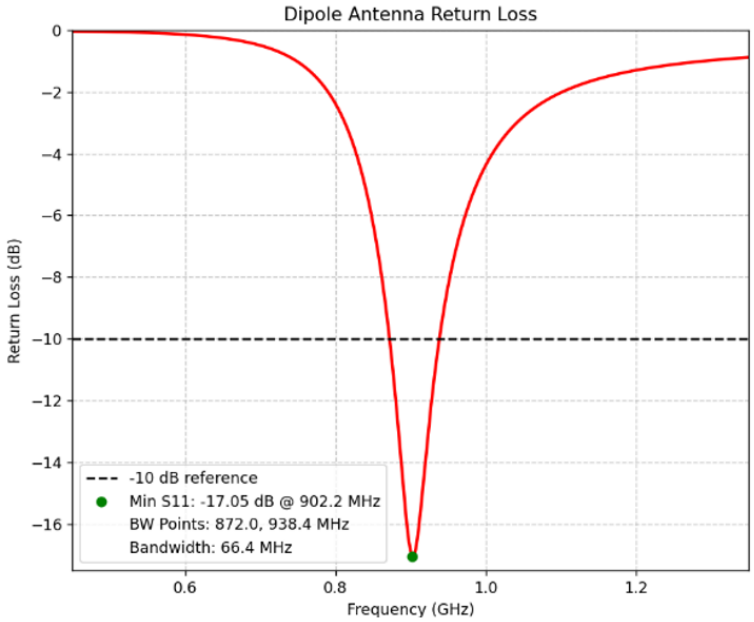

Figure 3.1 : Return loss results of the single dipole antenna.

In order to simulate brain stroke detection scenarios, male head model provided in the component libraries at HFSS is used. HFSS uses a homogeneous material inside of the head model for simplicity. Antennas are placed such that middle points of the dipole antennas align with the most upper side of the human head. Total of 16 dipole

antennas are used for improved resolution. In order to simulate stroke, a sphere with water filled inside is used since electrical properties of the water are quite similar with blood due to its plasma component that includes water about 92% in it [5, 8]. Blood can be detected through microwave imaging simply because dielectric properties of the brain tissues and blood are quite different.The blood has higher permittivity than the average permittivity of the brain [9].

Three cases are concerned in order to achieve differential microwave imaging. In the first case antennas are simulated with no brain stroke case. In the second case the brain stroke (water filled sphere) is placed inside of the human head with a radius of 1.5 cm. Since in differential microwave imaging one of the main aims is to get the information of whether stroke is growing or not, thus in the third case radius of the sphere is increased to 2 cm. Simulation setup of those three cases can be observed in the Figure 3.2. Also clear placement of the dipole antennas and brain stroke can be observed in the Figure 3.3. After simulation, scattering parameters of those three cases are extracted and saved for future use in the stage of data processing.

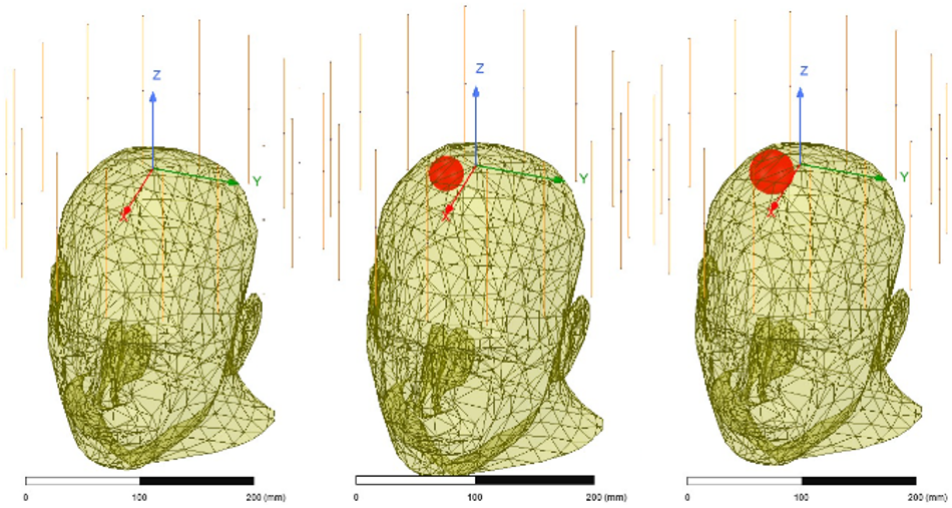

Figure 3.2 : Simulation setup: On the left healthy patient case, in the middle stroke with blood radius of 1.5 cm, on the right stroke with blood radius of 2 cm.

3.2 Differential Microwave Imaging

Microwave imaging is a technique that allows a non-invasive imaging approach for diagnostic applications, as opposed to other methods such as CT and MR. Explanation of how microwave imaging works can be found in Figure 3.4. Antennas placed around

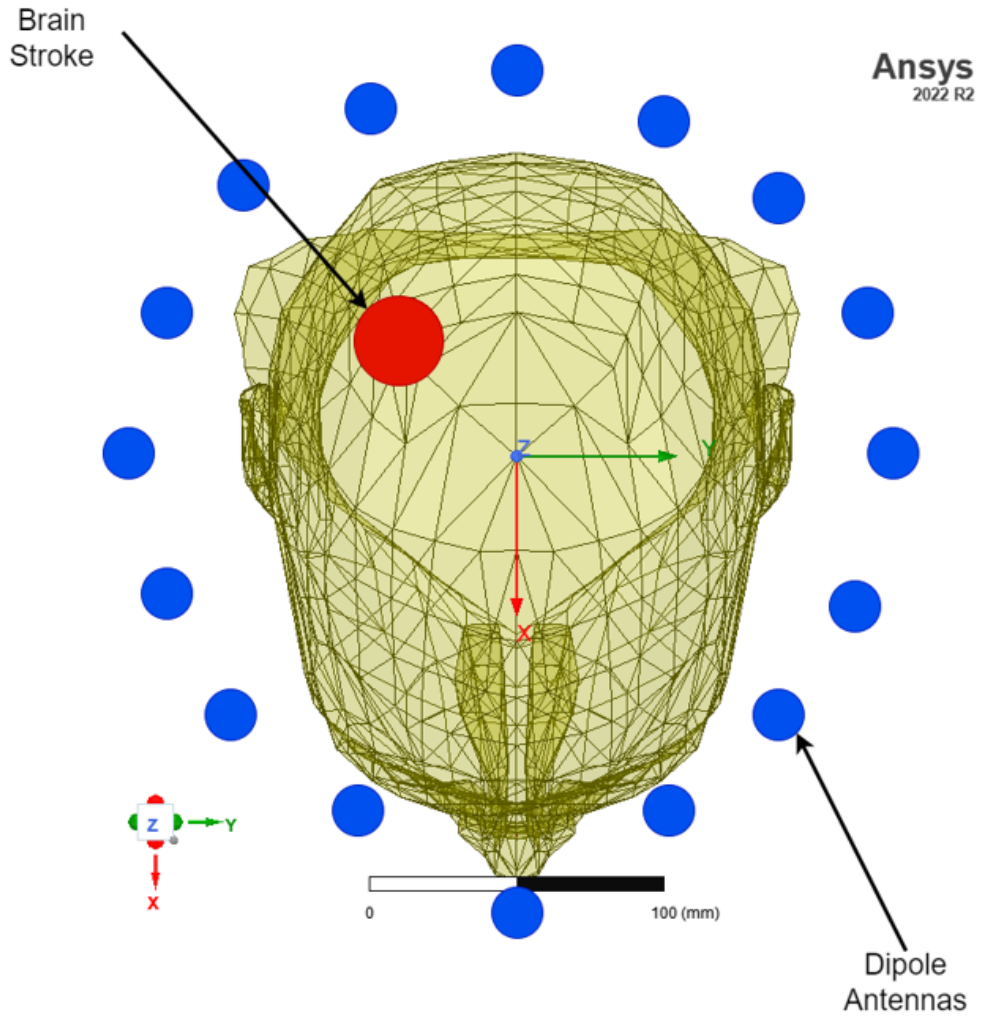

Figure 3.3 : Simulation setup: Antenna placement and brain stroke placement.

the target are processed by Vector Network Analyzer (VNA). VNA primarily measures scattering parameters in order to reveal tissue properties. Then, these parameters are processed using advanced algorithms to generate an image. This image can show abnormalities in the tissue concerned such as tumors and strokes. However, microwave imaging cannot be used for full body imaging, thus this method can be applicable for imaging of organs such as female breasts and human brain [10].

Microwave imaging algorithms can be divided into three categories named qualitative, quantitative deterministic reconstruction and hybrid methods. Qualitative methods cannot provide information about electromagnetic parameters such as dielectric permittivity and electric conductivity. However, qualitative methods provide information about the position and the shapes of the scatterers. This method can be utilized under certain approximations such as Born and Rytov type approximations.

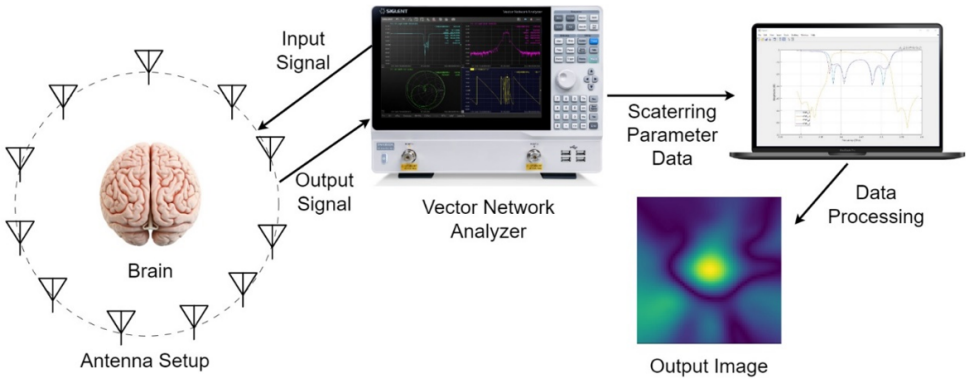

Figure 3.4 : The workflow of microwave imaging.

As an example, in order to apply Born approximation, the object should be known as a weak scatterer. The advantage of the qualitative methods is their computational efficiency, which enables fast reconstructions in limited time [10]. The linear sampling and the Born iterative methods can be given as examples of qualitative reconstruction methods [11].

Quantitative deterministic methods provide dielectric permittivity and electric conductivity information without the need of approximations. To utilize these parameters advanced deterministic algorithms are used. Consequently, even strong scatterers can be taken into account and these algorithms are valid for every scatterer, since quantitative methods originate from exact models. Thus it can be said that quantitative deterministic methods provide quite complete information about the scatterer; however, as a downside, this method is computationally expensive. Additionally, for convergence, starting guesses of the solution is needed [10]. The Distorted Born Iterative and Truncated Singular Value Decomposition methods can be given as examples of quantitative deterministic reconstruction methods [12].

Lastly, hybrid methods integrate various imaging techniques and algorithms to utilize the strength of each method. Generally, hybrid methods involve combining qualitative algorithms with quantitative methods to refine detailed distributions [13]. The Memetic Algorithm and Ant Colony Optimization can be given as examples of these hybrid microwave imaging techniques [14].

Differential microwave imaging, on the other hand, is useful to detect and image small scattering objects. Also, it is helpful to determine the changes in scattering properties

over time. Thus, in order to utilize differential microwave imaging, scattering properties of two different scenarios are needed [15].

3.3 Differential Microwave Imaging of Human Brain

Microwave imaging especially is applicable to the diseases concerning the human brain since the most popular methods such as MRI and CT are dangerous for continuous monitoring [16]. Microwave imaging holds immense potential for continuous monitoring of brain related diseases such as brain stroke, since there is electric contrast between stroke tissues and healthy brain tissues [17]. However, challenges such as solving the nonlinear inverse scattering problem must be addressed to increase the reliability and efficiency of this method [17]. A differential imaging approach in microwave imaging simplifies this problem. Thus, individuals can focus on variations in the stroke region over time which enables more efficient bedside stroke monitoring [4].

3.3.1 Mathematical framework for microwave imaging

The ideas of electromagnetic scattering form the basis of the mathematical framework for the differential microwave imaging to brain stroke monitoring application. Microwave imaging's main goal is temporal observation of stroke region changes by using scattered electromagnetic field measurements at multiple points. In this process, a single-frequency, multiview-multistatic measurement configuration is taken under consideration whereby each antenna alternates between transmitting signals and collecting them back to gather the scattered field data. The Lippmann-Schwinger equation characterizes the interaction of electromagnetic waves with brain tissue and provides the formula for the total electric field combining scattered and incident fields. The Eq. (3.1) [4] shows this connection.

$$E(r) = E_{\text{inc}}(r) + \int_V G(r,r')\,\chi(r')\,E(r')\,dr' \tag{3.1}$$

In Eq. (3.1), $\mathbf{E}(\mathbf{r})$ is the total electric field at a point. $\mathbf{E}_{\text{inc}}(\mathbf{r})$ is the incident electric field. $\mathbf{G}(\mathbf{r},\mathbf{r}')$ is the Green's function characterizing wave propagation. $\boldsymbol{\chi}(\mathbf{r}')$ is the electric contrast function. V is the volume of the scattering region.

This equation indicates variations in the electromagnetic characteristics of the brain tissue by indicating the connection of the scattered field and the contrast function. A fundamental parameter in microwave imaging, $\boldsymbol{\chi}(\mathbf{r})$ describes the variation in dielectric properties over the head. Mathematical expression of it is Eq. (3.2).

$$\chi(r) = k_0^2 [\varepsilon_r(r) - 1] - i\omega\mu_0\sigma(r) \tag{3.2}$$

In Eq. (3.2), k_0 is the free-space wavenumber, $\varepsilon_r(r)$ is the relative permittivity, $\sigma(r)$ is the conductivity, ω is the angular frequency, and μ_0 is the permeability of free space. This function provides a mathematical representation of the stroke-affected brain region by quantifying its electromagnetic properties, including permittivity and conductivity. In order to simplify the imaging process, the problem is linearized using the Distorted Born Approximation, which assumes that the changes in the contrast function over time are small. Under this approximation, the scattered field can be written as Eq. (3.3).

$$E_{\text{scat}}(r) = \int_V G(r, r') \Delta\chi(r') E_{\text{inc}}(r') dr' \tag{3.3}$$

$\Delta\chi(r')$ denotes the differential contrast function in Eq. (3.3). This corresponds with temporal variations in the stroke area. By means of this simplification in the equation, the nonlinear inverse scattering problem transforms into a linear one. This makes the problem computationally fair and suitable for real-time usages. Using linearized form, the inverse problem can be solved reconstructing the differential contrast function. That provides a spatial map demonstrating changes in the area affected by strokes over time.

Solving the imaging challenge has a strong basis provided by the mathematical formulation. These equations allow the electromagnetic variations between healthy and affected brain tissues to be used in identification of stroke areas. The ill-posed characteristics of the problem will challenge it going forward. Regularizing methods including Truncated Singular Value Decomposition (TSVD) will help to solve this difficulty. This regularity helps the solution to have a practical system for clinical application and stabilizes it.

Rebuilding the spatial map of the differential contrast, which shows changes in the stroke area over time, forms the imaging challenge. Assuming these are minor changes, the Distorted Born approximation helps to simplify the nonlinear to a linear inverse scattering problem [18]. This linearization simplifies computational needs and removes false solutions, so enabling real-time or quasi-real-time image reconstruction. Nevertheless, since the linear operator applied in this process is compact, the problem stays ill-posed and calls for regularizing techniques such Truncated Singular Value Decomposition (TSVD) to stabilize the solution [19].

Furthermore underlined in the section is the need of real-time monitoring for clinical use; hence, simplified, non-patient-specific reference models are advised to help to lower computational complexity. This method guarantees practical viability even in the presence of measurement errors by guaranteeing enough accuracy in identifying and tracking stroke development [4].

3.3.2 Inversion procedure

Differential microwave imaging for the reconstruction of stroke-related changes in brain tissues depends on the strong inversion process. An inverse problem with linear, ill-posed basis drives the imaging technique. The solution makes benefit of the TSVD scheme's regularization. This method approximates the differential contrast, so modeling stroke region changes. This is accomplished by modeling errors and noise stabilization of the reconstruction. Additionally, the TSVD truncation index strikes a compromise between spatial resolution and reconstruction stability. Using simplified, nonspecific reference models helps one take practical factors including the lack of exact patient-specific information into account. Although these models generate real-time images, the computational requirements are drastically lowered [4].

In Figure 3.5, flowchart of the microwave imaging procedure is explained. It shows how the linear operator is constructed, the use of non-specific head models, and the TSVD inversion. Notice that the whole procedure is designed to calculate all the most complex parts such as the building of the kernel and the computation of singular values; offline, reserving for real-time only the task of evaluating the differential contrast. This structured approach is aimed at ensuring practical and efficient clinical applications, with the possibility of monitoring stroke evolution in quasi-real time [4].

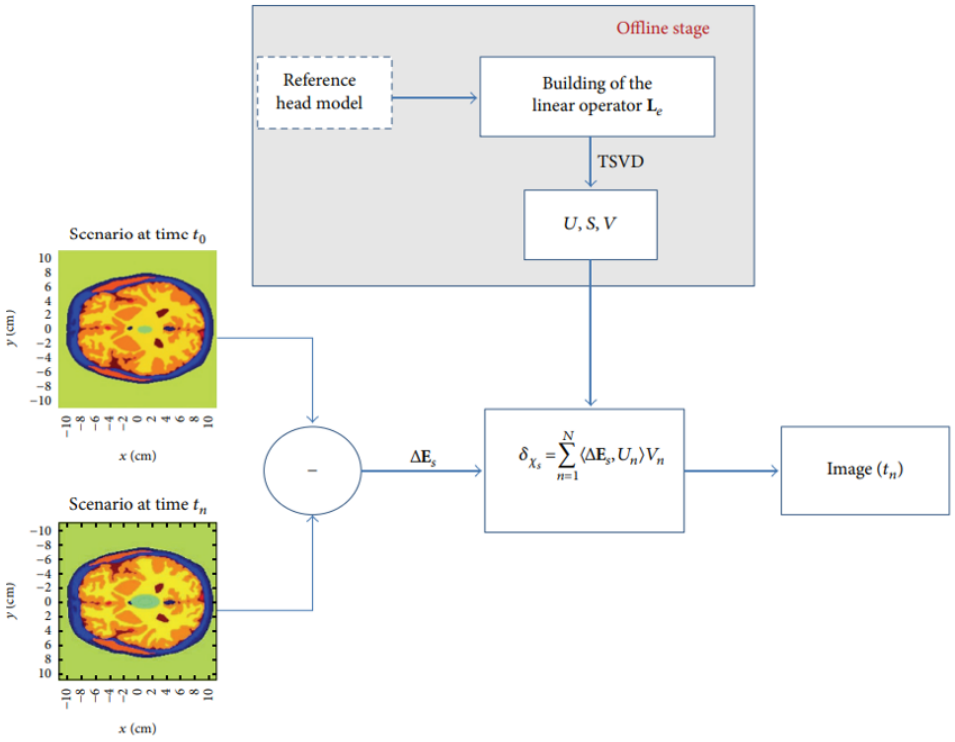

Figure 3.5 : Microwave imaging of human brain flowchart.

3.3.3 Truncated singular values decomposition (TSVD) method

Truncated SVD is a well-known regularization technique that has been widely applied in solving a variety of ill-posed inverse problems, including microwave imaging for medical diagnostics [20]. The direct inversion of the system matrix often amplifies the noise and yields unstable and inaccurate solutions. TSVD performs this by decomposing the system matrix into singular values and vectors, and truncating the smaller singular values. In such a way, the inversion stabilizes and accuracy in image reconstruction improves [21]. The linear inverse problem is represented in Eq. (3.4).

$$Ax = b \tag{3.4}$$

In Eq. (3.4), A indicates the system matrix, x denotes the unknown image vector, and b defines the measured data vector. The Singular Value Decomposition (SVD) provides the factorization of matrix A. The relationship is given in Eq. (3.5).

$$A = U\Sigma V^H \tag{3.5}$$

In Eq. (3.5), U and V represent the orthogonal matrices that contain the left and right singular vectors, respectively. Their orthogonality is expressed in Eq. (3.6).

$$U^*U = I, \quad V^*V = I \tag{3.6}$$

Σ is the diagonal matrix of singular values arranged in descending order, as shown in Eqs. (3.7) and (3.8).

$$\Sigma = \begin{bmatrix} \sigma_1 & 0 & \cdots & 0 \\ 0 & \sigma_2 & \cdots & 0 \\ \vdots & \vdots & \ddots & \vdots \\ 0 & 0 & \cdots & \sigma_p \end{bmatrix} \tag{3.7}$$

$$\sigma_1 \geq \sigma_2 \geq \cdots \geq \sigma_p \tag{3.8}$$

In TSVD, only the largest k singular values are retained to form the truncated diagonal matrix Σ_k. The approximate solution is computed in Eq. (3.9).

$$x_{\text{TSVD}} = V_k \Sigma_k^{-1} U_k^H b \tag{3.9}$$

This truncation will reduce the contribution of the noise and grant a more stable and precise reconstruction [21]. According to this perspective, TSVD has shown considerable promise toward enhancing both the quality and computational efficiency in image reconstruction concerning microwave imaging in the case of the detection of brain hemorrhages. For example, it was used for through-the-wall microwave imaging (TWI) applications and enhanced quality with respect to stability for images obtained [21].

TSVD is very sensitive; its effectiveness highly relies on the choice of an appropriate truncation threshold since it dictates the number of singular values to be retained for reconstruction. In choosing the optimal truncation threshold, there is always a trade-off between noise suppression and retention of critical features in the image [21]. Balancing truncation thresholds is very important in enhancing image clarity and resolution in medical imaging applications. By implementing the TSVD in image

reconstruction, the system gains the ability to present more realistic and stable outputs, which is necessary for diagnosis and monitoring of brain hemorrhage [21].

3.3.4 Advantages of TSVD over SVD

In many linear imaging problems, including those encountered in microwave brain imaging under the Born approximation, the system matrix $A \in \mathbb{R}^{m\times n}$ is ill-conditioned or nearly rank-deficient. A common representation of the inverse problem is given in Eq. (3.4), where A is the forward model, x is the unknown contrast distribution (e.g., permittivity changes in brain tissue), and b is the measured data. When this system is solved via Singular Value Decomposition (SVD), we can write it as shown in Eq. (3.5). The least-squares solution can be obtained as in Eq. (3.10).

$$x_{\mathrm{LS}} = A^{+}b = \sum_{i=1}^{r} \frac{\langle u_i, b\rangle}{\sigma_i} v_i \tag{3.10}$$

Here, $\{\sigma_i\}$ are the singular values, and $r = \mathrm{rank}(A)$. The vectors $\{u_i\}$ and $\{v_i\}$ form orthonormal bases for the column and row spaces of A, respectively. The problem arises when some σ_i are very small. In such cases, the corresponding terms in the solution behave as in Eq. (3.11).

$$\frac{\langle u_i, b\rangle}{\sigma_i} \to \infty \quad \text{as} \quad \sigma_i \to 0 \tag{3.11}$$

This suggests that division by small σ_i may cause random components in the projection $\langle u_i, b\rangle$ to be significantly amplified even if the data vector b is just a little contaminated with noise. These unstable modes thus take front stage in the rebuilt image x_{LS}, producing artifacts or unrealistic reconstructions. Commonly encountered in practical situations, especially when reconstructing high-spatial-frequency components, this condition stands out of ill-posed problems.

Truncated Singular Value Decomposition (TSVD) solves this by entirely ignoring the contributions of small singular values, so transforming the solution. As shown in Eq. (3.12) only the first k_α terms that which correspond to the highest singular values are retained rather than summing over all r components.

$$x_{\text{TSVD}} = \sum_{i=1}^{k_\alpha} \frac{\langle u_i, b \rangle}{\sigma_i} v_i \tag{3.12}$$

This results in a regularized solution that is more stable and less sensitive to noise. The corresponding rank-k_α approximation of the system matrix is provided in Eq. (3.13).

$$A_{k_\alpha} = \sum_{i=1}^{k_\alpha} \sigma_i u_i v_i^T \tag{3.13}$$

This approximation removes out directions in which the data is unreliable or uninformative while yet preserving the main behavior of the system. This can be selected according to application-specific constraints or spectral analysis techniques such the L-curve or cumulative energy ratio, the truncation threshold k_α serves as a regularizing factor.

TSVD also has another main benefit in not requiring continuous regularization parameter tuning (as in Tikhonov regularization). Rather, it uses a strong cut in the singular value spectrum to simplify interpretation and analysis. Within the limited subspace spanned by the first k_α singular vectors, TSVD also produces a minimal-norm solution, so naturally urging smoothness and suppressing unstable high-frequency components.

To illustrate these properties in a controlled and intuitive setting, we implemented a simplified experiment using image compression. In this demonstration, a grayscale image matrix was decomposed via SVD, and then reconstructed using varying numbers of retained singular values. This example does not involve noise or measurement data; rather, it serves to visually and numerically demonstrate the importance of singular value magnitudes in representing meaningful content.

The results show that the first 20–40 singular values carry the vast majority of the image's structure, while the remaining components contribute diminishingly small refinements. Reconstructions with fewer than 10 singular values retain only rough outlines, while those with 30–40 achieve nearly lossless visual fidelity. This provides direct insight into the information density of singular modes and supports the practical use of TSVD for reducing dimensionality, improving computational efficiency, and eliminating unnecessary components.

This analogy extends naturally to microwave brain imaging: just as high-order singular values in an image contribute little to overall structure, fine-scale contrast features in electromagnetic imaging may also lie below the noise floor or resolution limit of the system. TSVD enables reconstructions that focus on the dominant, reliably detectable features — such as the presence and approximate location of hemorrhagic tissue — while suppressing unstable, high-frequency artifacts that would otherwise be introduced by attempting to recover contrast modes associated with negligible singular values.

In our system, where the main clinical goal is to identify and track gross changes in intracranial dielectric properties, this emphasis on dominant features is not only sufficient but also beneficial. By means of constraints on antenna geometry, signal penetration, and measurement resolution, TSVD naturally promotes stability and interpretability, so avoiding overfitting to data components with perhaps limited physical significance.

Therefore, TSVD does not merely serve as a numerical trick to handle instability, but becomes a core part of the imaging philosophy itself: to extract only those features which the system is capable of measuring and resolving meaningfully. This is particularly relevant in differential imaging scenarios, where relative changes over time (such as stroke growth or remission) are of higher diagnostic value than exact absolute permittivity reconstructions. In such applications, it is often more important to ensure consistency and robustness in the imaging pipeline than to attempt recovery of fine details that lie outside the system's sensitivity bandwidth.

In the following appendix, we present a practical illustration of these ideas through a controlled TSVD-based image compression experiment. Although it does not involve clinical data or electromagnetic simulation, it provides a valuable visual and quantitative demonstration of how singular values govern reconstruction quality, and how truncation serves to balance fidelity and interpretability.

3.3.5 TSVD example application

To demonstrate how TSVD operates for image compression, that is, to examine the impact of retaining different numbers of singular values, a python program is used. The operation begins with the importing of an image and conversion to grayscale

format to simplify analysis. Then the image matrix is normalized and reshaped in 2D format, suitable for matrix operation. The initial step in the process is to conduct a complete Singular Value Decomposition (SVD), with the highest number of permitted components, and the singular values are then extracted and plotted graphically to ascertain their distribution. Compression analysis is then carried out in the subsequent step by specifying a series of component thresholds (e.g., [5, 10, 20, 30, 40]). For each threshold value, TSVD is repeated but with fewer components. The image is reconstructed using only the selected components, and the reconstructed image is displayed to verify the impact of compression at every level of threshold. This is carried out to examine how the number of components affects the quality and compression ratio of the image.

Figure 3.6 shows the graph of singular values obtained by the TSVD. The sharp drop after the first few singular values indicates that the larger portion of the information in the image is contained in the first few components, and the remaining components contribute less. The first singular value is far bigger than the others. After significant drop, the singular values are very small, indicating diminishing returns on keeping more components.

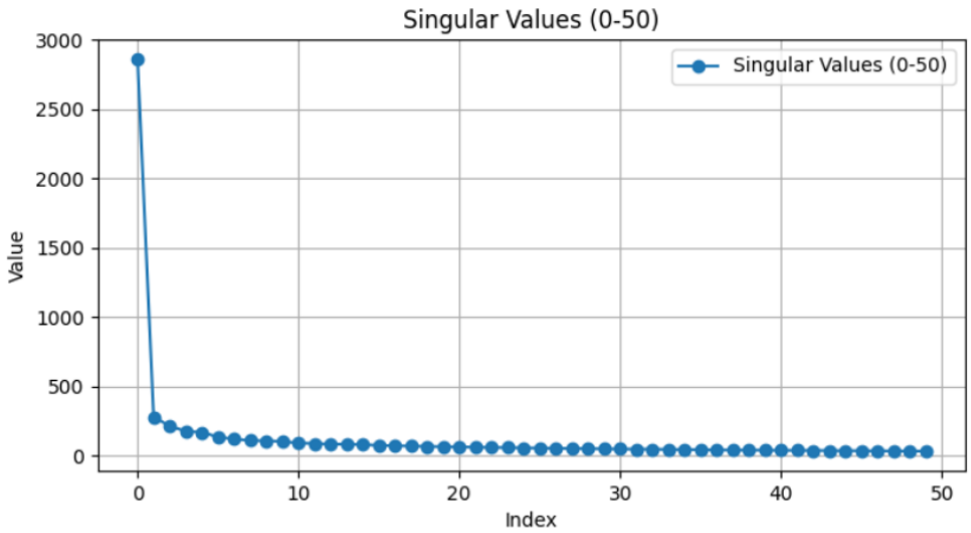

Figure 3.6 : Singular value distribution obtained from the TSVD.

Figure 3.7 is a comparison between the original image and reconstructed images with different numbers of singular values. With 5 singular values, the image is very blurred and only general structural outlines can be seen. With 10 singular values, structure is more apparent, but fine detail is absent. When 20 singular values are used, the

image quality is significantly improved and major features can be recognized. When 30 singular values are used, the image is quite close to the original with medium detail preservation. Finally, when 40 singular values are used, near-original quality is achieved and adequate information is preserved.

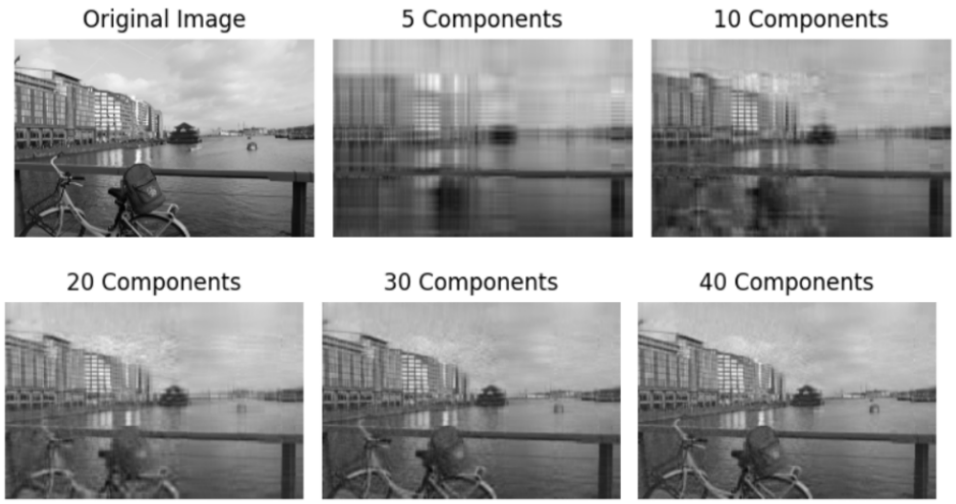

Figure 3.7 : Original image and its reconstructions with varying numbers of singular values.

This method can substantially reduce data storage and transmission requirements while maintaining visual quality. The singular value spectrum helps to decide on the optimal number of components to retain, compromising between compression efficiency and image quality.

Determining an appropriate threshold for singular values. Choosing the appropriate cutoff for singular values in applying TSVD is crucial in image compression and dimensionality reduction. The most significant decision is the number of singular values to retain in order to have an accurate reconstruction of the original data. Singular values represent the energy or variance each component contributes to the overall data.

Choosing the right number of components allows one to retain most of the energy of the image by reducing the components count. This guarantees good compression with very minimal evident loss of quality. There are present three main approaches of defining the singular value threshold. Usually in the range 90%-99%, the first is the cumulative energy threshold, which favors keeping the smallest number of components required to retain a proportion of the total energy.

This method uses the cumulative energy formula, in which the smallest number of components (k) is chosen such that the cumulative energy is more than the designated threshold, so preserving the most significant components.

The elbow method is the second method—a visual study of the singular value plot. In this case, the "elbow" or "knee" of the plot is an area of rapid slope change where the singular values until here have a greater contribution to the reconstruction while after this point they yield decreasing returns. Usually seen in retention of 30–40 components, the elbow is reminiscent of the next singular value plot.

The third method considers application-specific constraints including subjective visual quality criteria, real-time processing needs, and storage or transmission limits. Under bandwidth or computing restrictions, a smaller subset of components can be chosen to reduce the file size or speed processing even with the loss of image quality.

3.4 Inverse Scattering Theory

The term inverse scattering refers to the process of determining the internal structure or material properties of an object by observing how it scatters known electromagnetic waves. In the forward scattering problem, we assume we know the object's shape and properties, and we compute how waves will scatter from it. In contrast, the inverse scattering problem starts with the measured scattered waves, and aims to reconstruct the unknown object that caused them. It's called "inverse" because it reverses the usual direction of analysis—from observed effects (scattered fields) back to hidden causes (object properties).

Inverse scattering theory serves to determine the inner properties of an unknown object—most typically its permittivity ε_r and conductivity σ based on the measurement of scattered electromagnetic waves. When an incident electromagnetic field illuminates a dielectric or conductive object, it generates a scattered field, and from the examination of the scattered field, conclusions can be drawn regarding the object that caused it.

The entire area $u_t(z)$ fulfills the Helmholtz equation in a specified region Ω where the wave number $k(z)$ is spatially changing as shown in Eq. (3.14).

$$\left(\nabla^2 + k^2(z)\right) u_t(z) = 0 \quad \text{for} \quad z \in \mathbb{R}^2 \tag{3.14}$$

In the free region (outside Ω), the incident field $u_i(z)$ satisfies the Helmholtz equation as shown in Eq. (3.15).

$$\left(\nabla^2 + k_0^2\right) u_i(z) = 0 \quad \text{for} \quad z \in \mathbb{R}^2 \tag{3.15}$$

Here, $k(z)$ equivalent is shown in Eq. (3.16).

$$k(z) = \begin{cases} \omega^2 \varepsilon_z \mu - i\omega\sigma_z\mu, & z \in \Omega \\ k_0 = \dfrac{2\pi}{\lambda_0} = \omega\sqrt{\varepsilon_0\mu_0}, & z \notin \Omega \end{cases} \tag{3.16}$$

The scattered field $u_s(z)$ is defined as the difference between the total field and the incident field as shown in Eq. (3.17).

$$u_s(z) = u_t(z) - u_i(z) \tag{3.17}$$

The two Helmholtz equations are subtracted and rearranged to yield an inhomogeneous Helmholtz equation for the scattered field. This is shown in Eq. (3.18).

$$\nabla^2 u_s(z) + k_0^2 u_s(z) = -\left(k^2(z) - k_0^2\right) u_t(z) \tag{3.18}$$

This relation relates the measured scattered field $u_s(z)$ to the unknown object properties in Ω. The right-hand side, which is referred to as the contrast source, is the source of scattering and contains the internal object properties.

3.4.1 Implementation of Green function

To solve the inhomogeneous Helmholtz equation, we employ the Green's function method. The Green's function $g(z,z')$ satisfies the Eq. (3.19).

$$\nabla^2 g(z,z') + k_0^2 g(z,z') = -\delta(z - z') \tag{3.19}$$

For two-dimensional problems, the Green's function for free space is given as it is shown in the Eq. (3.20).

$$g\left(z,z'\right)=\frac{1}{4i}H_0^{(2)}\left(k_0\left|z-z'\right|\right) \tag{3.20}$$

Here, $H_0^{(2)}$ is the zero-order second-kind Hankel function. With this Green's function, the scattered field in a given point of observation p can be expressed as an integral over the object domain Ω as it is shown in the Eq. (3.21).

$$u_s\left(p\right)=\int_\Omega g\left(p,z\right)\left[k^2\left(z\right)-k_0^2\right]u_t\left(z\right)d\Omega\left(z\right) \tag{3.21}$$

Taking the object function to be $\chi\left(z\right)=\varepsilon_c\left(z\right)-1$, where $\varepsilon_c\left(z\right)$ is the complex permittivity, the integral equation is then becomes as shown in the Eq. (3.22) and Eq. (3.23).

$$u_s\left(p\right)=k_0^2\int_\Omega g\left(p,z\right)\left[\varepsilon_c\left(z\right)-1\right]u_t\left(z\right)d\Omega\left(z\right) \tag{3.22}$$

$$u_s\left(p\right)=k_0^2\int_\Omega g\left(p,z\right)\chi\left(z\right)u_t\left(z\right)d\Omega\left(z\right) \tag{3.23}$$

3.4.2 Born approximation

The nonlinearity introduced by the dependence of the object properties on $u_t\left(z\right)$ makes invert the inverse problem difficult directly. Assuming weak scattering, the Born approximation is a common linearization method based on which $u_s\approx 0$ inside the object. The incident field as shown in the Eq. (3.24) approximates the field inside Ω.

$$u_i\left(z\right)\approx u_t\left(z\right) \tag{3.24}$$

By substituting into the integral equation the Eq. (3.25) can be achieved.

$$u_s\left(p\right)\approx k_0^2\int_\Omega \chi\left(z\right)g\left(k_0\left|p-z\right|\right)u_i\left(z\right)d\Omega \tag{3.25}$$

When the incident field is produced by a line source at position q, it can also be written in terms of the Green's function as shown in the Eq. (3.26).

$$u_i\left(z\right)=g\left(k_0\left|z-q\right|\right)=\frac{1}{4i}H_0^{(2)}\left(k_0\left|z-q\right|\right) \tag{3.26}$$

Thus, the Born approximation simplifies the scattering equation to the Eq. (3.27).

$$u_s(p) \approx k_0^2 \int_\Omega \chi(z)\, g(k_0 |p-z|)\, g(k_0 |z-q|)\, d\Omega \tag{3.27}$$

This definition forms the foundation of numerous inversion techniques, in which the observed field $u_s(p)$ is employed to reconstruct the contrast function $\chi(z)$.

3.4.3 Python implementation of inverse scattering theory

The inverse scattering problem is discretized in order to be implemented numerically. The domain Ω is divided into M mesh elements, and the integral is a matrix-vector product as shown in the Eq. (3.28).

$$u_s = L\chi \tag{3.28}$$

Here $u_s \in \mathbb{C}^{N^2K\times 1}$ is the measured scattered fields for all N transmitters, N receivers, and K frequencies, $\chi \in \mathbb{C}^{M\times 1}$ is the discretized object contrast vector, and $L \in \mathbb{C}^{N^2K\times M}$ is the sensing matrix constructed from Green's functions. Each matrix element $L_{pq,m}$ can be equated as given in the Eq. (3.29).

$$L_{pq,m} = k_0^2 \int_\Omega g\big(k\,|p-z|\big)\, g\big(k\,|q-z|\big)\, \chi(z)\, \mathrm{d}\Omega(z) \tag{3.29}$$

To compute L in closed form, we first discretize the domain. We partition Ω into M circular cells $\{\Omega_m\}$ of radius a and area Δz, as given in Eq. (3.30) and Eq. (3.31).

$$\Delta z = \pi a^2, \tag{3.30}$$

$$\Omega = \bigcup_{m=1}^{M} \Omega_m, \qquad |\Omega_m| = \Delta z, \quad m = 1,\ldots,M. \tag{3.31}$$

Next, the volume integral in Eq. (3.29) is approximated by a Riemann sum sampled at the cell centers z_m, as shown in Eq. (3.32).

$$\int_\Omega g\big(k_0\,|p-z|\big)\, g\big(k_0\,|q-z|\big)\, \chi(z)\, \mathrm{d}\Omega(z) \;\approx\; \sum_{m=1}^{M} g\big(k_0\,|p-z_m|\big)\, g\big(k_0\,|q-z_m|\big)\, \chi(z_m)\, \Delta z. \tag{3.32}$$

Substituting the approximation (3.32) into Eq. (3.29) yields the discrete entry formula in Eq. (3.33).

$$L_{pq,m} \approx k_0^2\, g\big(k_0\,|p - z_m|\big)\, g\big(k_0\,|q - z_m|\big)\, \chi(z_m)\, \Delta z. \tag{3.33}$$

The Green's function $g(k_0 r)$ in Eq. (3.33) is defined by the zero-order Hankel function in Eq. (3.34).

$$g\big(k_0\, r\big) = \frac{1}{4j} H_0^{(2)}\big(k_0\, r\big). \tag{3.34}$$

For circular cells of radius a, the self- and mutual-cell integrals of $H_0^{(2)}$ admit the analytic form given in Eq. (3.35) [22].

$$\frac{jk_0^2}{4} \int_0^{2\pi} \int_0^{a} H_0^{(2)}\big(k_0\rho\big)\, \rho\, \mathrm{d}\rho\, \mathrm{d}\phi = \begin{cases} \dfrac{j}{2}\big[\pi k_0 a H_1^{(2)}(k_0 a) - 2j\big], & m = n, \\ \dfrac{j\pi k_0 a}{2} J_1(k_0 a)\, H_0^{(2)}\big(k_0 r_{mn}\big), & m \neq n, \end{cases} \tag{3.35}$$

Here, $r_{mn} = |z_m - z_n|$. In practice, the effective cell weight Δz in Eq. (3.33) incorporates the Bessel-term from Eq. (3.35), yielding the implementation coefficient in Eq. (3.36).

$$\Delta z = j\,\pi\, k_0\, a\, J_0\big(k_0 a\big). \tag{3.36}$$

Finally, absorbing $\chi(z_m)$ into each column of L gives the entry-wise approximation in Eq. (3.37).

$$L_{pq,m} \approx k_0^2\, g\big(k_0\,|z_m - p|\big)\, g\big(k_0\,|z_m - q|\big)\, \Delta z. \tag{3.37}$$

The object contrast reconstruction is performed by TSVD as shown in the Eq. (3.38).

$$\chi_R = \mathrm{TSVD}\,(L, u_s) \tag{3.38}$$

Python libraries used for implementation include NumPy for numerical computation and matrix operations, SciPy for linear algebra tasks such as Singular Value Decomposition (SVD) and Truncated Singular Value Decomposition (TSVD),

Matplotlib for visualization, particularly with tools like `pcolormesh`, and scikit-rf (`skrf`) for managing S-parameters, especially in `.sNp` file formats.

In future work, we will enhance our current TSVD-based reconstruction toolset to be more complete by having the complete Python pipeline to reconstruct the inverse scattering problem with simulated and experimental data. One goal is to have a modular, reproducible simulation environment where we can compare different forward models, levels of noise, and contrast distributions. This will include the computation of Green's function-based sensing matrices for various antenna geometries and frequencies, and simulation of known scattered field data from contrast functions. The TSVD reconstruction will be carried out with tunable truncation limits to explore stability and spatial resolution trade-offs at different physical conditions. Additionally, we will use advanced selection measures for the truncation parameter like automatic thresholding through cumulative energy and the L-curve method. The final code will enable visualization of contrast maps, singular value spectra, and residual errors to give comprehensive performance analysis. Python programming will be utilized to execute the entire matrix construction, TSVD solution, and result visualization using libraries such as NumPy, SciPy, and Matplotlib, focusing on clinical interpretability and algorithmic robustness in situations.

3.5 Matching Medium Design

3.5.1 Benefits of matching medium

Particularly at 900 MHz with dipole antenna arrays, in microwave biomedical imaging the use of a matching medium is crucial to solve the major impedance mismatch between air and biological tissues. Whereas biological tissues such skin and brain can have values exceeding 40, leading to strong reflections and poor signal penetration without appropriate coupling [23], air has a dielectric constant near 1. Significantly for reaching deep anatomical targets such as hemorrhagic areas within the brain, introducing a coupling medium with intermediate permittivity greatly reduces these reflections and improves the transmission of microwave energy into the body.

Furthermore greatly increases the coupling efficiency between the imaging domain and the antenna elements a matching media provides. This improved coupling reduces

energy losses at the interface, so increasing the amount of microwave energy entering the tissue and so improving the signal-to—-noise ratio of the measurements [23]. In practical systems, such the 16-element 3D microwave imaging prototype evaluated by Rodriguez-Duarte et al., each antenna is enclosed in a dielectric housing—serving as a local matching structure—to maximize energy distribution into the brain phantom [24].

Using a matching media also has a major benefit in terms of reducing of false interface reflections. If not under control, these reflections overwhelm the received signals and mask internal anomaly-generated smaller backscattered waves. Lui and Fhager underlined that the careful choice of matching medium can reduce this effect, so allowing better clarity in scattering parameter measurements and hence improving the quality of reconstructed images [25].

Apart from controlling interface noise, matching media help homogenize the near-field region surrounding the imaging target. More predictable wave propagation, less measurement variability, and simpler electromagnetic modeling needed for image reconstruction follow from this [25]. Moreover, since wave speed decreases in higher-permittivity media, the effective electrical size of the antenna array rises [23], so enhancing spatial resolution and detection sensitivity for small inclusions.

Overall, the advantages of using a matching medium in microwave brain imaging are lower impedance mismatch, better antenna coupling, suppressed reflections, more stable measurement environments, and better resolution and each of which is essential for the accurate detection of stroke-induced hemorrhagic lesions.

3.5.2 Updates in HFSS simulation

After the baseline free-space studies were finished, the computational model was completely rebuilt in HFSS with a dielectric matching layer around the antenna array and head phantom. Realizing the matching layer as a right circular cylinder whose solid volume is Boolean-subtracted by the head, one can say that the head sits inside a cavity carved out of a larger dielectric block. Selecting a cylinder is trivial to match the antenna ring, reduces error at the air interface, and enables rotationally symmetric adaptive meshing. Measuring from the anatomical center of the phantom, the cylinder's radius is fixed at 14.5 cm; each dipole is centered 12.5 cm from that

same origin, leaving a 2 cm gap filled totally by the homogeneous matching medium. Physical properties of the matching medium is provided in the Figure 3.8.

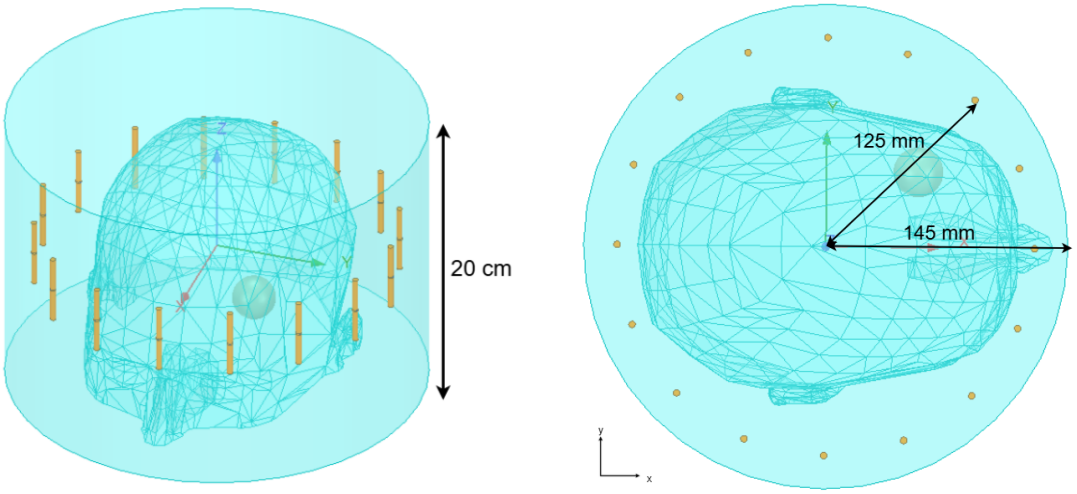

((a)) 3D view ((b)) Top view

Figure 3.8 : Geometric dimensions of the dielectric matching medium.

To ensure the dielectric material entirely envelops the area of diagnostic interest without generating an excessively tall domain, a further 2 cm vertical clearance is maintained above the skull vertex and below the chin plane. All matching medium properties are provided in Table 3.1 and other media properties are provided in Table 3.2.

Relative Permittivity	Bulk Conductivity	Radius	Radial Clearance
41	0.005 S/m	14.5 cm	2 cm
20	0.005 S/m	14.5 cm	2 cm

Table 3.1 : Matching-medium properties for $\varepsilon_r = 41$ and $\varepsilon_r = 20$.

Quantity	Air	Matching Medium		Brain	Water (stroke)
Relative Permittivity (ε_r)	1	20	41	41.5	80
Conductivity (σ) [S/m]	0	0.005	0.005	0.9	1.5
Free-space Wavelength (λ_0) [mm]	333	–	–	–	–
Wavelength in Medium (λ) [mm]	–	74.5	52.0	51.7	37.3
Wave Impedance (Z) [Ω]	377	84	59	58	42.1

Table 3.2 : Electromagnetic properties at 900 MHz for different media.

Because the additional dielectric more than doubles the electrical size of the domain, an immediate penalty is paid in solve time. The initial single-frequency run that had required roughly half an hour expanded to well over ninety minutes once the

$\varepsilon_r = 41$ matching layer was activated, owing to a three-fold increase in tetrahedral count. To compensate, the phantom geometry was truncated: all tissue lying below the nose was removed. Hemorrhagic strokes are confined to cranial contents, and the subtracted neck region does not influence microwave propagation paths that remain predominantly radial within the upper skull. Eliminating that sub-volume removes low-curvature features that otherwise force the adaptive mesher to maintain fine element sizes deep inside the model, thereby restoring manageable run times without sacrificing anatomical fidelity where it matters.

Immersion of the antennas in a high-permittivity bath reduces the effective wavelength; thus, the conducting elements themselves had to be miniaturized to maintain the resonant near to the target frequency ($\approx$ 900 MHz). Each dipole spans 3.3 cm with the arm radius of 1 mm to retain mechanical rigidity. The feed gap is widened symmetrically to 1 mm to simplify modeling of the coaxial excitation port. Once the compressed wavelength in $\varepsilon_r = 41$ is taken into account, an optimetrics sweep is performed for dipole lengths between 3 cm and 4 cm in 0.3 cm steps; the deepest S_{11} null occurred exactly at 3.3 cm, so confirming the analytical half-wavelength prediction. S-parameter values for different dipole lengths can be observed in Figure 3.9.

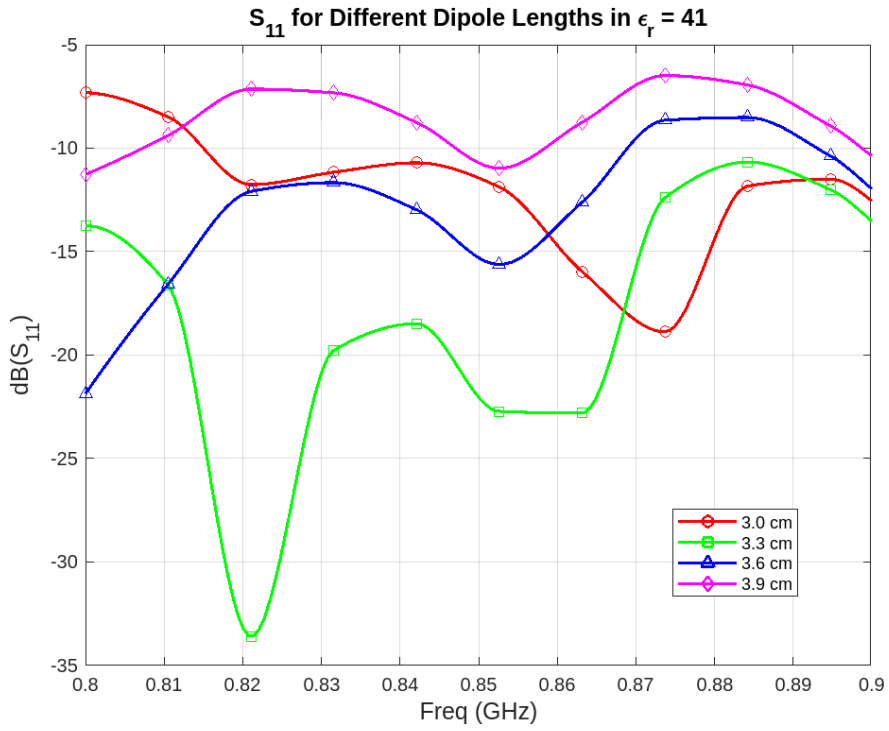

Figure 3.9 : S_{11} versus frequency for different dipole lengths ($\varepsilon_r = 41$).

Between consecutive passes, HFSS tracks the biggest change in the S-matrix (max $|\Delta S|$). After the standard six passes, the high-ε_r bath ($\varepsilon_r = 41$) would not fall below our 0.02 target, hence the solver would be pushed to keep constantly improving the mesh and significantly extending its completion time. The simulation ended much faster when we repeated the run using an identical model but reduced the matching-layer permittivity to $\varepsilon_r = 20$. Max $|\Delta S|$ moved under 0.02 within the same six passes. We kept $\varepsilon_r = 20$ for the following investigations since the lower-ε_r medium satisfies the convergence criterion while saving computation time.

We next decreased the matching-layer permittivity to 20, maintaining every clearance and global dimension the same. The dipole was retuned by stretching its length to 4.8 cm, as it was determined with parametric sweep shown in the Figure 3.10, and at the same time thickening each arm from 1 mm to 2 mm for a cleaner mechanical model; the 1 mm feed gap stayed unaltered. The rest of the geometry stayed as originally set; these little adjustments were all it took to restore the antenna to its half-wave resonance.

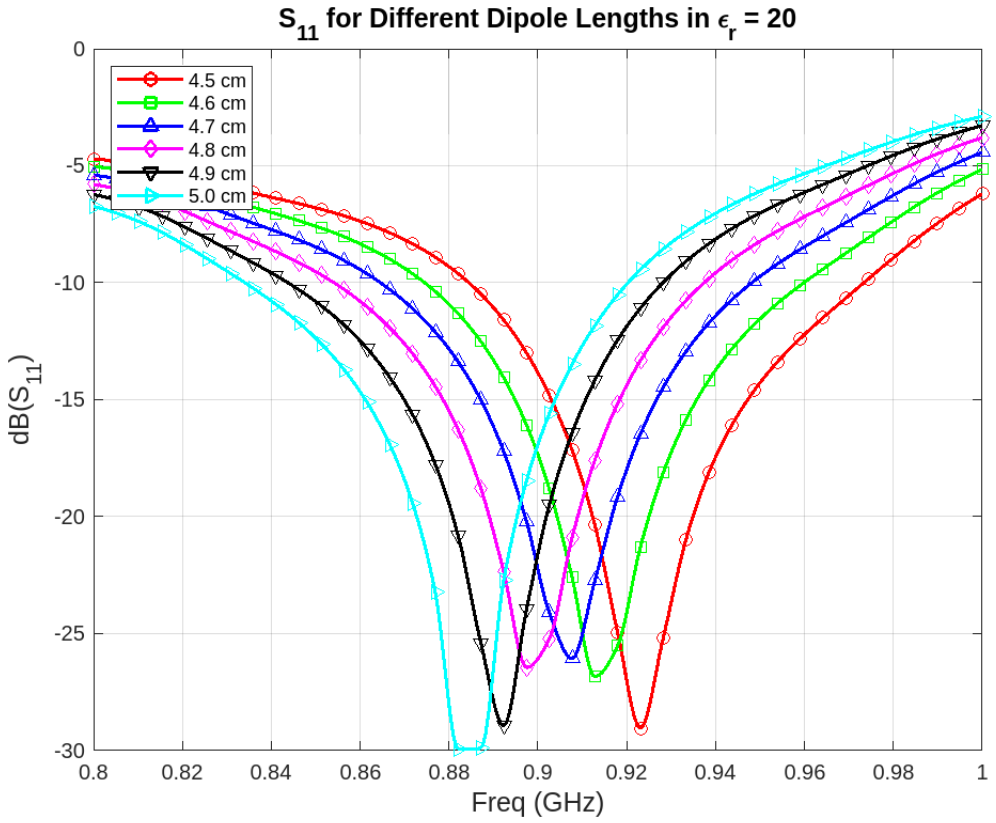

Figure 3.10 : S_{11} versus frequency for different dipole lengths ($\varepsilon_r = 20$).

Embedding a spherical inclusion of distilled water, diameter 3 cm (radius 1.5 cm), whose dielectric spectrum ($\varepsilon_r = 80$, $\sigma = 1.5$ S/m) simulates intracranial hemorrhage

at microwave frequencies results in stroke emulation. The sphere is placed on the right-bottom corner of the brain instead of at the geometric center. Assigning the average brain dielectric properties, provided in Table 3.3, the head volume that remains after truncation is assigned a realistic background for simulation.

	Relative Permittivity	Bulk Conductivity (S/m)
Head Phantom	41.5	0.9
Water (hemorrhage)	80	1.5
Matching Medium	20	0.005

Table 3.3 : Dielectric properties of head phantom, hemorrhage and matching medium after analysis.

The main numerical assumptions for the biological tissues as well as for the matching-medium scenarios are compiled below. All values line up with the operating band center. Corresponding antenna dimensions and parameters are provided in Table 3.4.

Antenna Property	Length
Dipole Length ($\varepsilon_r = 20$)	4.8 cm
Antenna Radius (head to antenna)	12.5 cm
Dipole Arm Radius	2 mm
Feed Gap Width	1 mm

Table 3.4 : Antenna dimensions and parameters in the final setup.

3.6 Python Implementation of TSVD

3.6.1 Structure of the code

The reconstruction pipeline is a direct numerical implementation of the forward model in Eq. (3.27), its singular value decomposition (SVD) in Eq. (3.37), and the truncated inverse of Eq. (3.27). At a high level, the script takes two measured S-parameter files (.s16p), builds the forward operator $\mathbf{L}$, applies a truncated-SVD (TSVD), and displays the resulting differential contrast $\delta\chi$. The pseudo-code below emphasises the logical flow.

Require: Two scattering matrices $\mathbf{S}_{\text{empty}}$ and $\mathbf{S}_{\text{bleed}}$; frequency index f_k; initial TSVD cut–off k_α

Ensure: 2-D image of the magnitude $|\delta\chi|$

1: **Load data:** extract the difference vector $\mathbf{u}_s \leftarrow \left[\mathbf{S}_{\text{bleed}}(f_k) - \mathbf{S}_{\text{empty}}(f_k)\right]_{\text{vec}}$

2: **Discretise domain:** generate an $N \times N$ square grid Ω and pre-compute pixel thickness Δz

3: **Build forward operator:** for every transmit–receive antenna pair evaluate the 2-D Green function $g(k_0 r)$ and assemble $\mathbf{L}$ according to Eq. (3.27)

4: **Factorise:** compute SVD $\mathbf{L} = \mathbf{U}\boldsymbol{\Sigma}\mathbf{V}^{\mathrm{H}}$ once per frequency

5: **Invert with TSVD:** retain the k_α largest singular values and compute $\delta\chi \leftarrow \mathbf{V}\boldsymbol{\Sigma}_{k_\alpha}^{-1}\mathbf{U}^{\mathrm{H}}\mathbf{u}_s$ (Eq. (3.12))

6: **Display:** reshape $\delta\chi$ onto the grid, plot $|\delta\chi|$

Steps 1–2 map measurement data onto the computational domain. Step 3 converts the continuous integral equation into the matrix form of Eq. (3.37). Steps 4–5 solve the ill-posed inverse problem by discarding the smallest singular values, mitigating noise amplification predicted by Eq. (3.12). Step 6 provides an interactive visual check so that the operator can tune k_α until the image stabilises. Flowchart of the code is provided in the Figure 3.11.

One of the important parameters in the algorithm is mesh resolution. Mesh resolution should be selected in a way that, imaging should be observed clearly and run-time should be efficient. The square imaging window has a physical side length $L = 0.20$ m, matching the head phantom used. At the centre frequency $f_0 = 900$ MHz the free-space wavelength is $\lambda_0 = c/f_0 \approx 0.33$ m. To avoid spatial aliasing, the Nyquist sampling criterion requires

$$\Delta x \;\le\; \frac{\lambda_0}{2} \;=\; \frac{c}{2f_0} \;\approx\; 0.165\ \text{m}, \tag{3.39}$$

where Δx is the pixel pitch. For a uniform grid of $n_{\text{grid}} \times n_{\text{grid}}$ pixels the pitch is

$$\Delta x \;=\; \frac{L}{n_{\text{grid}}}. \tag{3.40}$$

Setting $n_{\text{grid}} = 128$ gives $\Delta x \approx 1.6$ mm $\ll \lambda_0/2$, oversampling the field by more than two orders of magnitude. Further refinement therefore brings little benefit, while the computational cost of the SVD in Eq. (3.37) rises steeply.

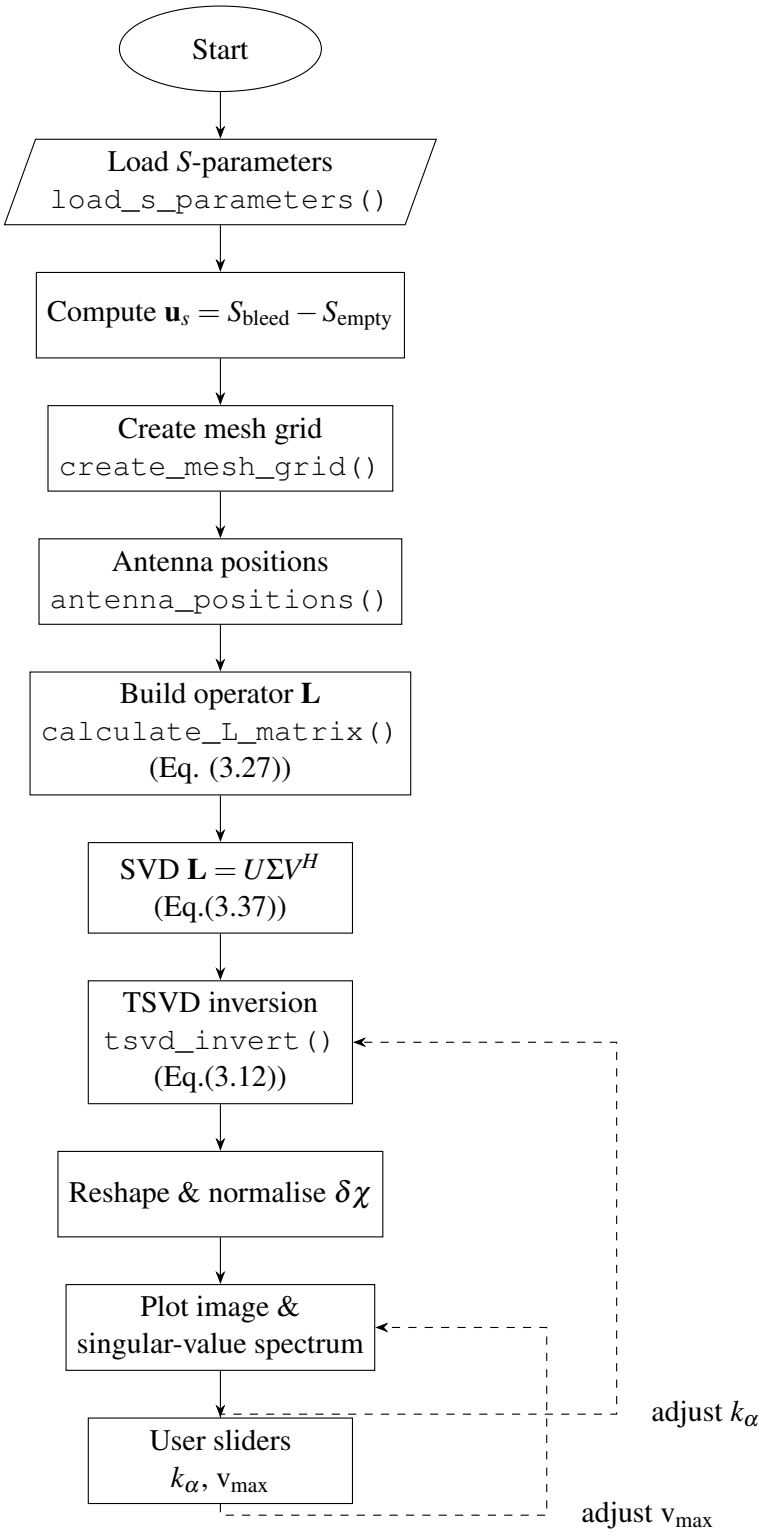

Figure 3.11 : Execution flow of the TSVD reconstruction pipeline implemented in the project.

$$T_{\text{SVD}} \sim \mathcal{O}\big(N_{\text{pix}}^3\big) = \mathcal{O}\big(n_{\text{grid}}^6\big), \tag{3.41}$$

so doubling the linear grid size from 128 to 256 would increase run-time by a factor $2^6 = 64$. Conversely, reducing the grid saves time but eventually degrades image quality as shown in Fig. 3.12. Finer meshes reveal smooth, continuous structures at the cost of higher SVD run-time (Eq. 3.41), whereas coarse meshes obscure detail and introduce block artefacts. The 128×128 mesh thus strikes a practical balance between spatial fidelity and execution time.

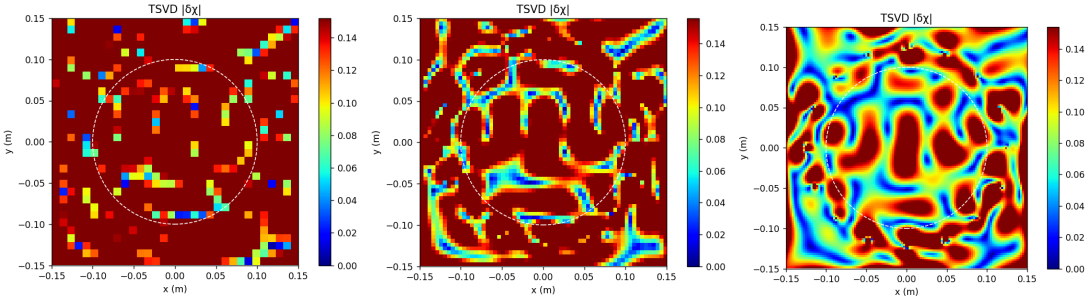

((a)) 32×32 pixels ($\Delta x \approx 6.3$ mm)

((b)) 64×64 pixels ($\Delta x \approx 3.1$ mm)

((c)) 128×128 pixels ($\Delta x \approx 1.6$ mm)

Figure 3.12 : Effect of mesh resolution on the TSVD magnitude map $|\delta\chi|$.

3.6.2 Cut-off selection

The choice of the TSVD cut-off index k_α is based on a combination of spectral, energetic, and qualitative criteria. First, the singular-value spectrum of the forward operator is computed and plotted on a linear scale, provided in the Figure 3.13.

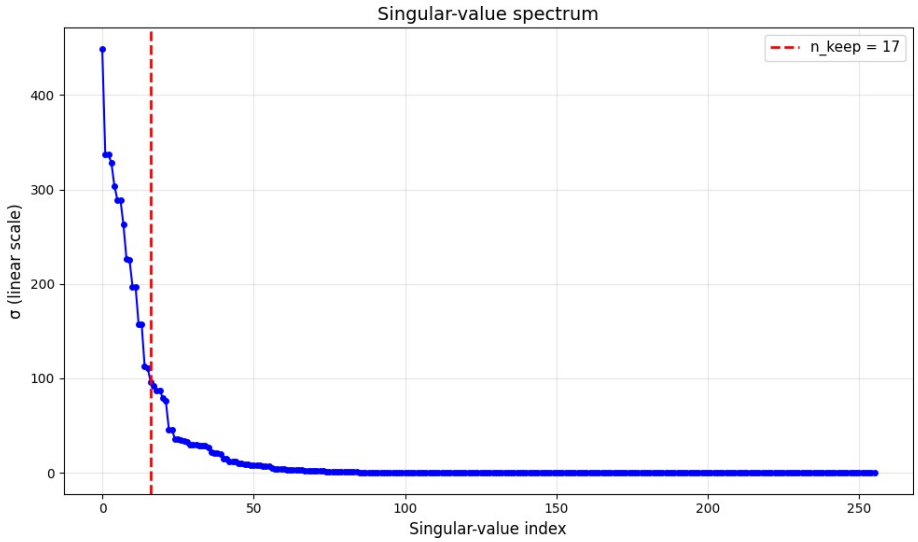

Figure 3.13 : Singular-value spectrum for the water-sphere test. The dashed red line marks the chosen cut-off $k_\alpha = 17$.

In this plot, the singular values $\{\sigma_i\}_{i=1}^{256}$ decay rapidly until index $i = 17$, after which they enter a long, slowly decaying tail. The pronounced "elbow" at $i = 17$ indicates that the first 17 singular values capture most of the operator's action on the data, while the remaining modes lie close to the numerical noise floor. If the cumulative energy curve is inspected (Fig. 3.13) according to Eq. (3.42), $E(17) \approx 0.90$, confirming that retaining 17 modes preserves 90% of the total spectral energy. Hence $k_\alpha = 17$ emerges as a natural truncation threshold.

$$E(k) \;=\; \frac{\sum_{i=1}^{k} \sigma_i^2}{\sum_{i=1}^{256} \sigma_i^2} \tag{3.42}$$

Beyond spectral analysis, an interactive slider was used to visualize the effect of varying k_α on the reconstructed contrast maps $|\delta\chi|$. Figure 3.14 shows interactive slider interface that allows user to change maximum value of the color scale and k_α. This allows better observation of the effect of the k_α on the image, and color scale variability allows for better visualization of the hemorrhage.

Figure 3.15 shows six reconstructions obtained for $k_\alpha = \{9, 17, 22, 60, 140, 256\}$. Too few singular values (e.g. $k_\alpha = 9$) blurs the inclusion, whereas too many (e.g. $k_\alpha = 256$) re-introduce noise and artefacts.

When $k_\alpha = 9$, the inclusion appears severely blurred and its peak amplitude is underestimated, indicating that too few modes lead to over-regularization and loss of spatial detail. At $k_\alpha = 17$, the hemorrhagic inclusion is sharply localized and the background speckle remains low, justifying this index as the optimal balance. Increasing k_α beyond 17 (e.g. $k_\alpha = 60$ or $k_\alpha = 140$) begins to re-introduce ringing artefacts around the antenna ring and raises the noise floor, while $k_\alpha = 256$ essentially recovers every noisy singular direction and produces a speckled, nearly random map. The slider-based exploration thus confirms that the elbow at $i = 17$ not only corresponds to 90% energy capture, but also yields the best qualitative trade-off between resolution and stability.

3.6.3 Test and updated on TSVD algorithm

In this step, we aimed to verify the accuracy and stability of our TSVD reconstruction pipeline using the simplest possible scenario. The goal was not to test advanced

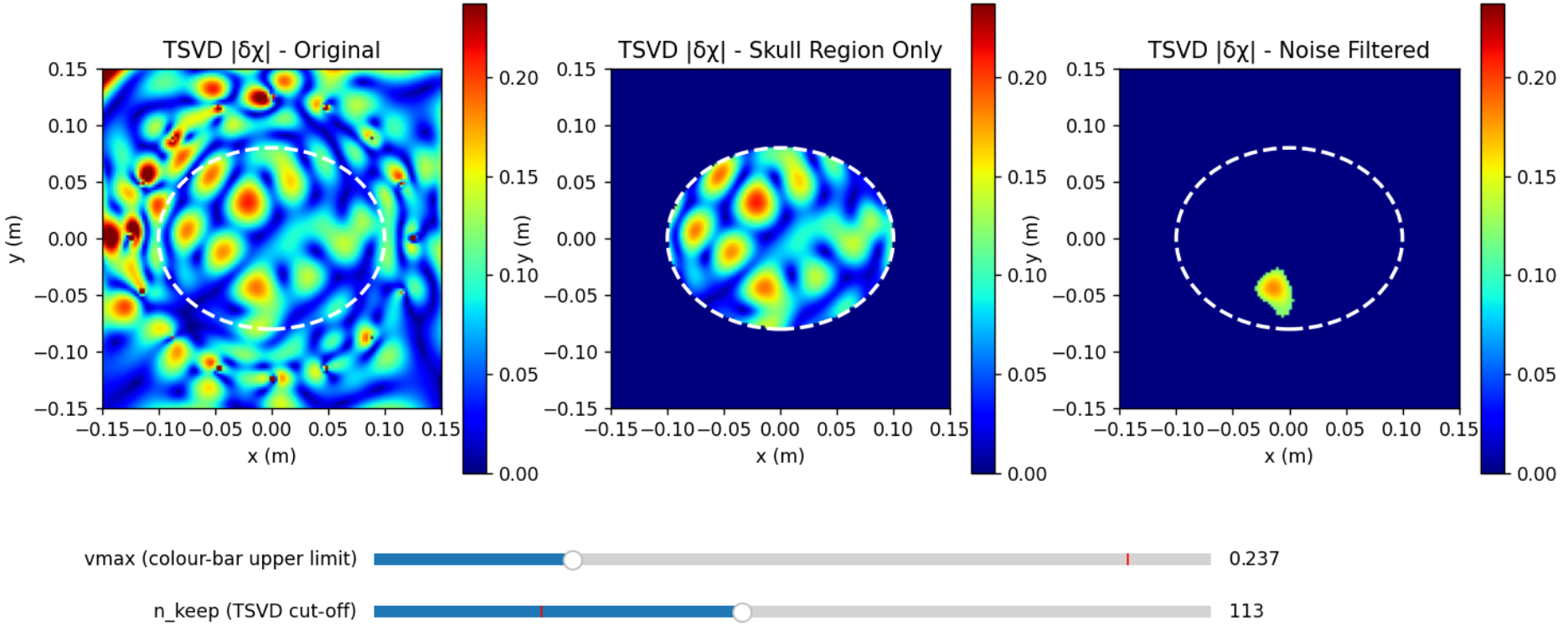

Figure 3.14 : User interface with changing color scale and k_α.

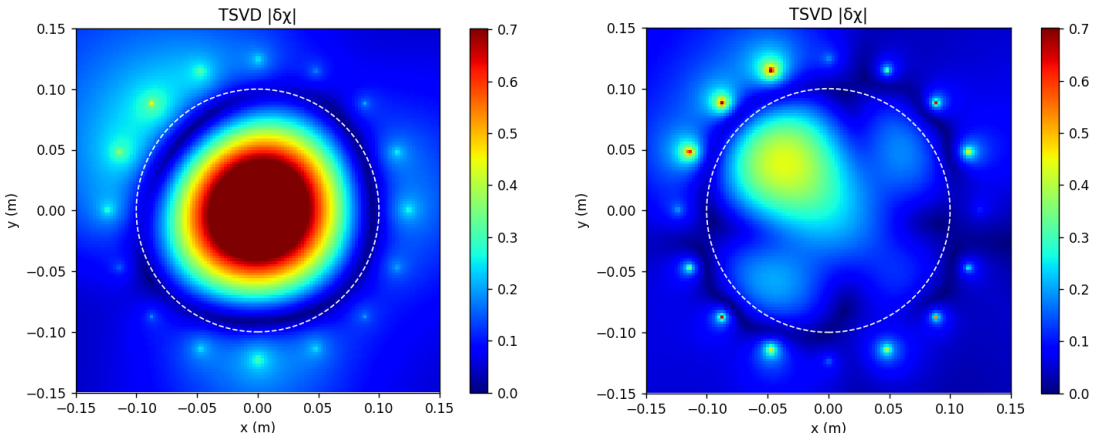

((a)) $k_\alpha = 9$ ((b)) $k_\alpha = 17$

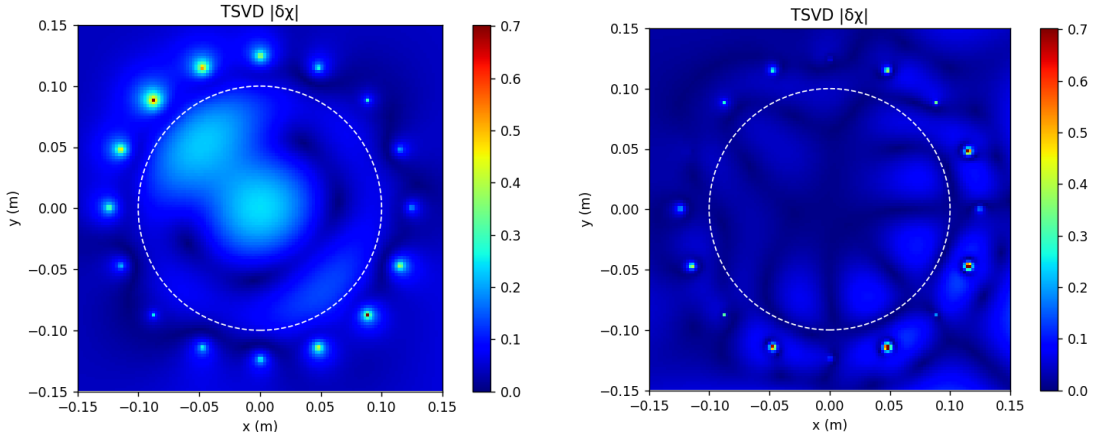

((c)) $k_\alpha = 22$ ((d)) $k_\alpha = 60$

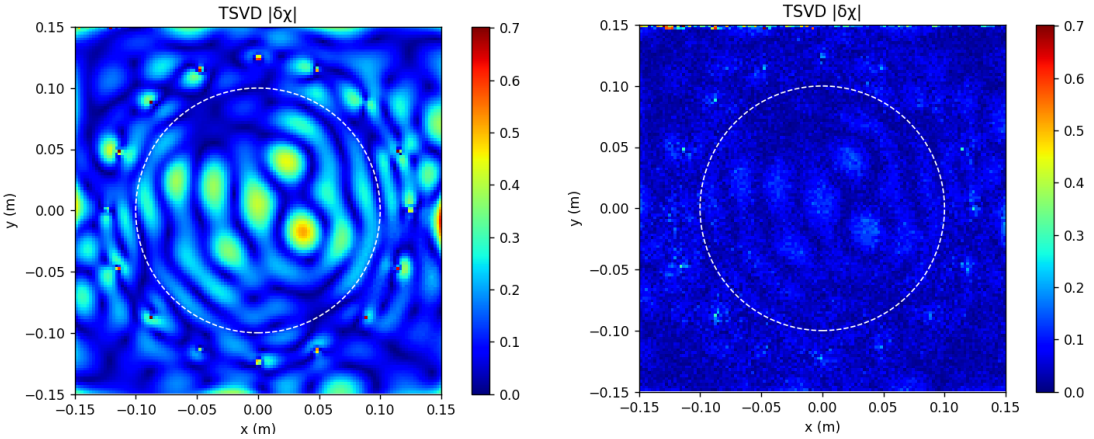

((e)) $k_\alpha = 140$ ((f)) $k_\alpha = 256$

Figure 3.15 : TSVD reconstructions $|\delta\chi|$ for increasing cutoff index.

model geometries or antenna variations, but simply to confirm that the code reads HFSS-generated scattering parameters, correctly assembles the forward operator, and produces a meaningful image when given controlled input data.

We set up two HFSS simulations: one with sixteen identical dipole antennas placed in free space, and one with a 30 mm-diameter water sphere ($\varepsilon_r = 80$, $\sigma = 1.5\,\mathrm{S/m}$) placed off-center. Both cases use the same antenna geometry given in Table 3.5.

Parameter	Value	Units
Dipole Length	16	cm
Antenna Array Radius (center to antenna)	12.5	cm
Dipole Arm Radius	1	mm
Feed Gap Width	1	mm
Number of Antennas	16	—
Operating Frequency	900	MHz

Table 3.5 : Antenna dimensions and parameters used in the simple test.

The practical consideration to model the hemorrhage as a 30 mm-diameter *water-sphere phantom* with $\varepsilon_r = 80$, $\sigma = 1.5$ S/m is although fresh blood exhibits a relative permittivity of about 61 and a bulk conductivity of roughly $1.5\,\mathrm{S/m}$ as shown in the Table 3.6.

Tissue	ε_r	σ [S/m]	Tissue	ε_r	σ [S/m]
Blood	61.36	1.538	Blood Vessel	44.77	0.6961
Brain Gray Matter	52.73	0.9423	Brain White Matter	38.89	0.5908
Dura	44.43	0.9611	Cerebrospinal Fluid	68.64	2.413
Bone Cortical	12.45	0.1433	Vitreous Humor	68.90	1.636

Table 3.6 : Representative dielectric properties of brain-related tissues at 900 MHz .

Hemorrhage phantom is deliberately modeled with $\varepsilon_r = 80$ while keeping $\sigma = 1.5\,\mathrm{S/m}$. The background brain model employed in subsequent sections has $\varepsilon_r \approx 41$, so raising the permittivity of the inclusion enlarges the dielectric contrast to $\Delta\varepsilon_r \approx 39$. This enhanced contrast strengthens the scattered field, making any shortcomings of the TSVD inversion more apparent and thereby providing a stringent, yet physiologically credible, test of the algorithm's accuracy and stability.

For each of the cases we exported S-parameters and applied our TSVD-based inversion code. Simulation setup can be observed in Figure 3.16.

In order to observe the effect of the dielectric phantom on the electric field in the antenna plane, a radial plane is inserted inside the antenna space as observed in the Figure 3.17.

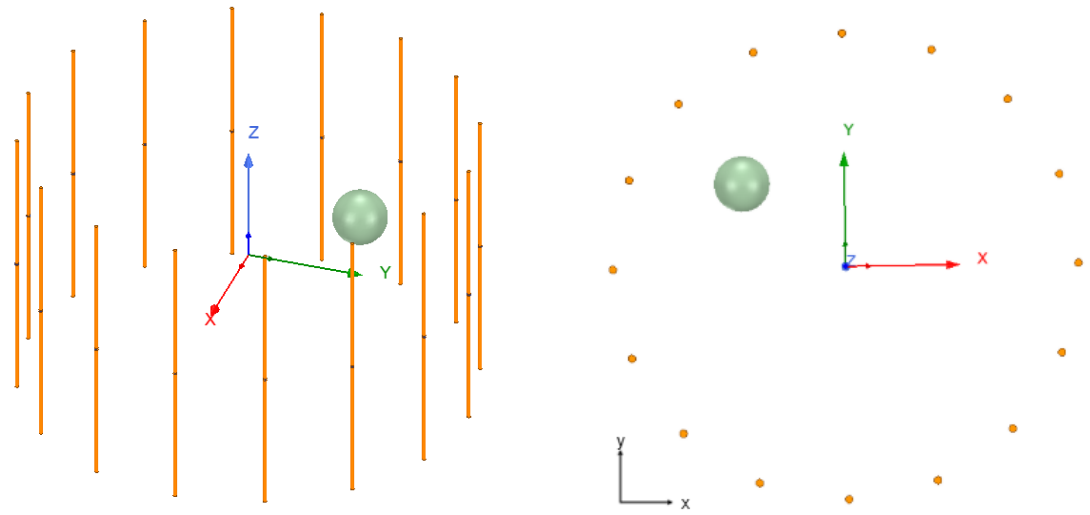

((a)) Sixteen-element dipole array with a sphere to simulate hemorrhage.

((b)) Top view of the setup with a diameter water sphere.

Figure 3.16 : HFSS simulation setup to test the TSVD implementation.

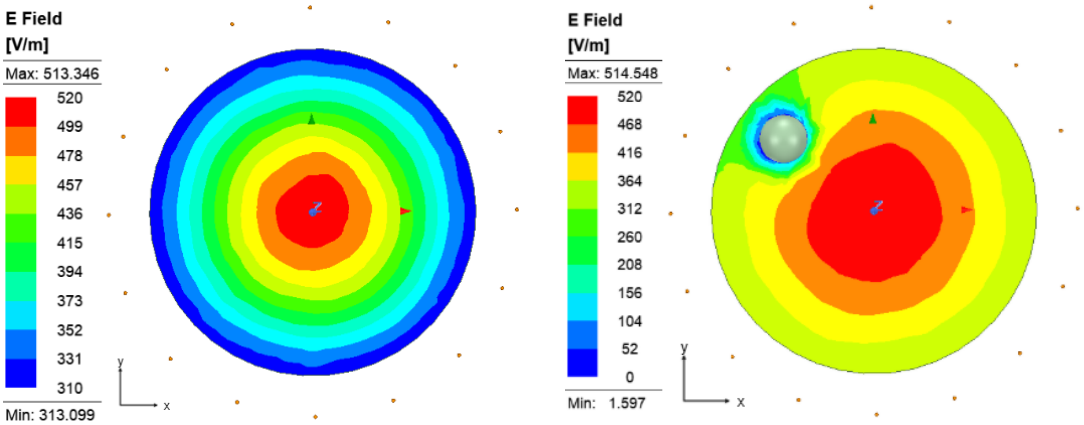

((a)) Baseline excitation without dielectric inclusion.

((b)) Perturbed field with hemorrhage phantom.

Figure 3.17 : Magnitude of the electric field in the antenna plane at TSVD implementation test setup.

At Figure 3.17(a), the field is almost radially symmetric, ranging from $E_{\max} \approx 5.1 \times 10^2\,\mathrm{V/m}$ at the center to $E_{\min} \approx 3.1 \times 10^2\,\mathrm{V/m}$ near the array. Inserting the high-permittivity, as observed in the Figure 3.17(b), lossy water sphere disrupts this symmetry. It draws energy from the incoming field because of higher displacement currents ($\varepsilon_r = 80$) and conductive losses ($\sigma = 1.5\,\mathrm{S/m}$). The field inside the sphere collapses to below $2\,\mathrm{V/m}$, while a high-gradient ring forms around its boundary. The resulting disturbance creates the non-zero multi-static scattering matrix that the TSVD algorithm uses. A correct inversion must therefore show a strong, high-contrast feature at the sphere's position and leave the surrounding area largely unchanged.

The quality of the reconstruction can be judged from the image in Figure 3.18. Using a cut-off index of $k_\alpha = 16$, the TSVD algorithm produces a single, well-focused hot-spot that coincides with the true position of the dielectric phantom, while keeping the rest of the domain clean of spurious artefacts.

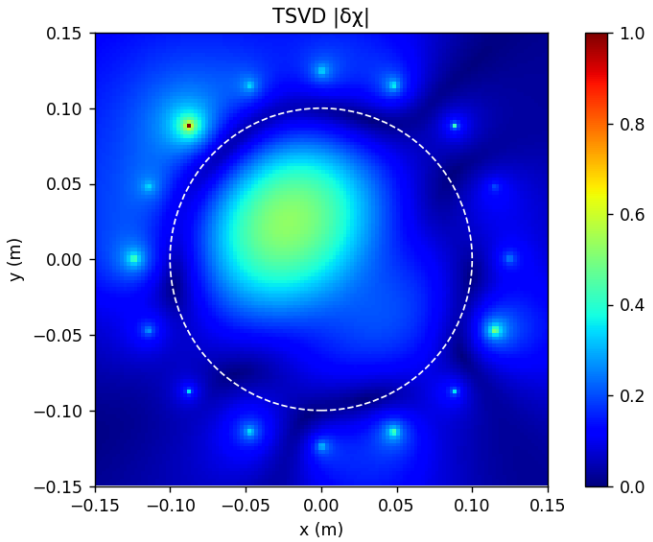

Figure 3.18 : Microwave imaging algorithm result, $k_\alpha = 16$.

The clear localisation and low background noise confirm that the Python pipeline correctly imports the HFSS S-parameters, builds the forward operator, and carries out a stable inversion. This successful test gives confidence that the same implementation will perform reliably on more complex head models in the following section.

After testing and validating that implementation in Python works flawlessly, some improvements on the visualization is conducted. In order to remove the bright artifacts that appear outside the head, caused by the antenna radiation, and to match the true outline of the skull, we added an elliptical mask, instead of a circular one. This sets every pixel lying outside a fitted ellipse to zero. The ellipse is chosen so that its major and minor axes follow the outer table of the skull in the cross-section used by the inversion code. Figure 3.19 compares the original reconstruction with the masked version.

The masked image retains all meaningful contrast variations inside the brain while eliminating the spurious high-intensity spots near the antennas. This simple post-processing step therefore improves interpretability without altering the underlying inversion algorithm.

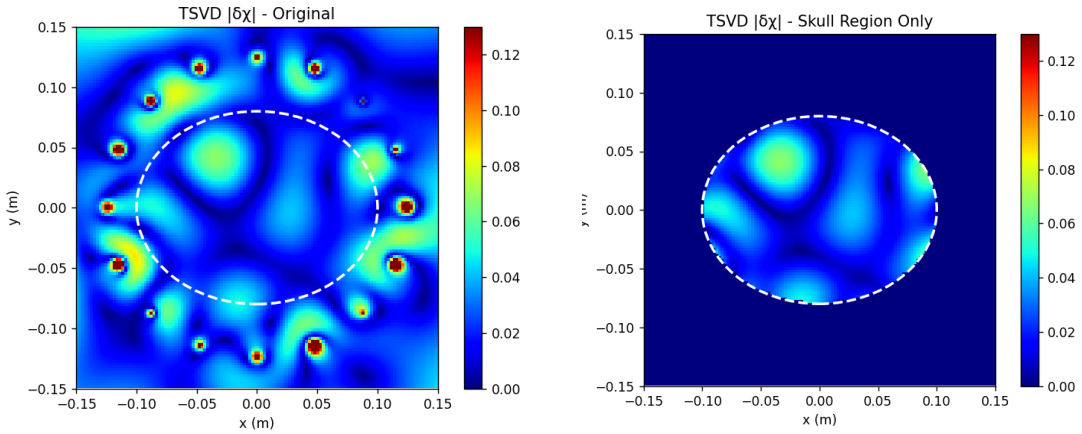

((a)) Original TSVD image without masking, antennas are visible.

((b)) Same image after applying the skull-shaped elliptical mask.

Figure 3.19 : Effect of the skull mask on the TSVD reconstruction.

3.6.4 Noise filtering and artefact suppression

Although the TSVD step localises the main dielectric contrast, the resulting image still exhibits speckle and weak antenna ring artefacts. Therefore, a filter is applied as a light post-processing block that preserves the inversion but improves visual clarity.

The first stage is a Gaussian smoothing. Let $I(x,y)$ denote the normalized magnitude image obtained from the TSVD. Convolution with a circularly symmetric Gaussian kernel (Eqs. (3.43), (3.44)) suppresses pixel-scale roughness.

$$G_\sigma(x,y) = \frac{1}{2\pi\sigma^2}\exp\left[-(x^2+y^2)/(2\sigma^2)\right] \tag{3.43}$$

$$I_s = I * G_\sigma \tag{3.44}$$

Here, the standard deviation σ is chosen between one and two pixels to balance noise removal against edge preservation. In the second stage, an adaptive threshold keeps only the brightest $100-p\%$ of the smoothed image. A percentile value T_p is computed and a binary mask is created as shown in the Eq. (3.45).

$$B = \{(x,y)\,|\,I_s(x,y) \geq T_p\} \tag{3.45}$$

Raising the percentile p makes the filter stricter. Stage three performs morphological cleaning. The mask B is opened and then closed with a circular structuring element S_r

of radius r as shown in the Eq. (3.46).

$$B_c = \big((B \ominus S_r) \oplus S_r\big) \oplus S_r \ominus S_r = (B \circ S_r) \bullet S_r \tag{3.46}$$

thereby eliminating isolated one-pixel flecks and filling pin-hole voids without eroding coherent regions.

Finally, connected-component pruning is used to make the image more spatially coherent. In the cleaned binary mask B_c, each separate region is called a component and labelled as $C_i \subset B_c$. We measure the size of each component using its area: $A_i = |C_i|$. The largest component, called $C_{\max}$, is kept. After selecting the components, we create a final binary mask M. This mask is applied to the smoothed image I_s, giving the final cleaned image as shown in the Eq. (3.47)

$$I_{\text{filt}} = I_s \cdot M \tag{3.47}$$

Increasing the smoothing parameter σ or the threshold percentile p reduces noise but may blur small features, such as thin haemorrhage rims. A larger radius r for the structuring element removes bigger gaps, but can also merge nearby areas. Figure 3.20 shows that the filter removes more than 85 % of the non-zero pixels while maintaining the lesion's peak contrast and shape, greatly easing clinical interpretation of the microwave image.

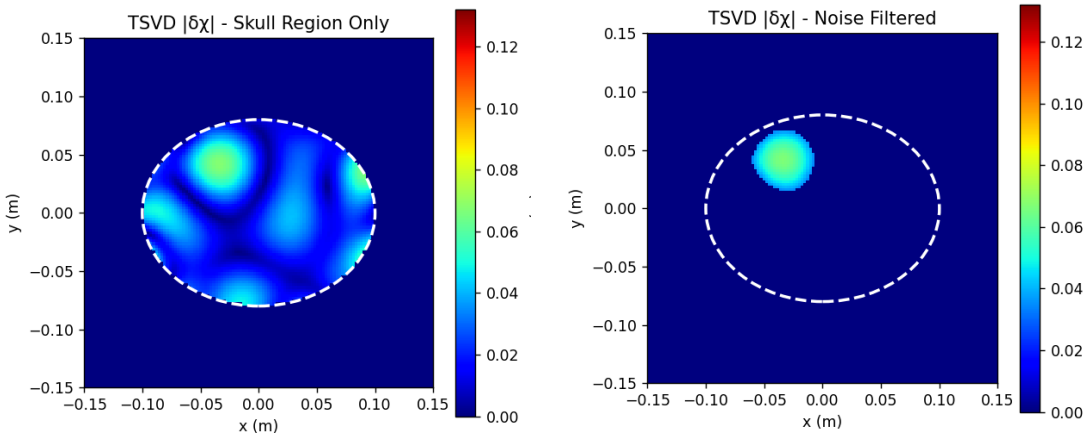

((a)) TSVD output after skull masking but before filtering.

((b)) Result after applying the four-stage noise filter.

Figure 3.20 : Effect of the adaptive noise filter.

Figure 3.21 shows the flow diagram of the algorithm. Each block lists the controlling parameter that can be tuned to trade noise suppression against lesion preservation.

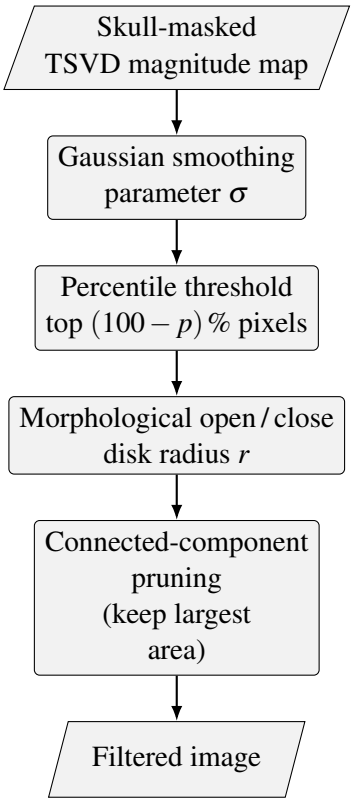

Figure 3.21 : Flow diagram of the noise-filtering algorithm applied after TSVD reconstruction.

Additionally, in order to provide ellipse dimensions in the image, the x and y dimensions of the head model simulated on HFSS are calculated. Calculated lengths are provided in Figure 3.22.

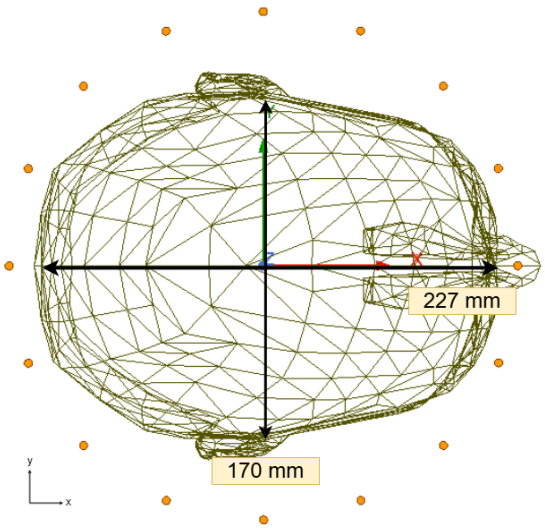

Figure 3.22 : Dimensions of head model used in simulations in order to determine ellipse dimensions used in the image.

4. RESULTS AND DISCUSSION

4.1 Geometric Quadrant Definition

In order to describe the locations of intracranial hemorrhages, we divide the head cross-section into four quadrants using a standard Cartesian coordinate system. Let (x, y) be a point in the plane:

- **Quadrant I:** $x > 0$, $y > 0$ (upper right)
- **Quadrant II:** $x < 0$, $y > 0$ (upper left)
- **Quadrant III:** $x < 0$, $y < 0$ (lower left)
- **Quadrant IV:** $x > 0$, $y < 0$ (lower right)

We will refer to any hemorrhage by its quadrant number. For example, a lesion at $(+a, +b)$ lies in Quadrant I, while one at $(-a, -b)$ lies in Quadrant III. Quadrant locations are provided in the Figure 4.1.

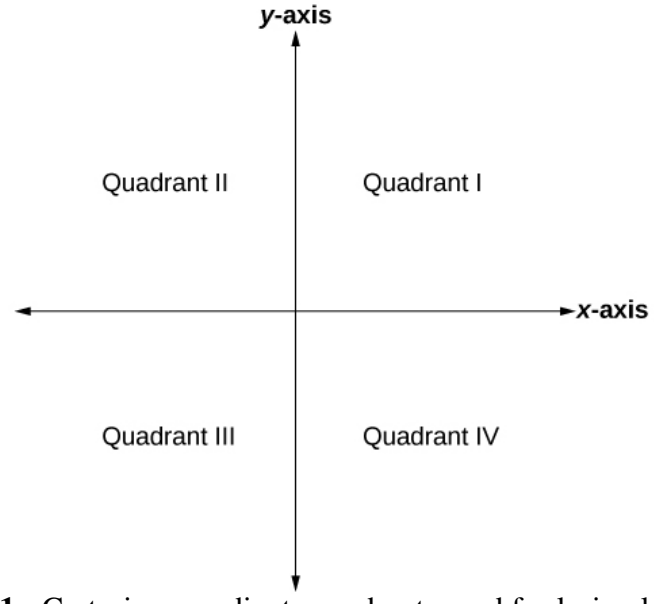

Figure 4.1 : Cartesian coordinate quadrants used for lesion localization.

4.2 Impact of Brain Conductivity on Imaging Performance

4.2.1 Realistic conductivity case: $\sigma = 0.9$ S/m

In this case the brain is assigned its true bulk conductivity of $\sigma = 0.9$ S/m. We excite the head phantom at $f = 900$ MHz with sixteen dipole antennas and reconstruct the lesion image using the truncated-SVD (TSVD) algorithm. With the lossy case, recovering focal spots corresponding to intracranial hemorrhages is possible but these reconstructions are heavily contaminated by noise and artefacts.

To understand the loss mechanism, let E_0 be the electric field amplitude at the source and let $E(d)$ be its amplitude after travelling a distance d through tissue. The field decays exponentially, as explained in the Eq. (4.1).

$$E(d) \;=\; E_0\, e^{-\alpha d} \tag{4.1}$$

Here the attenuation constant α can be represented as shown in the Eq. (4.2).

$$\alpha \;=\; \sqrt{\pi f \mu_0 \sigma} \tag{4.2}$$

As an example for $d = 0.10$ m, the ratio of received to transmitted field can be shown in the Eqs. (4.3) and (4.4).

$$\alpha \approx \sqrt{\pi \times 9 \times 10^8 \times 4\pi \times 10^{-7} \times 0.9} \;\approx\; 56.5 \text{ m}^{-1} \tag{4.3}$$

$$\frac{E(d)}{E_0} \;=\; e^{-\alpha d} \;\approx\; e^{-5.65} \;\approx\; 3.5 \times 10^{-3}. \tag{4.4}$$

This means less than 0.5 % of the transmitted field reaches the far side of the brain. The remaining signal lies just above the noise floor, producing low-contrast, grainy images that hinder reliable lesion localization. This result shows that, while penetration is not completely blocked, realistic conductivity still degrades image quality significantly compared to an ideal lossless case.

4.2.2 Lossless brain approximation: $\sigma = 0$

In this case, the brain conductivity is set to zero. Without attenuation, the electric field is propagated without decay as shown in the Eq. (4.5).

$$E(d) = E_0\, e^{-\alpha d} \quad \longrightarrow \quad E(d) = E_0 \quad (\text{since } \alpha = 0) \tag{4.5}$$

Because $\sigma = 0$, the attenuation constant can be found as shown in the Eq. (4.6).

$$\alpha = \sqrt{\pi f \mu_0 \sigma} = 0 \tag{4.6}$$

Attenuation is found as zero, and the transmitted field is received at full amplitude by every antenna. As a result, the most of the total spectral energy is captured by the first fifty singular values. The ratio of received to transmitted field in the lossless case can be found as shown in the Eq. (4.7)

$$\frac{E(d)}{E_0} = e^{-0 \cdot d} = 1 \tag{4.7}$$

This confirms that no signal strength is lost regardless of the path length d. These ideal reconstructions demonstrate that millimetre-scale localization of intracranial hemorrhages can be achieved by the TSVD pipeline when conductive damping is absent. This lossless model is therefore provided as an ideal-world benchmark for future hardware or algorithmic enhancements.

4.3 Simulation Setups

4.3.1 Case labeling

In order to organize the various tests, each configuration is assigned a case label C_i. Two conductivity conditions are considered. Non-conductive cases use the suffix $\sigma = 0$, giving labels C_{i,σ_0}. Conductive cases use the suffix $\sigma = 0.9$, giving labels $C_{i,\sigma}$.

Thus, for example, C_{1,σ_0} is Case 1 with zero conductivity, while $C_{1,\sigma}$ is the same geometry under realistic conductivity. All simulated cases are provided in Table 4.1.

4.3.2 Cut-off index (k_α) selection for scenarios

The cut-off index k_α is determined by inspecting the singular value spectrum both for conductive and non-conductive cases. Also interactive k_α slider is utilized to determine which cut-off value can be chosen and singular-value spectrum is to determine which

Case	Description	Conductivity
C_{1,σ_0}	No blood inclusion	$\sigma = 0$
C_{2,σ_0}	15 cm radius hemorrhage in Quadrant I	$\sigma = 0$
C_{3,σ_0}	22 cm radius hemorrhage in Quadrant I	$\sigma = 0$
C_{4,σ_0}	Dual hemorrhage: 15 cm in QI, 22 cm in QIII	$\sigma = 0$
$C_{1,\sigma}$	No blood inclusion	$\sigma = 0.9\,\mathrm{S/m}$
$C_{2,\sigma}$	15 cm radius hemorrhage in Quadrant I	$\sigma = 0.9\,\mathrm{S/m}$
$C_{3,\sigma}$	22 cm radius hemorrhage in Quadrant I	$\sigma = 0.9\,\mathrm{S/m}$
$C_{4,\sigma}$	Dual hemorrhage: 15 cm in QI, 22 cm in QIII	$\sigma = 0.9\,\mathrm{S/m}$

Table 4.1 : Simulated cases under non-conductive and conductive conditions.

singular-values are redundant. These singular value spectra is provided in Figure 4.2 and Figure 4.3. For non-conductive case clear "knee" in the spectrum has appeared between values of 50 and 55. Accordingly, $k_\alpha = 52$ was adopted for all non-conductive reconstructions.

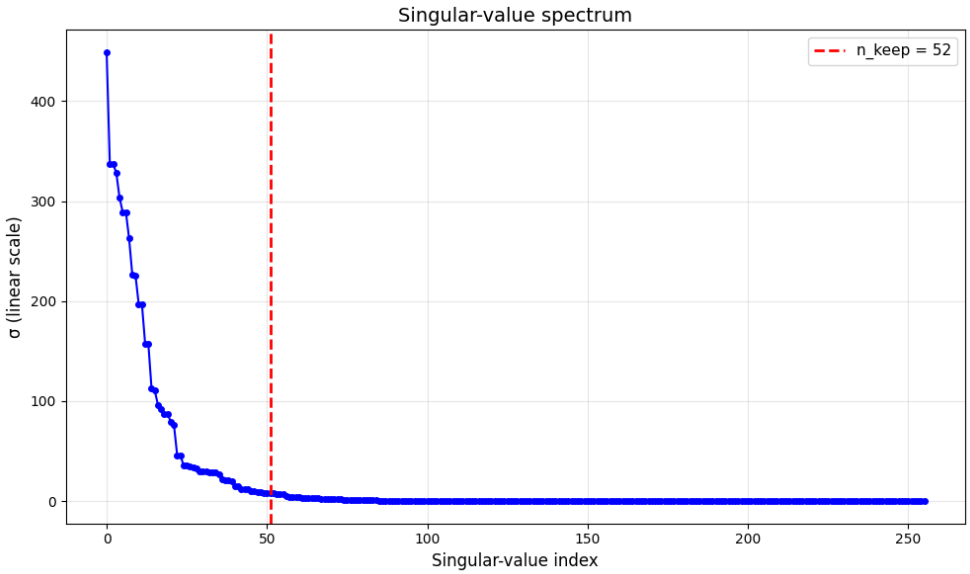

Figure 4.2 : Singular-value spectrum for the non-conductive case, $k_\alpha = 52$.

Similarly, for conductive case, the spectrum showed a abrupt change of slope at the range of 30 and 35. Accordingly, cut-off index value of $k_\alpha = 33$ is chosen for the conductive scenarios.

4.4 Medical Hemorrhage Scenarios

In this work, five clinically inspired hemorrhage scenarios are evaluated under two conductivity conditions: non-conductive ($\sigma = 0$) and realistic conductive ($\sigma =$

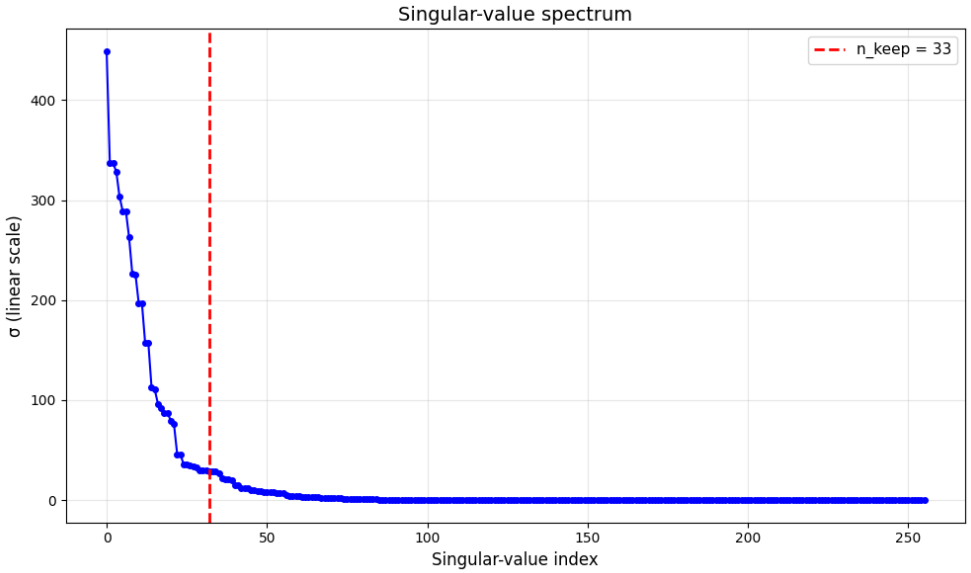

Figure 4.3 : Singular-value spectrum for the conductive case, $k_\alpha = 33$.

0.9 S/m). Each scenario is assigned a label S_{i,σ_0} for the non-conductive case and $S_{i,\sigma}$ for the conductive case. Table 4.2 summarizes these ten simulated configurations.

Scenario	Description	Conductivity
$S_{1,\sigma_0/\sigma}$	Single intracranial hemorrhage vs healthy brain ($C_{1,\sigma_0/\sigma}$ vs. $C_{2,\sigma_0/\sigma}$)	0, 0.9 S/m
$S_{2,\sigma_0/\sigma}$	Enlarged intracranial hemorrhage vs healthy brain ($C_{1,\sigma_0/\sigma}$ vs. $C_{3,\sigma_0/\sigma}$)	0, 0.9 S/m
$S_{3,\sigma_0/\sigma}$	Progression of intracranial hemorrhage ($C_{2,\sigma_0/\sigma}$ vs. $C_{3,\sigma_0/\sigma}$)	0, 0.9 S/m
$S_{4,\sigma_0/\sigma}$	Multiple intracranial hemorrhages vs healthy brain ($C_{1,\sigma_0/\sigma}$ vs. $C_{4,\sigma_0/\sigma}$)	0, 0.9 S/m
$S_{5,\sigma_0/\sigma}$	New hemorrhage in multi-lesion case ($C_{2,\sigma_0/\sigma}$ vs. $C_{4,\sigma_0/\sigma}$)	0, 0.9 S/m

Table 4.2 : Overview of medical hemorrhage scenarios.

4.4.1 Scenario 1: Single intracranial hemorrhage

In this scenario, a single spherical hemorrhage of 15 cm radius is placed in the first quadrant (Quadrant I) of the brain cross-section. Clinically, this models an isolated focal bleed in the frontal-right region, as might occur after a localized head trauma or small vessel rupture. The aim is to determine whether the TSVD imaging pipeline can detect and localize this lesion under both ideal (lossless) and realistic (lossy) conductivity conditions.

Figure 4.4 presents the lossless case (C_{2,σ_0} vs. C_{1,σ_0}). Panel (a) shows the head phantom and the 16-dipole antenna array. Panels (b) and (c) display the simulated electric-field magnitude for the healthy brain and the hemorrhage case, respectively, when $\sigma = 0$. The raw TSVD reconstruction of the contrast function $|\delta_\chi|$ is given in panel (d), with the skull-region detail in (e). After spatial filtering, the final TSVD image (f) shows a clear, high-contrast focus exactly at the lesion location.

Figure 4.5 gives the corresponding results for the lossy case ($C_{2,\sigma}$ vs. $C_{1,\sigma}$). Although the hemorrhage focus remains visible, the reconstruction is contaminated by elevated background noise and artefacts. Panels (b) and (c) illustrate that realistic conductivity ($\sigma = 0.9\,\mathrm{S/m}$) attenuates the field amplitude, and panels (d)–(f) demonstrate how noise degrades the TSVD output compared to the idealized case.

Together, these images confirm that while TSVD can localize a single intracranial hemorrhage with millimetre-scale accuracy in the absence of loss (Figure 4.4), realistic brain conductivity substantially reduces image contrast and clarity (Figure 4.5).

4.4.2 Scenario 2: Enlarged intracranial hemorrhage

In this scenario, the hemorrhage radius is increased from 15 cm to 22 cm in the first quadrant, modeling a more extensive focal bleed. Clinically, this represents a growing hematoma that may exert greater mass effect and risk of raised intracranial pressure.

Figure 4.6 shows the lossless case (C_{3,σ_0} vs. C_{1,σ_0}). Panel (a) illustrates the head phantom and antenna arrangement. In panel (b), the electric-field map for the healthy brain appears uniform, while panel (c) reveals a broader high-field region around the enlarged lesion when $\sigma = 0$. The raw TSVD reconstruction (d) displays a larger contrast area, and panels (e) and (f) confirm that the filtered TSVD image precisely outlines the expanded hemorrhage.

Figure 4.7 presents the corresponding lossy results ($C_{3,\sigma}$ vs. $C_{1,\sigma}$). Compared to the ideal case, panels (b) and (c) exhibit reduced field amplitude under realistic conductivity. The TSVD outputs in (d)–(f) are more diffuse and noisier, yet the enlarged lesion remains identifiable despite the degraded contrast.

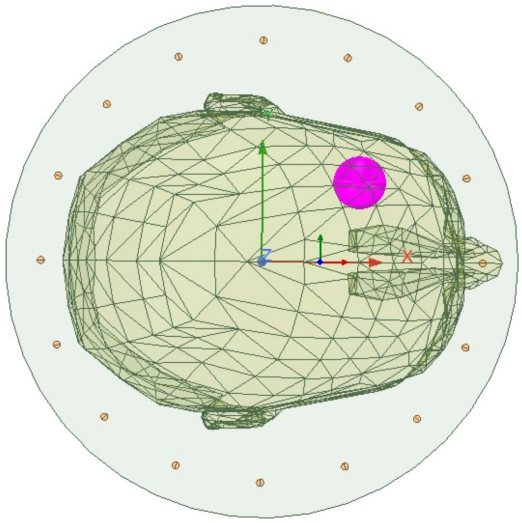

((a)) Simulation setup.

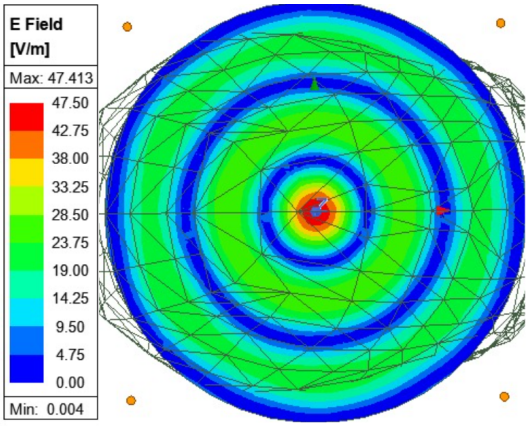

((b)) E field of the cross-section for C_{1,σ_0}.

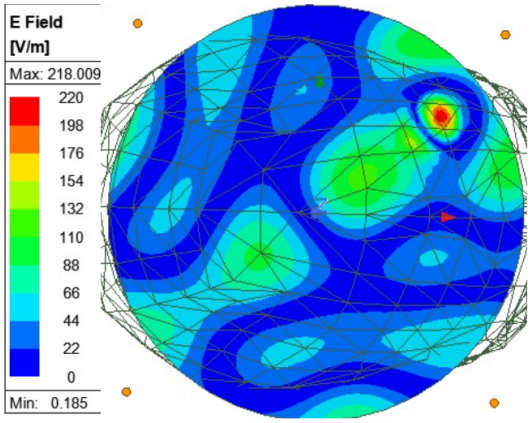

((c)) E field of the cross-section for C_{2,σ_0}.

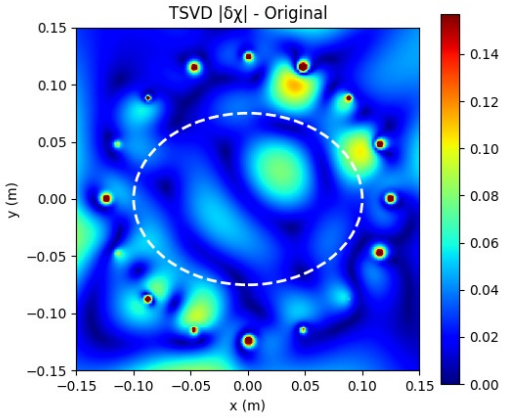

((d)) TSVD $|\delta_\chi|$.

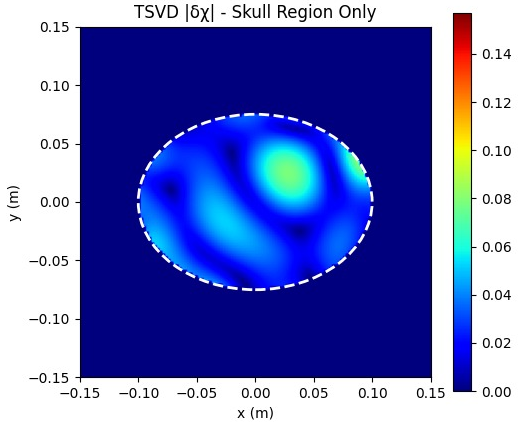

((e)) TSVD $|\delta_\chi|$ skull region.

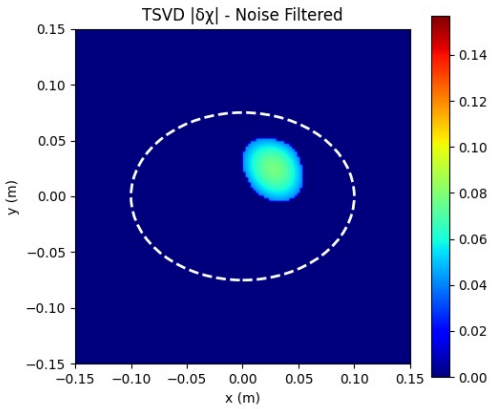

((f)) TSVD $|\delta_\chi|$ filtered.

Figure 4.4 : Imaging for single intracranial hemorrhage (Scenario 1, lossless case).

These images demonstrate that lesion size directly influences the reconstructed focus: a larger hemorrhage yields a wider TSVD signature, but realistic losses still impair clarity (lossless in Figure 4.6, lossy in Figure 4.7).

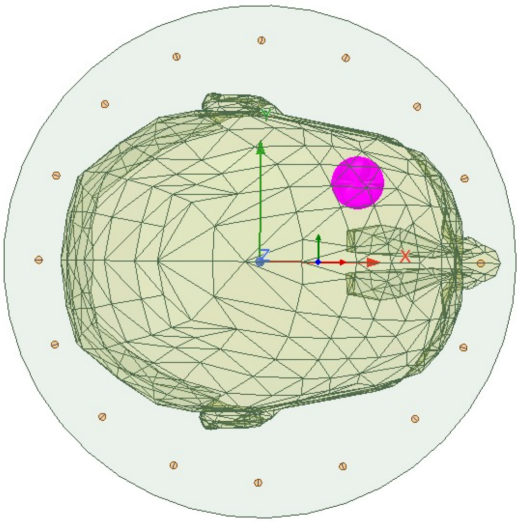

((a)) Simulation setup.

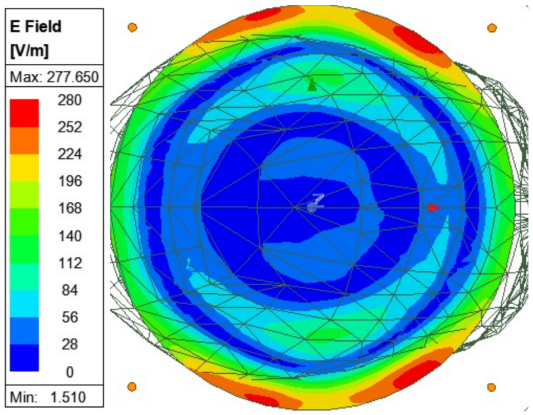

((b)) E field of the cross-section for $C_{1,\sigma}$.

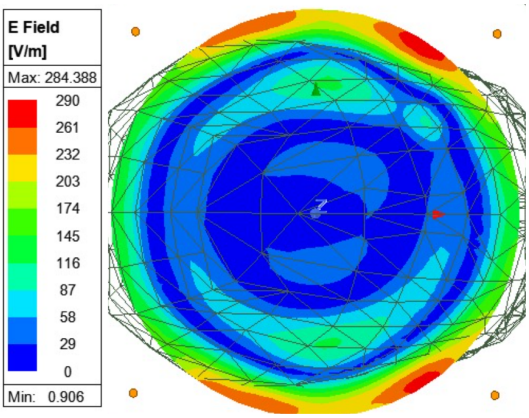

((c)) E field of the cross-section for $C_{2,\sigma}$.

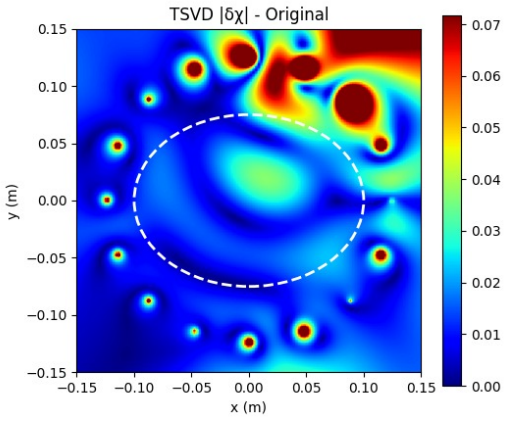

((d)) TSVD $|\delta_\chi|$.

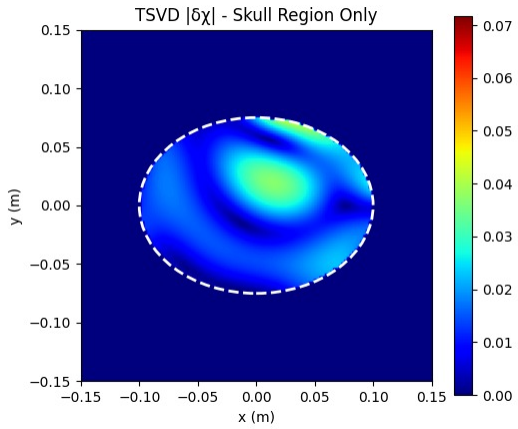

((e)) TSVD $|\delta_\chi|$ skull region.

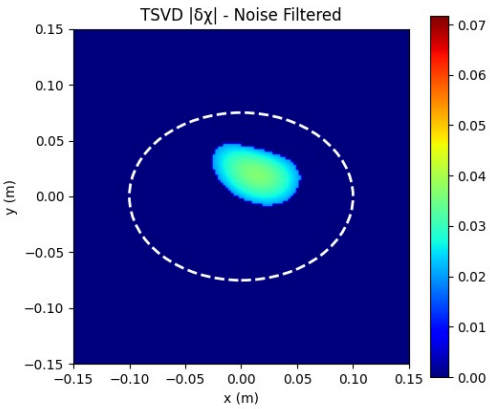

((f)) TSVD $|\delta_\chi|$ filtered.

Figure 4.5 : Imaging for single intracranial hemorrhage (Scenario 1, lossy case).

4.4.3 Scenario 3: Progression of intracranial hemorrhage

In this scenario, the hemorrhage is allowed to grow from a 15 cm radius to a 22 cm radius within the same first quadrant location. Medically, this models the progression

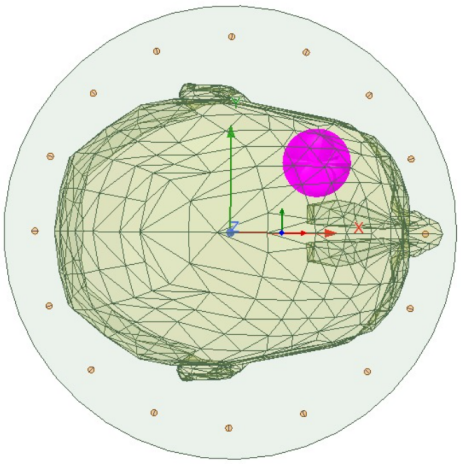

((a)) Simulation setup.

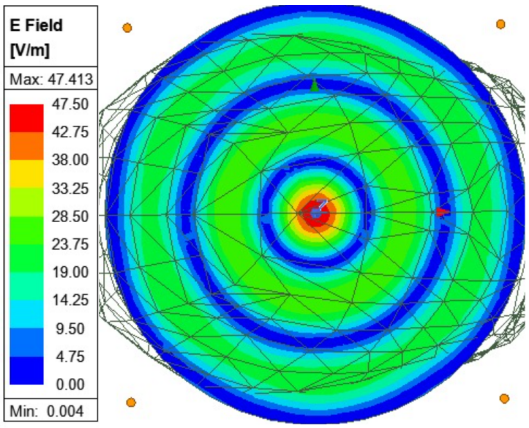

((b)) E field of the cross-section for C_{1,σ_0}.

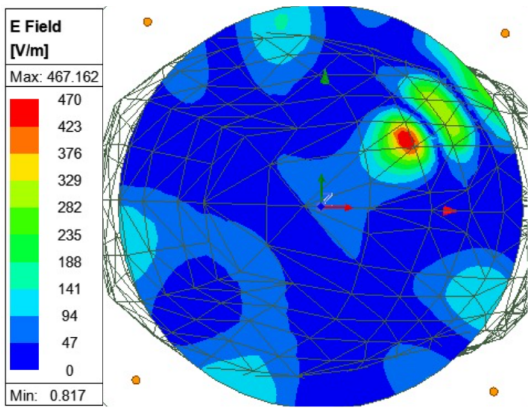

((c)) E field of the cross-section for C_{3,σ_0}.

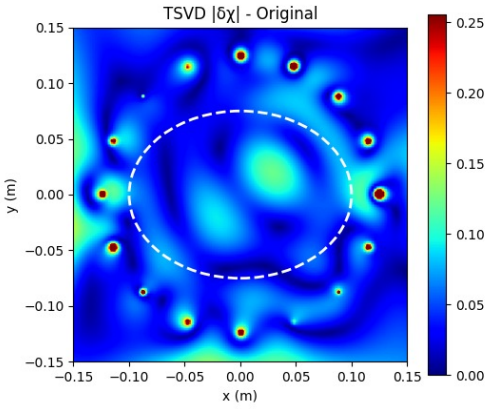

((d)) TSVD $|\delta_\chi|$.

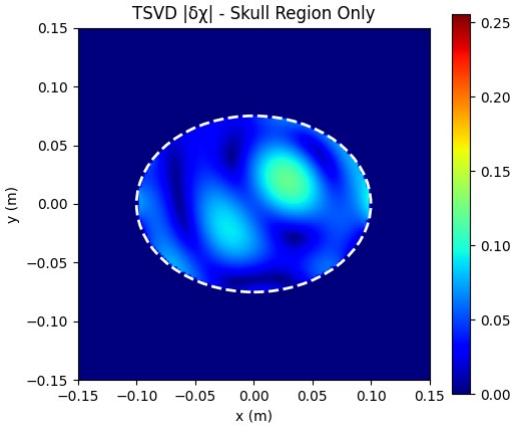

((e)) TSVD $|\delta_\chi|$ skull region.

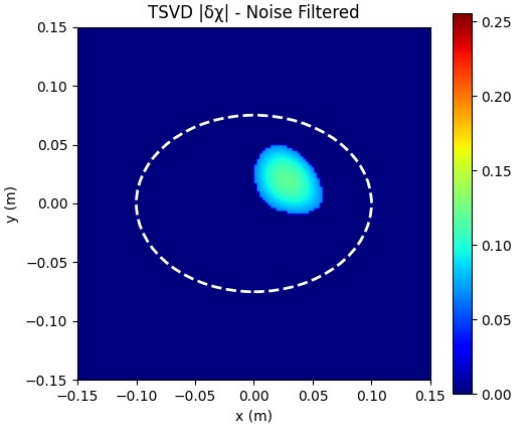

((f)) TSVD $|\delta_\chi|$ filtered.

Figure 4.6 : Imaging for enlarged intracranial hemorrhage (Scenario 2, lossless case).

of a hematoma over time, which can increase intracranial pressure and worsen patient prognosis if not detected promptly. The goal is to assess whether the TSVD imaging pipeline can distinguish between the smaller and larger bleed volumes under both ideal and realistic conductivity conditions.

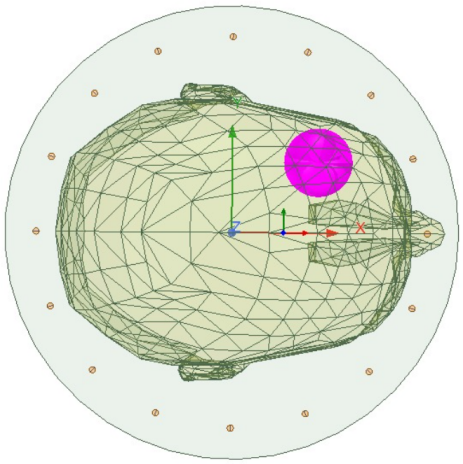

((a)) Simulation setup.

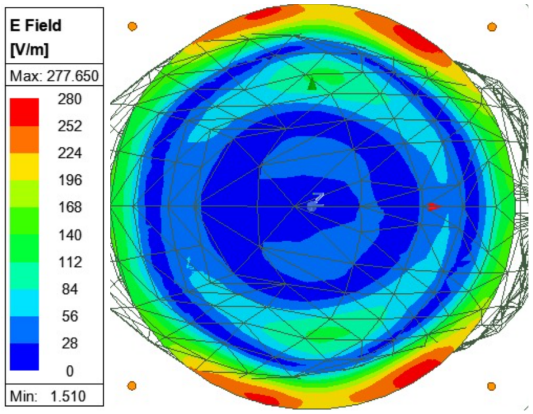

((b)) E field of the cross-section for $C_{1,\sigma}$.

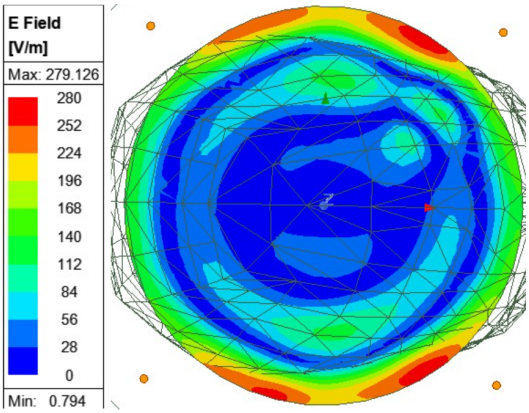

((c)) E field of the cross-section for $C_{3,\sigma}$.

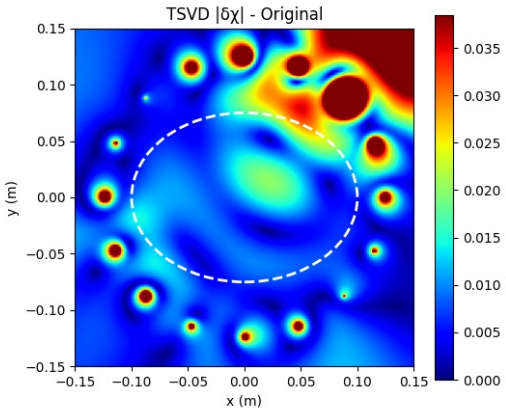

((d)) TSVD $|\delta_\chi|$.

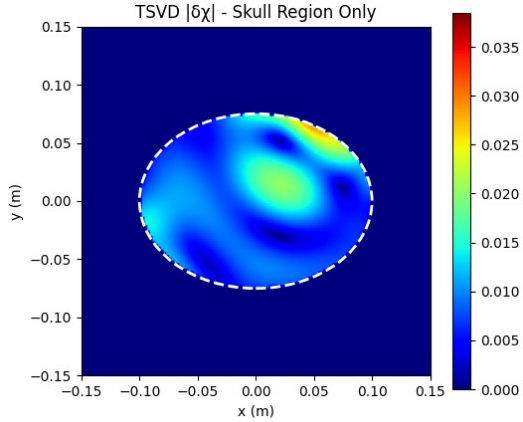

((e)) TSVD $|\delta_\chi|$ skull region.

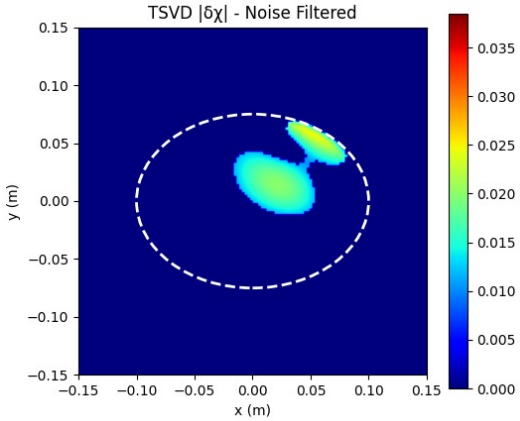

((f)) TSVD $|\delta_\chi|$ filtered.

Figure 4.7 : Imaging for enlarged intracranial hemorrhage (Scenario 2, lossy case).

Figure 4.8 shows the lossless case (C_{3,σ_0} vs. C_{2,σ_0}). Panel (a) depicts the head phantom and antenna layout. Panels (b) and (c) compare the electric-field magnitude for the 15 cm and 22 cm lesions, respectively, when $\sigma = 0$. The raw differential TSVD reconstruction in panel (d) highlights the shell of growth between the two bleed sizes,

and panels (e) and (f) confirm that after skull-region isolation and noise filtering, the annular focus matches the incremental volume of the hemorrhage.

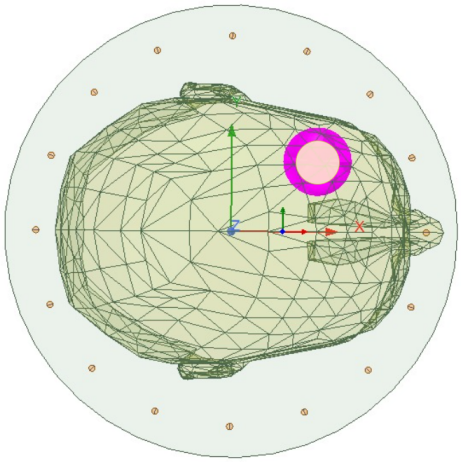

((a)) Simulation setup.

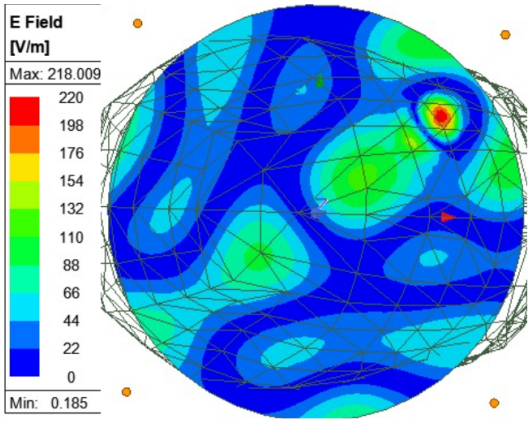

((b)) E field of the cross-section for C_{2,σ_0}.

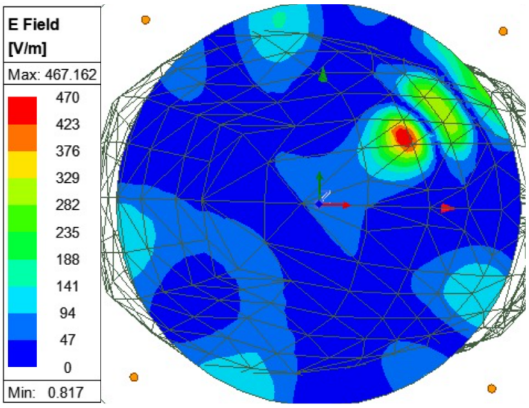

((c)) E field of the cross-section for C_{3,σ_0}.

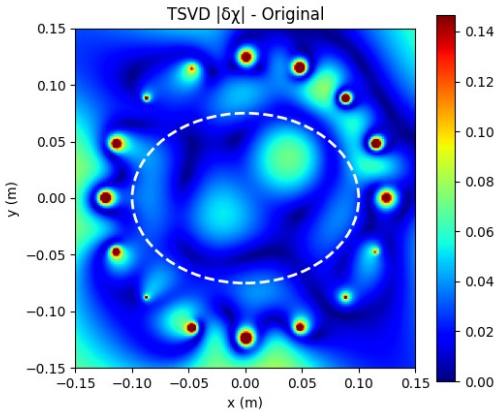

((d)) TSVD $|\delta_\chi|$.

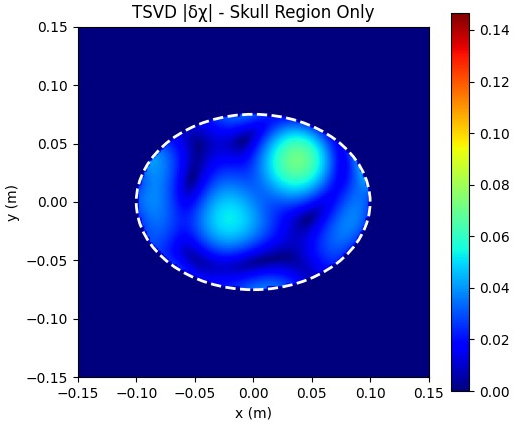

((e)) TSVD $|\delta_\chi|$ skull region.

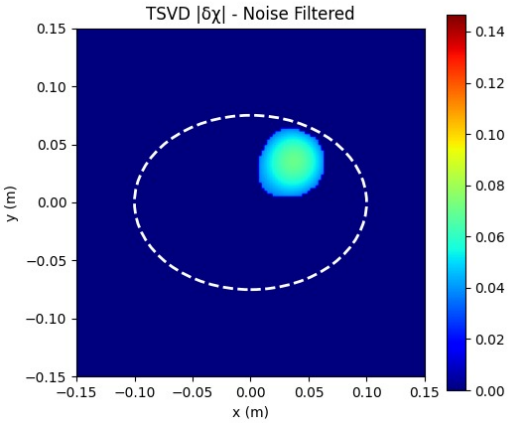

((f)) TSVD $|\delta_\chi|$ filtered.

Figure 4.8 : Imaging for progression of intracranial hemorrhage (Scenario 3, lossless case).

Figure 4.9 presents the corresponding lossy results ($C_{3,\sigma}$ vs. $C_{2,\sigma}$). As shown in panels (b) and (c), realistic conductivity attenuates both fields, and the TSVD outputs in panels (d)–(f) are noisier and lower in contrast. Nevertheless, the annular growth signature remains discernible, demonstrating the method's sensitivity to changes in hemorrhage volume even under lossy conditions.

4.4.4 Scenario 4: Multiple intracranial hemorrhage

In this scenario, two separate hematomas are present simultaneously: a 15 cm radius bleed in Quadrant I and a 22 cm radius bleed in Quadrant III. Medically, this models a patient with multifocal injury, such as diffuse head trauma or coagulopathy leading to multiple bleeding sites. The objective is to test whether the TSVD imaging pipeline can resolve and localize both lesions under ideal and realistic conductivity conditions.

Figure 4.10 illustrates the lossless case (C_{4,σ_0} vs. C_{1,σ_0}). In panel (a), the head phantom and antenna layout are shown. Panels (b) and (c) compare the electric-field magnitude for the healthy brain and the dual-lesion case, respectively, when $\sigma = 0$. The raw TSVD contrast map in panel (d) reveals two distinct intensity peaks corresponding to each hemorrhage. Panel (e) focuses on the skull region, and panel (f) presents the filtered TSVD image, where both lesions are clearly resolved with minimal artefacts.

Figure 4.11 shows the corresponding lossy results ($C_{4,\sigma}$ vs. $C_{1,\sigma}$). As seen in panels (b) and (c), realistic conductivity attenuates the fields, and the TSVD outputs in panels (d)–(f) exhibit increased background noise. Despite this, two separate foci remain visible, demonstrating that the method retains enough spatial diversity to distinguish multiple hemorrhages even under lossy conditions.

4.4.5 Scenario 5: Additional hemorrhage with existing lesion

In this scenario, a secondary hemorrhage of 22 cm radius is introduced in Quadrant III alongside the original 15 cm lesion in Quadrant I. Medically, this models a patient who develops a new bleed adjacent to an existing hematoma, increasing intracranial pressure and complicating treatment planning. The aim is to verify that the TSVD pipeline can cancel the common lesion signature and isolate only the new hemorrhage.

Figure 4.12 presents the lossless case (C_{4,σ_0} vs. C_{2,σ_0}). Panel (a) shows the head phantom with both lesion locations marked. In panels (b) and (c), the electric-field

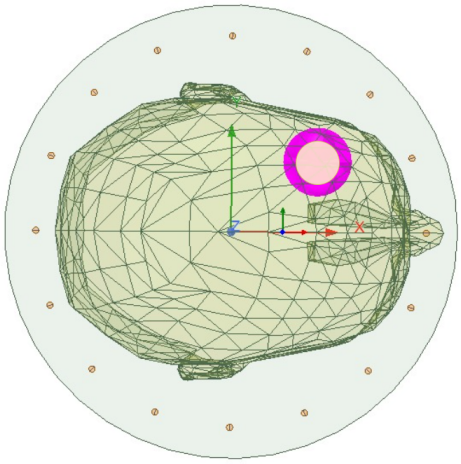

((a)) Simulation setup.

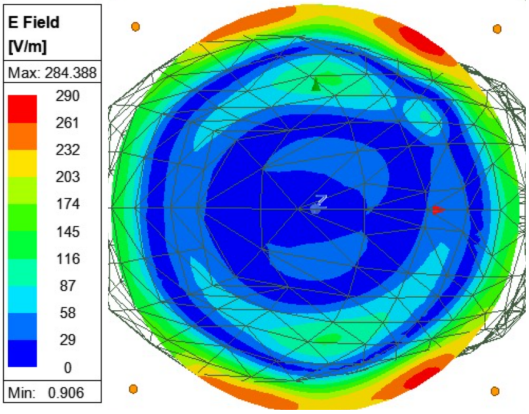

((b)) E field of the cross-section for $C_{2,\sigma}$.

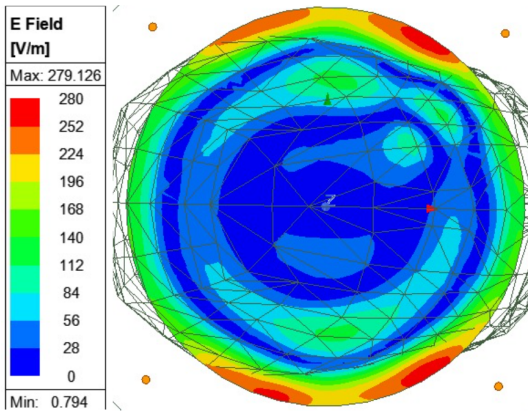

((c)) E field of the cross-section for $C_{3,\sigma}$.

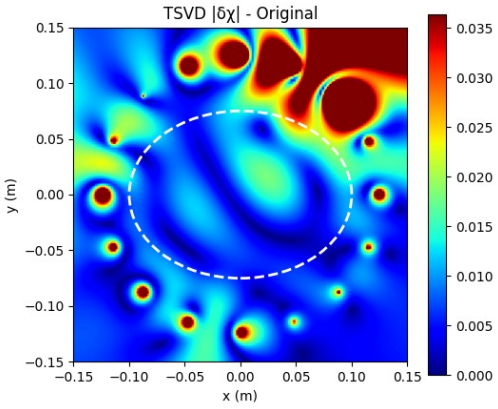

((d)) TSVD $|\delta_\chi|$.

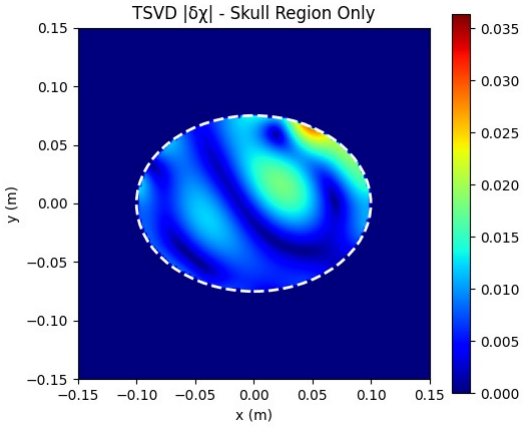

((e)) TSVD $|\delta_\chi|$ skull region.

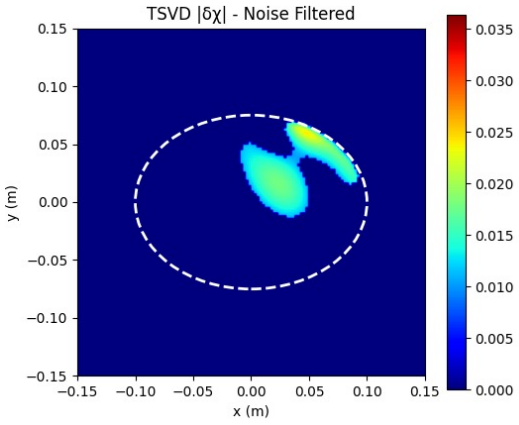

((f)) TSVD $|\delta_\chi|$ filtered.

Figure 4.9 : Imaging for progression of intracranial hemorrhage (Scenario 3, lossy case).

magnitude is compared for the single-lesion and dual-lesion cases when $\sigma = 0$. The raw differential TSVD map in panel (d) highlights the added bleed, and panels (e)

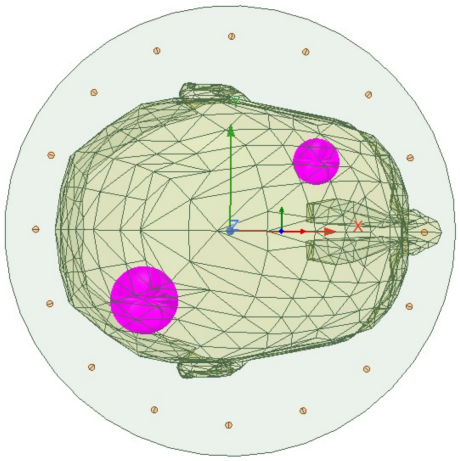

((a)) Simulation setup.

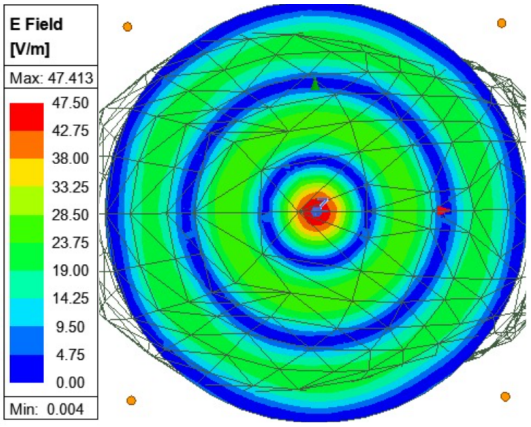

((b)) E field of the cross-section for C_{1,σ_0}.

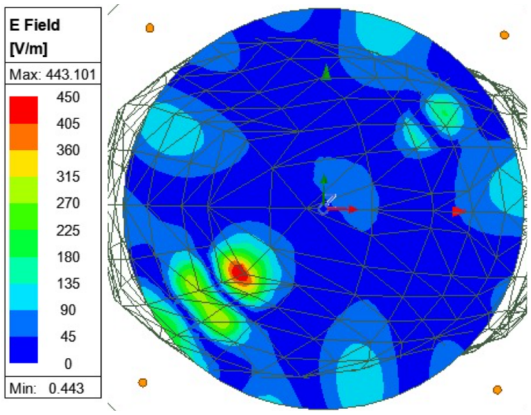

((c)) E field of the cross-section for C_{4,σ_0}.

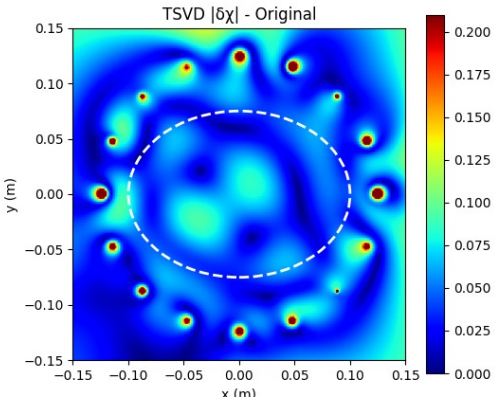

((d)) TSVD $|\delta_\chi|$.

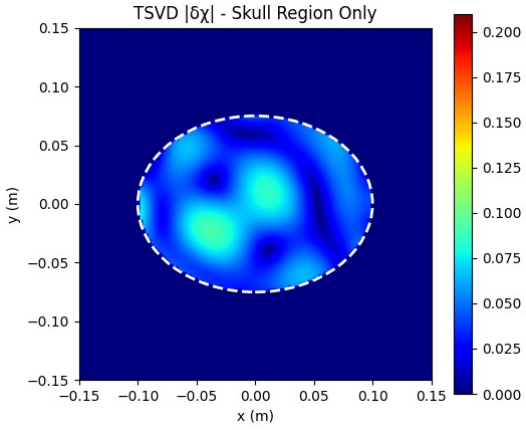

((e)) TSVD $|\delta_\chi|$ skull region.

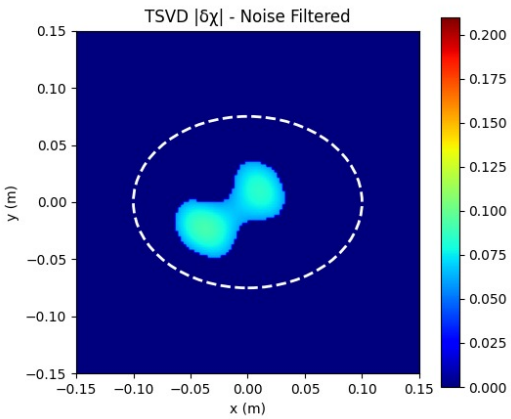

((f)) TSVD $|\delta_\chi|$ filtered.

Figure 4.10 : Imaging for multiple intracranial hemorrhage (Scenario 4, lossless case).

and (f) demonstrate that, after skull-region isolation and noise filtering, only the new hemorrhage remains visible.

Figure 4.13 shows the corresponding lossy results ($C_{4,\sigma}$ vs. $C_{2,\sigma}$). As shown in panels (b) and (c), realistic brain conductivity attenuates both fields, and the TSVD

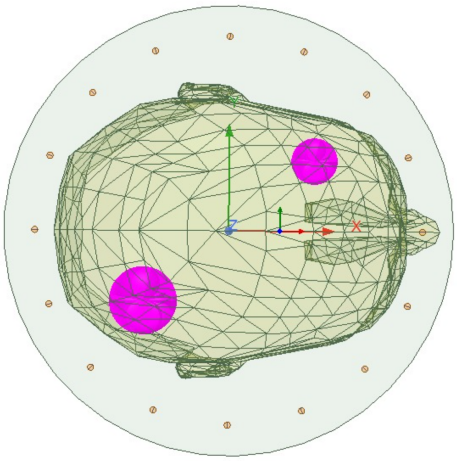

((a)) Simulation setup.

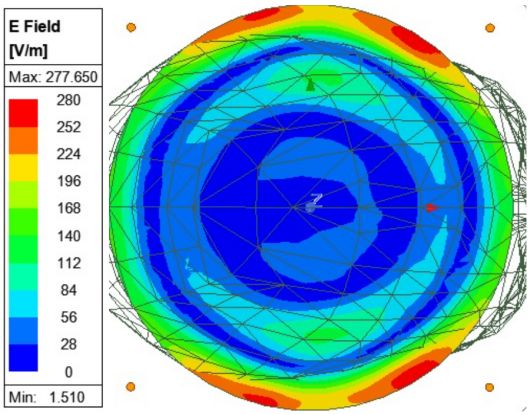

((b)) E field of the cross-section for $C_{1,\sigma}$.

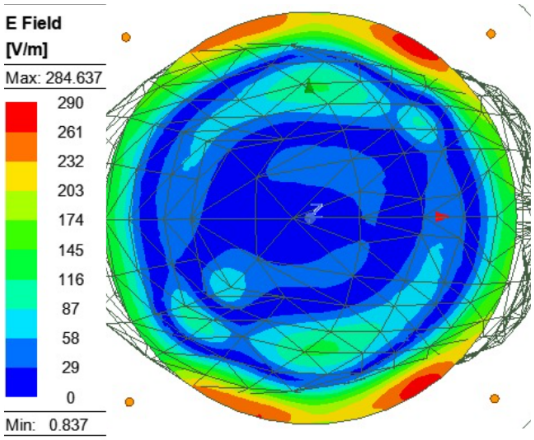

((c)) E field of the cross-section for $C_{4,\sigma}$.

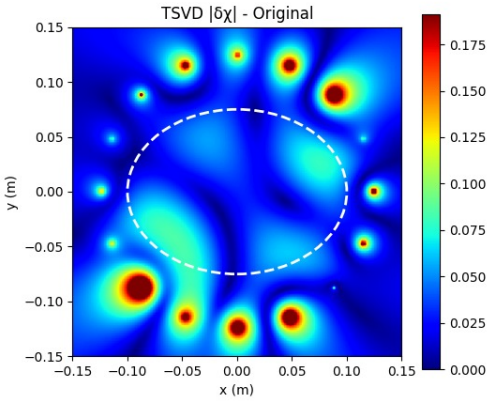

((d)) TSVD $|\delta_\chi|$.

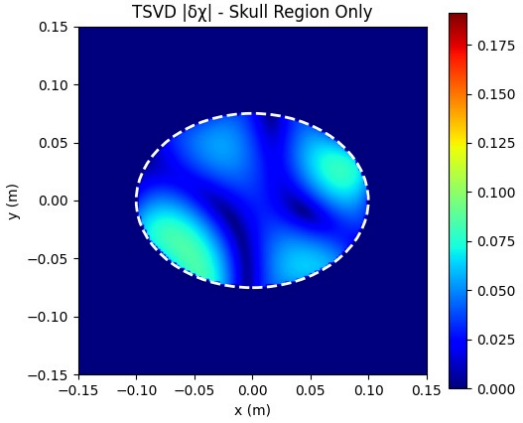

((e)) TSVD $|\delta_\chi|$ skull region.

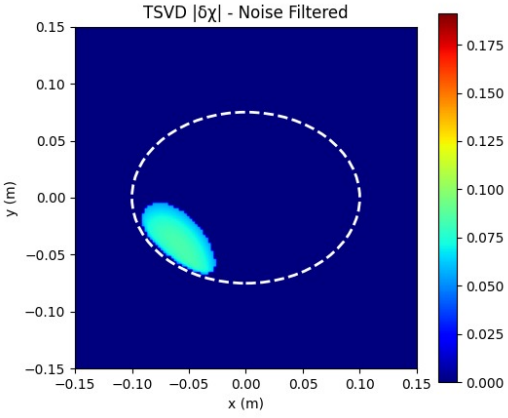

((f)) TSVD $|\delta_\chi|$ filtered.

Figure 4.11 : Imaging for multiple intracranial hemorrhage (Scenario 4, lossy case).

reconstructions in panels (d)–(f) are noisier. Nevertheless, the additional hemorrhage is still clearly localized, confirming the robustness of the differential imaging approach under lossy conditions.

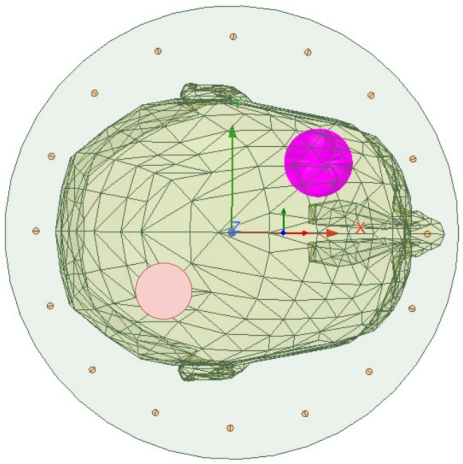

((a)) Simulation setup.

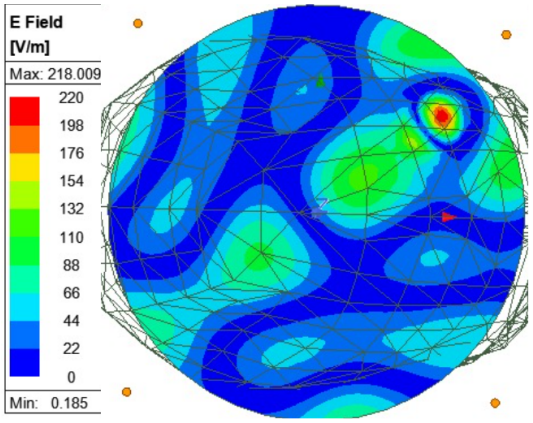

((b)) E field of the cross-section for C_{2,σ_0}.

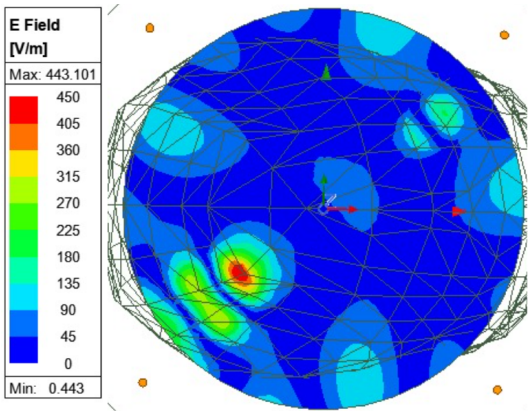

((c)) E field of the cross-section for C_{4,σ_0}.

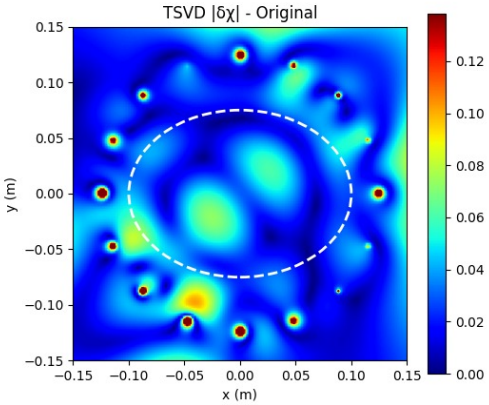

((d)) TSVD $|\delta_\chi|$.

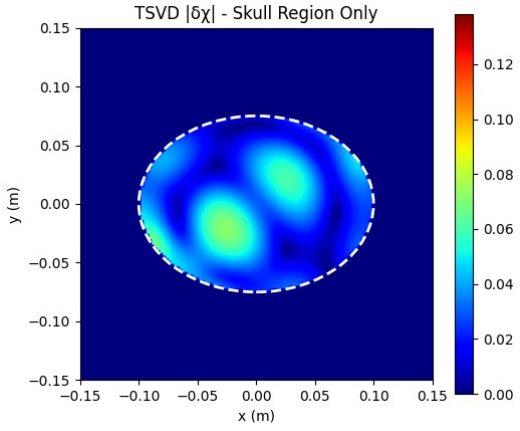

((e)) TSVD $|\delta_\chi|$ skull region.

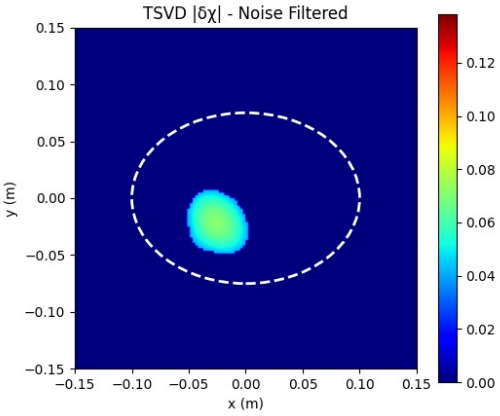

((f)) TSVD $|\delta_\chi|$ filtered.

Figure 4.12 : Imaging for additional hemorrhage with existing lesion (Scenario 5, lossless case).

4.5 Discussion of the Results

The imaging results obtained through the truncated-SVD (TSVD) inversion reveal several key insights into the feasibility and limitations of our 16-antenna, 900 MHz

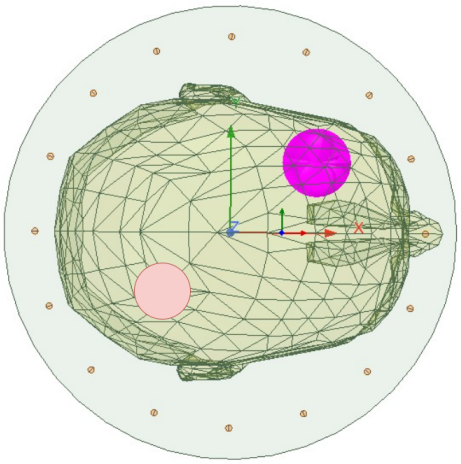

((a)) Simulation setup.

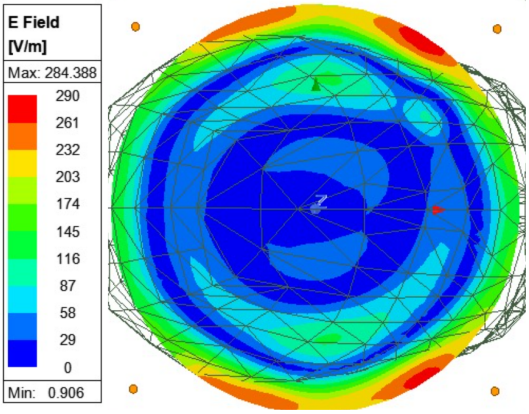

((b)) E field of the cross-section for $C_{2,\sigma}$.

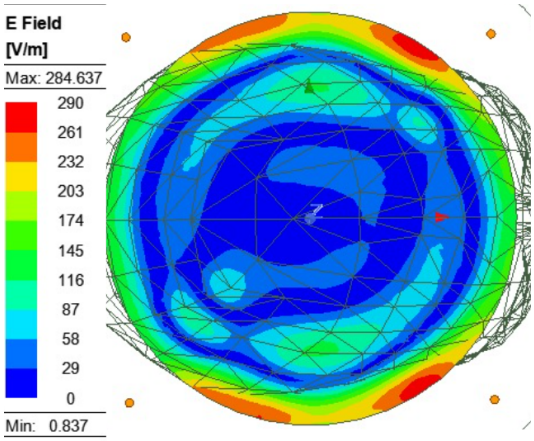

((c)) E field of the cross-section for $C_{4,\sigma}$.

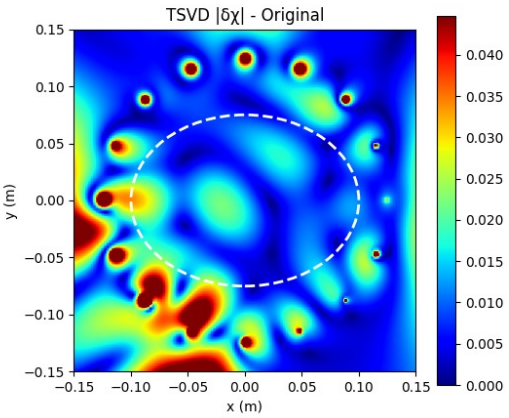

((d)) TSVD $|\delta_\chi|$.

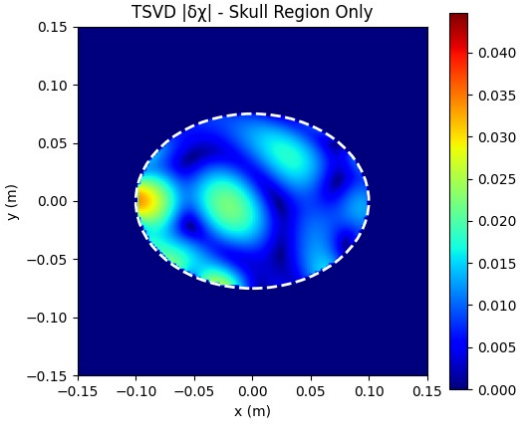

((e)) TSVD $|\delta_\chi|$ skull region.

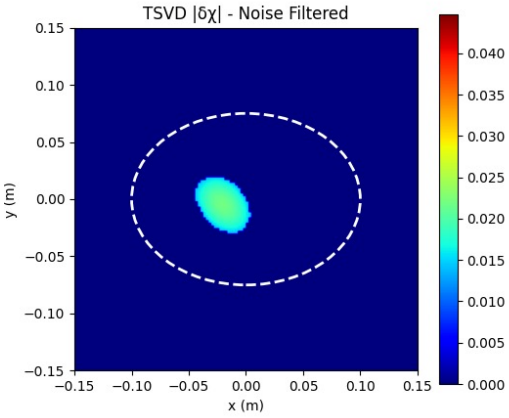

((f)) TSVD $|\delta_\chi|$ filtered.

Figure 4.13 : Imaging for additional hemorrhage with existing lesion (Scenario 5, lossy case).

system. First, the simulated electric-field distributions (Figures 4.4–4.13, panels (b) and (c)) directly illustrate how variations in tissue conductivity and lesion geometry shape the raw data. In the lossless cases ($\sigma = 0$), the field penetrates uniformly and

high-order modes remain strong; this creates clear, concentric patterns that the TSVD algorithm can exploit to recover sharp, high-contrast images of each hemorrhage. By contrast, under realistic conductivity ($\sigma = 0.9$ S/m), the field amplitudes are heavily attenuated and the higher modes collapse toward the noise floor. As shown in the lossy-case panels, the recovered $|\delta_\chi|$ maps still capture the general location of each lesion, but contrast is reduced and background artefacts become prominent.

The application of a skull-region mask and spatial noise filtering markedly improves the practical utility of the TSVD reconstructions. In all scenarios, the raw TSVD output (panel (d) in each figure) contains ringing artefacts and false foci arising from residual coupling between antennas and random noise. Many of these spurious features are eliminated when the map is limited to the inside of the skull (panel (e)), as they are primarily found outside the region of interest. The reconstruction is further smoothed by a subsequent low-pass filter (panel (f)), which suppresses high-frequency noise while maintaining the millimeter-scale lesion focus. The combined result is a sharp rise in the lesion contrast-to-noise ratio; even in cases where there is loss, the final filtered images enable clear localization of both single and multiple hemorrhages. Overall, the findings show that intracranial lesions can be accurately visualized using TSVD inversion in an idealized, lossless setting when combined with the proper pre- and post-processing. The method still localizes hemorrhages under realistic conductivity, but at the expense of increased artifacts and diminished contrast. These results point to two obvious areas for development: incorporating model-based regularization to recover contrast from shallow modes and increasing measurement diversity (for example, by adding more antennas or frequency sweeps) to strengthen the singular-value spectrum. The lossless-case reconstructions continue to be a useful standard for evaluating new hardware and algorithmic improvements until such developments are put into practice.

5. REALISTIC CONSTRAINTS

5.1 Practical Implementation

The TSVD-based through-wall microwave imaging system for brain hemorrhage detection requires careful hardware and coupling environment design in order to be implemented practically. Using permittivity $\varepsilon_r = 20$ and very low loss (conductivity $\sigma \approx 0.005$ S/m), an ideal cylindrical matching medium (radius = 145 mm) was simulated. Actually, reaching a comparable matching medium and integrating the antenna array into it calls both mechanical and material aspects. Using a matching medium is critical to bridge the impedance mismatch between air ($\varepsilon_r \approx 1$) and the high-dielectric head tissues (ε_r on the order of 40) at 0.9 GHz [9]. Strong interface reflections at the skin boundary would arise without a coupling medium, so restricting microwave penetration into the brain. Surrounding the head with an intermediary-permittivity medium (on the scale of 10–30) reflections are blocked and more energy is transferred into the tissue. A matching medium also enhances the coupling between dipole antennas and the head, so raising the net signal strength obtained from internal targets. An intermediate dielectric homogenizes the near-field around the head, so lowering spurious multipath effects and streamlining the modeling assumptions of the imaging technique. These advantages are absolutely essential for the detection of deep, tiny hemorrhagic lesions as our simulations show.

5.1.1 Matching medium considerations

It is very difficult to find or create a physical medium with low conductivity and $\varepsilon_r \approx 20$ at about 0.9 GHz. A number of potential materials and mixtures are listed in Table 5.1, together with an estimate of their dielectric characteristics at 900 MHz. Composite solids and single-component liquids are both taken into account. . Notably, pure water has a very high permittivity (≈ 80) and moderate loss at 0.9 GHz (effective $\sigma \sim$ 1–2 S/m) [9], so it greatly overmatches tissue and causes substantial attenuation.

Pure glycerin, a common coupling liquid in microwave imaging setups, has lower permittivity ($\approx$ 40–45) but is still rather lossy (microwave relaxation equivalent to $\sigma \approx 1$ S/m). Neither water nor glycerol alone achieves $\varepsilon_r \approx 20$. Instead, mixtures of polar liquids can be tuned to intermediate permittivities. For example, *water–alcohol solutions* can cover a broad permittivity range (ethanol–water or methanol–water mixtures can achieve $\varepsilon_r \approx$ 10–70 by adjusting ratios). An alcohol-rich mixture (e.g., 80% ethanol + 20% water) could yield $\varepsilon_r \approx$ 15–25 with relatively low conductivity. Similarly, ethylene glycol or propylene glycol mixed with water offers pure glycols with $\varepsilon_r \approx$ 30–37 and moderate loss; by adjusting the water content, ε_r can be tuned as required. A *water–glycerol* mixture (with glycerol fraction $>$ 50%) has $\varepsilon_r \approx$ 40–70, too high for our target, making glycerol more suited for tissue phantoms than low-permittivity matching layers. Alternatively, combining water/glycol with higher alcohols (e.g., 1-butanol with $\varepsilon_r \approx 17$ at DC) or low-polarity solvents can reach $\varepsilon_r \approx 20$. In all cases, these liquids would be contained in sealed compartments or flexible bags to prevent direct contact and evaporation.

Another approach is coupling with a semi-solid or solid dielectric. This avoids liquid handling and simplifies the device. Rodriguez-Duarte *et al.* implemented a 24-antenna helmet using urethane rubber blocks loaded with graphite powder as the matching medium [24]. By adding conductive carbon powder to an elastic polymer, they achieved $\varepsilon_r \approx 18.3$ and $\sigma \approx 0.19$ S/m at 1 GHz . The resulting solid "matching bricks" conform to the head and embed the antennas, offering a repeatable helmet-like setup. Although the loss tangent of this composite exceeds our simulation medium (0.19 vs. 0.005 S/m), modest loss can help dampen spurious reflections and antenna mutual coupling while still preserving detectable signal levels. Other flexible gels (e.g., silicone or polyurethane loaded with ceramic or carbon-black powders) could be formulated to reach $\varepsilon_r \approx$ 15–25, providing a stable, encapsulated antenna environment while balancing permittivity and loss.

5.1.2 Antenna integration and performance

The dipole antenna array has to be integrated such that every antenna is essentially buried in the medium and near the head with the chosen matching medium. In the simulated model, dipole antennas were arranged around the cylinder at a radius of

Material / Mixture	Approx. ε_r @ 0.9 GHz	Approx. σ @ 0.9 GHz (S/m)
Distilled Water (reference)	~ 80	~ 1–2
Glycerin (99%+ pure)	~ 40–45	~ 1.0
Ethylene Glycol	~ 30–37	~ 0.1–0.2
Water–Alcohol Mix	~ 15–25	~ 0.01–0.05
Graphite–Rubber Composite	~ 18–20	~ 0.1–0.2

Table 5.1 : Potential matching medium materials at 0.9 GHz.

125 mm from the center, creating only a minimal gap between the antenna elements and the head phantom. A real system can accomplish this by either inserting antennas into the solid matching material itself or mounting them on the inner wall of the medium container—for a rigid construction. For example, in a liquid setup, each dipole might be sealed in a thin dielectric sleeve and submerged in the fluid, or conformal patch/monopole antennas could be laminated to the container's inner surface. In a solid matrix, antennas can be positioned precisely during dielectric block or cast fabrication to ensure close interaction with the medium [24]. The referenced 24-antenna prototype inserted printed monopole "brick" antennas into a rubber dielectric block [24]. Our design uses simple dipoles, realized as copper wire or PCB-printed elements fed via coaxial cables. Notably, an antenna immersed in a high-ε medium ($\varepsilon_r \approx 20$) experiences a shortened wavelength. A half-wave dipole at 900 MHz in free space is 16.7 cm long, but in $\varepsilon_r = 20$ medium the effective wavelength scales down by $\sqrt{20} \approx 4.5$. HFSS simulations show the dipole needs to be about 4.8 cm long to resonate in the matching medium. This shortening must be incorporated into the antenna design, and the feed matching network may require adjustment since the input impedance in dielectric loading differs from that in air.

5.1.3 Loss and noise considerations

Our algorithm (TSVD with differential imaging) proved quite sensitive to noise—the reconstructions were "usable but not always clear," especially when signals were weak. In a physical device, additional sources of noise will be present: *e.g.*, thermal noise from the medium and antennas, coupling among antennas, and instrument noise from the measurement electronics. The matching medium itself, if lossy, will attenuate signals and could reduce the dynamic range of received hemorrhage echoes. For instance, using a medium like glycerin ($\sigma \approx 1$ S/m) would dampen signals

considerably. A low-loss medium (like our ideal $\sigma = 0.005$ S/m, or a well-chosen alcohol mixture with minimal ionic content) is preferable for maximizing signal strength. That said, some loss (like the 0.1–0.2 S/m in a rubber composite) can be tolerated—and even beneficial in stabilizing the measurements—as long as the receive electronics are sufficiently sensitive. Modern microwave hardware can detect signals on the order of –100 dB relative to transmit power with a good vector network analyzer or low-noise receiver. In practice, one would use a *calibration procedure* and possibly a reference measurement channel to subtract out systematic errors [24]. To calibrate the system's phase and amplitude response, for instance, Rodriguez-Duarte et al. included spare antennas in a reference liquid [24]. Our differential imaging approach (comparing healthy vs. hemorrhage scenarios) inherently helps cancel common-mode errors, but a real system would still need to mitigate drift and multiple reflections. Time-gating or filtering could be applied to isolate early-time signals (from shallow interfaces) from later-time brain scattering, further cleaning up the data before image reconstruction.

5.1.4 Limitations and outlook

Finally, it's critical to acknowledge the limitations of the current work while preserving realistic hopes for real-world implementation. Since no physical testing has been done, all results are based on numerical modeling and algorithmic development only. As a result, effects like slight variations in dielectric characteristics, fabrication tolerances, and patient-to-patient variability are not noticed. The used TSVD method is known to be sensitive to model errors and measurement noise; in a real device, regularization parameters may need to be changed, or alternative reconstruction techniques (like iterative tomographic methods) may be used to control uncertainty. We purposefully chose a straightforward physical configuration (cylindrical symmetry, homogeneous matching medium) to facilitate the switch to a prototype. In a real-world scenario, the imaging model would be informed by precise measurements of the matching medium's ε_r and σ values, with material selection guided by the candidates listed in Table 5.1. After that, dipole antennas would be built to the appropriate size for that medium and verified (for example, using S11 reflection measurements) to guarantee correct tuning at 0.9 GHz Some performance trade-offs are expected; for instance, embedding

antennas in a high-ε medium can reduce radiation efficiency and bandwidth, although this is offset by much-improved coupling into the head. As is typical in through-wall or through-tissue microwave imaging, the system would likely require higher transmit power or longer integration times to compensate for weaker signals. Nonetheless, with careful design, the simulated system can be realized in hardware. A robust calibration procedure and a well-chosen matching medium—potentially a solid dielectric helmet for practicality—will enable this TSVD-based imaging array to operate in vivo. Future work will involve building such a medium and antenna array, then validating stroke detection performance in laboratory experiments. By iterating between modeling and measurement, the practical feasibility of microwave stroke imaging using this approach can be continually improved.

5.2 Realistic Constraints

Several practical restrictions that do not show up in idealized theory or in purely numerical investigations have emerged throughout the development of the differential microwave-imaging system.

5.2.1 Social, environmental and economic impact

A portable microwave unit might cut the time to diagnosis for stroke patients at regional hospitals, so clearly benefiting society. The method uses non-ionizing radiation, avoiding the safety and shielding problems associated with X-ray CT. The environmental footprint of the antennas is minimal, as they can be built from recyclable materials and consume very little power. Although initial build costs are high, per-scan costs should decline as equipment is amortized and clinical procedures improve. Because the technology is designed to augment rather than replace current imaging professionals, upskilling programs can help minimize any potential job disruptions.

5.2.2 Cost analysis

No physical components have been bought, and no clinical assessments have been performed, as the study has only been able to use software models thus far. Nevertheless, a rough budget frame aids in determining viability. A multi-port network analyzer that can do time-gated S-parameter measurements would be the

single biggest expense; according to market research, these devices are significantly more expensive than the typical student budget. The antenna array itself, which consists of 16 broadband dipoles, precision cables, and a basic switching matrix, is a second cost factor. The computational demand for HFSS and Python-based TSVD coding is already met by university workstations, and software is still reasonably priced under academic licensing. Labor is considered notionally: the cost of the RF gear would be comparable to the stipend of an entry-level engineer for a six-month equivalent work put in by each of the three team members. Although they are small in contrast, consumables including matching medium components, SMA connectors, and 3-D-printed fittings should be monitored for accuracy. Based on this, the project concept indicates that open-source technologies and the reuse of institutional equipment are essential for financial viability.

5.2.3 Standards

Although the present effort is limited to simulations, any prototype in the future has to follow generally accepted guidelines. When electromagnetic exposure arises, one should follow the power-density limits of IEEE C95.1. PCB layout and connector labeling should be done according to common RF design recommendations including IPC-2221. Should the equipment be classified as a medical system, IEC 60601-1—which is supplemented by standardized Turkish versions under TS EN—will take first priority as the safety standard. From a software standpoint, the group tracks all code changes in a version-control repository and follows ISO/IEC 29110's lightweight documentation rules for small technical teams. The basis for ethical compliance—that is, a formal pledge to obtain institutional permission before acquiring any human data—is the IEEE Code of Ethics.

5.2.4 Health and safety concerns

While health hazards are fictional during the simulation phase, a responsible design culture addresses them before hand. Radio frequency exposure will be kept much below IEEE C95.1's whole-head specific-absorption limits; once physical testing begins, compliance can be verified with a handheld field probe. The antenna carrier, which looks like a helmet, should have its sharp edges softened and padded if one

wants to protect skin and hair. Essential for electrical safety are using approved power sources and including over-current protection to every measuring channel. Although hygiene guidelines are not yet set, scan sessions can be short to minimize patient discomfort and any future touch surfaces can be specified in widely sterile plastics. Once these broad safety issues have been taken care of, there is a sensible basis for the forthcoming development cycle when physical hardware replaces numerical models.

5.3 Future Work and Recommendations

Large improvements in non-invasive medical diagnostics are grounded in the proposed microwave imaging of the brain hemorrhage system. The antenna array design will be expanded beyond by investigating other antenna designs, such miniature Vivaldi antennas, which can maximize signal penetration and minimize artifacts in reconstructed images [26] will also be part of it. Furthermore crucial for efficient signal transmission and reception in a range of clinical settings is additional optimization of the matching medium. This can be achieved by applying machine learning techniques to design matching medium. CNN and MLP methods can predict the optimal matching medium permittivity for any combination of antenna and tissue. This will drastically reduce the numerical sweep steps which are slow and inefficient. [27].

Another crucial direction of development to improve computational efficiency and diagnostic accuracy even more is including more complex machine learning models into the reconstruction process. This can reduce the noise effects due to TSVD algorithm and improve the reliability of the imaging algorithm. Integration with portable, bedside-compatible hardware will also be a top priority of the system in order to help to further fulfill the project's aim of access and real-time monitoring. Compact hardware solutions that can control imaging computational load and ensure patient safety will take precedence in development [28].

In order to increase microwave penetration, in the future, flexible conformal antenna arrays can be employed to the imaging system. Employing conformal antenna elements that make up a 360° would improve coupling and minimize mismatches due to patient difference [29].

Research of multi-modal imaging methods, such microwave imaging mixed with ultrasonic waves, might enhance diagnostics even more. By means of adaptive algorithms and iterative learning approaches, future works will also address the issues including noise sensitivity and patient-specific variability. The improvements will increase the system's resilience and adaptability to identify and track hemorrhagic conditions, so rendering it clinically acceptable and generally practical in emergency and critical care environments.

6. CONCLUSION

In this work, entirely in a simulation environment, the feasibility of a portable, low-cost microwave imaging system for the detection and monitoring of intracranial hemorrhages has been shown. The system produced differential multistatic S-parameter data representing both healthy and hemorrhagic conditions inside a realistic head phantom by using a circular array of sixteen dipole antennas optimized at 900 MHz together with a well designed matching medium. Born-approximation-based linearization and subsequent Truncated Singular Value Decomposition (TSVD) regularization enabled stable and interpretable image reconstructions, effectively suppressing noise and emphasizing the dominant contrast features.

Results revealed that, even for small and deeply located lesions, the proposed pipeline can localize hemorrhagic foci with great accuracy and clarity under idealized lossless conditions. But when realistic tissue conductivity was added, the microwave signal experienced notable attenuation, so lowering image contrast and complicating the reliable diagnosis of smaller or deeper lesions. Still, the general spatial localization of hemorrhagic areas stayed reasonable, which emphasizes the possible clinical relevance of the method for gross lesion monitoring.

Five clinically inspired scenarios were methodically assessed to show that under both lossless and lossy conditions the technique can differentiate between several patterns of hemorrhagic progression, enlargement, and multiplicity. Supported by suitable regularization and signal preprocessing, evaluations of the rebuilt images confirm the stability of the TSVD-based inversion method.

It is important to acknowledge that the findings are based entirely on numerical simulations and algorithmic development. Although this phase did not address real-world confusing variables including dielectric-property variations, fabrication tolerances, and inter-patient variability, the present results give a strong basis for next experimental validation. Furthermore, methodological decisions, including the use of a homogeneous phantom, cylindrical symmetry, and an interactive TSVD cutoff

interface, were deliberately chosen to simplify algorithm verification and enable a clear transition to prototype development.

In general, differential microwave imaging based on optimal antenna arrays and TSVD regularization provides a promising, fast, and low-cost method for the detection and monitoring of intracranial hemorrhages within the limitations of simulation. Future hardware realization as well as experimental research will benefit much from the insights and benchmarks developed here.

REFERENCES

[1] **Dilman, , Yıldırım, U., Coşğun, S., Doğu, S., Çayören, M. and Akduman, I.** Feasibility of brain stroke imaging with microwaves, *2016 IEEE Asia-Pacific Conference on Applied Electromagnetics (APACE)*, IEEE, pp.334–338.

[2] **Bisio, I., Estatico, C., Fedeli, A., Lavagetto, F., Pastorino, M., Randazzo, A. and Sciarrone, A.** Variable-exponent lebesgue-space inversion for brain stroke microwave imaging, *IEEE Transactions on Microwave Theory and Techniques*, *68*(5), 1882–1895.

[3] **Dilman, , Bilgin, E., Akıncı, M.N.** *et al.* Monitoring of intracerebral hemorrhage with a linear microwave imaging algorithm, *Medical & Biological Engineering & Computing*, *61*, 33–43.

[4] **Scapaticci, R., Bucci, O.M., Catapano, I. and Crocco, L.** Differential Microwave Imaging for Brain Stroke Followup, *International Journal of Antennas and Propagation*, Article ID 312528.

[5] **Çayören, M. and Akduman, ,** Continuous monitoring of hemorrhagic strokes via differential microwave imaging, **L. Crocco**, **I. Karanasiou**, **M. James and R. Conceição**, editors, Emerging Electromagnetic Technologies for Brain Diseases Diagnostics, Monitoring and Therapy, Springer, Cham.

[6] **EM Software & Systems-SA (Pty) Ltd.**, FEKO: The Power of Multiple Solvers, Stellenbosch, South Africa, april 14, 2014.

[7] **ANSYS, Inc.**, ANSYS HFSS User's Guide.

[8] **Topsakal, E., Karacolak, T. and Moreland, E.C.** Glucose-dependent dielectric properties of blood plasma, *2011 XXXth URSI General Assembly and Scientific Symposium*, Istanbul, Turkey, pp.1–4.

[9] **Gabriel, S., Lau, R.W. and Gabriel, C.** The dielectric properties of biological tissues: III. Parametric models for the dielectric spectrum of tissues, *Physics in Medicine and Biology*, *41*(11), 2271–2293.

[10] **Pastorino, M.** *Microwave Imaging*, Wiley, Hoboken, N.J.

[11] **Colton, D., Kirsch, A. and Monk, P.**, The Linear Sampling Method in Inverse Scattering Theory, **D. Colton**, **H.W. Engl**, **A.K. Louis**, **J.R. McLaughlin and W. Rundell**, editors, Surveys on Solution Methods for Inverse Problems, Springer, Vienna.

[12] **Magdum, A. and Erramshetty, M.** Distorted Born iterative method with back-propagation improves permittivity reconstruction, *International Journal of Microwave and Wireless Technologies*, *15*(2), 331–337.

[13] **Shan, T.**, **Lin, Z.**, **Song, X.**, **Li, M.**, **Yang, F. and Xu, S.** Neural Born Iterative Method for Solving Inverse Scattering Problems: 2D Cases, *IEEE Transactions on Antennas and Propagation*, *71*(1).

[14] **Pastorino, M.** Stochastic Optimization Methods Applied to Microwave Imaging: A Review, *IEEE Transactions on Antennas and Propagation*, *55*(3), 538–548.

[15] **Sachs, J.**, **Ley, S.**, **Just, T.**, **Chamaani, S. and Helbig, M.** Differential Ultra-Wideband Microwave Imaging: Principle Application Challenges, *Sensors*, *18*, 2136.

[16] **Jauch, E.C.** *et al.* Guidelines for the early management of patients with acute ischemic stroke: a guideline for healthcare professionals from the American Heart Association/American Stroke Association, *Stroke*, *44*(3), 870–947.

[17] **Semenov, S.** *et al.* Dielectrical spectroscopy of canine myocardium during acute ischemia and hypoxia at frequency spectrum from 100 kHz to 6 GHz, *IEEE Transactions on Medical Imaging*, *21*, 703–707.

[18] **Wang, Y.M. and Chew, W.C.**, Reconstruction of Two-Dimensional Refractive Index Distribution Using the Born Iterative and Distorted Born Iterative Method, **H. Lee and G. Wade**, editors, Acoustical Imaging, vol. 18, Springer, Boston, MA.

[19] **Bertero, M. and Boccacci, P.** *Introduction to Inverse Problems in Imaging*, Institute of Physics, Bristol, UK.

[20] **Noschese, S. and Reichel, L.** A modified truncated singular value decomposition method for discrete ill-posed problems, *Numerical Linear Algebra with Applications*, *21*(6), 813–822.

[21] **Dogu, S.**, **Alidoustaghdam, H.**, **Dilman, and Akinci, M.N.** The Capability of Truncated Singular Value Decomposition Method for through the Wall Microwave Imaging, ***A. Aboltins and A. Litvinenko****, editors, Proceedings of 2020 IEEE Workshop on Microwave Theory and Techniques in Wireless Communications, MTTW 2020*, Institute of Electrical and Electronics Engineers Inc., pp.76–81.

[22] **Richmond, J.** Scattering by a dielectric cylinder of arbitrary cross section shape, *IEEE Transactions on Antennas and Propagation*, *13*, 334–341.

[23] **Shao, W. and Zhou, B.** Effect of Coupling Medium on Penetration Depth in Microwave Medical Imaging, *Diagnostics*, *12*(12), 2906.

[24] **Rodriguez-Duarte, D.O.**, **Vasquez, J.A.T.**, **Scapaticci, R.**, **Turvani, G.**, **Cavagnaro, M.**, **Casu, M.R.**, **Crocco, L. and Vipiana, F.** Experimental Validation of a Microwave System for Brain Stroke 3-D Imaging, *Diagnostics*, *11*(7), 1232.

[25] **Lui, H.S. and Fhager, A.** On the Matching Medium for Microwave Stroke Diagnosis, *Biomedical Physics & Engineering Express*, *5*(4), 045034.

[26] **Zhang, W.**, **Xie, J.**, **Somjit, N.** *et al.*, Design and Optimization of Miniaturized Co-planar Vivaldi Antennas for Enhanced Microwave Imaging in Brain Hemorrhage Detection, preprint, Research Square.

[27] **Cil, E.**, **Cadir, C.**, **Kati, O.A.**, **Yilmaz, H.B. and Dumanli, S.** Machine Learning-Based Matching Medium Design for Implant Communications, *IEEE Transactions on Antennas and Propagation*, *70*(7), 5199–5208.

[28] **Li, Q.** *et al.* A Portable Microwave Intracranial Hemorrhage Imaging System Based on PSO-MCKD-CEEMDAN Method, *IEEE Transactions on Microwave Theory and Techniques*, *71*(2), 773–783.

[29] **Alqadami, A.S.M.**, **Nguyen-Trong, N.**, **Mohammed, B.**, **Stancombe, A.E.**, **Heitzmann, M.T. and Abbosh, A.** Compact Unidirectional Conformal Antenna Based on Flexible High-Permittivity Custom-Made Substrate for Wearable Wideband Electromagnetic Head Imaging System, *IEEE Transactions on Antennas and Propagation*, *68*(1), 183–194.

APPENDIX A.1 : Python script used in the TSVD example application.
APPENDIX A.2 : Python script used in the final TSVD part.

7. APPENDICES

APPENDIX A.1

```
import numpy as np
import matplotlib.pyplot as plt
from sklearn.decomposition import TruncatedSVD
from skimage import data, color, img_as_float
from skimage.io import imread

# Step 1: Load and preprocess an image
image = imread('/Users/burakerdilbicer/Desktop/Python Files/TSVD_deneme/IMG_5571.JPG')
image_gray = color.rgb2gray(image)  # Convert the image to grayscale
image_matrix = img_as_float(image_gray)  # Convert to floating point values

# Reshape the image matrix to 2D array for TSVD
height, width = image_matrix.shape
image_2d = image_matrix.reshape((height, width))

# Step 2: Apply Truncated SVD (TSVD)
#n_components = min(50, min(height, width))
n_components = min(height, width)
tsvd = TruncatedSVD(n_components=n_components)
image_matrix_tsvd = tsvd.fit_transform(image_2d)
image_reconstructed = tsvd.inverse_transform(image_matrix_tsvd)

# Reshape back to original dimensions
image_reconstructed = image_reconstructed.reshape((height, width))

# Plot singular values
singular_values = tsvd.singular_values_
plt.figure(figsize=(8, 4))
plt.plot(singular_values, 'o-', label='Singular Values')
plt.title('Singular Values')
plt.xlabel('Index')
plt.ylabel('Value')
plt.grid(True)
plt.legend()
plt.show()

# Step 3: Display original and reconstructed images with different thresholds
thresholds = [5, 10, 20, 30, 40]  # Different numbers of singular values to keep
fig, axes = plt.subplots(1, len(thresholds) + 1, figsize=(15, 6))

# Original image
axes[0].imshow(image_matrix, cmap='gray')
axes[0].set_title('Original Image')
axes[0].axis('off')

# Reconstructed images with different thresholds
for i, threshold in enumerate(thresholds):
    tsvd = TruncatedSVD(n_components=threshold)
    image_matrix_tsvd = tsvd.fit_transform(image_2d)
    image_reconstructed = tsvd.inverse_transform(image_matrix_tsvd)
    image_reconstructed = image_reconstructed.reshape((height, width))

    axes[i + 1].imshow(image_reconstructed, cmap='gray')
    axes[i + 1].set_title(f'{threshold} Components')
    axes[i + 1].axis('off')

plt.tight_layout()
plt.show()
```

Listing 7.1: Python script used in the TSVD example application.

APPENDIX A.2

```
# Microwave imaging for brain hemorrhage detection using TSVD reconstruction
# Features: Interactive sliders, noise filtering, elliptical skull masking

import numpy as np
import matplotlib.pyplot as plt
from matplotlib.widgets import Slider
from matplotlib.patches import Ellipse
from scipy.special import hankel2, jv
from scipy.linalg import svd
from scipy import ndimage
from scipy.ndimage import binary_opening, binary_closing, label
from skimage.morphology import disk
from skimage.filters import gaussian
import skrf as rf

# Utility functions
def load_s_parameters(filename: str) -> np.ndarray:
    """Load S-parameters from .s16p file."""
    return rf.Network(filename).s


def create_mesh_grid(size: float = 0.3, points: int = 32):
    """Create square mesh grid for imaging domain."""
    x = np.linspace(-size / 2, size / 2, points)
    y = np.linspace(-size / 2, size / 2, points)
    xx, yy = np.meshgrid(x, y)
    return x, y, xx, yy, np.column_stack((xx.ravel(), yy.ravel()))


def antenna_positions(radius: float = 0.125, n: int = 16) -> np.ndarray:
    """Generate antenna coordinates in circular array."""
    phi = np.linspace(0, 2 * np.pi * (1 - 1 / n), n)
    return np.column_stack((radius * np.cos(phi), radius * np.sin(phi)))


def green_function(k0: float, r: np.ndarray) -> np.ndarray:
    """2D scalar Green's function using Hankel function."""
    return (1 / (4j)) * hankel2(0, k0 * r)


def calculate_L_matrix(
    mesh_pts: np.ndarray, ant_pos: np.ndarray, k0: float, delta_z: complex
) -> np.ndarray:
    """Build forward operator matrix for all Tx-Rx pairs."""
    n_ant, n_mesh = len(ant_pos), len(mesh_pts)
    L = np.empty((n_ant * n_ant, n_mesh), dtype=np.complex128)

    row = 0
    for tx in ant_pos:
        for rx in ant_pos:
            r_tx = np.linalg.norm(mesh_pts - tx, axis=1)
            r_rx = np.linalg.norm(mesh_pts - rx, axis=1)
            L[row] = (k0**2) * green_function(k0, r_tx) * green_function(k0, r_rx) ...
            ... * delta_z
            row += 1
    return L


def tsvd_invert(
    U: np.ndarray,
    S: np.ndarray,
    Vh: np.ndarray,
    us: np.ndarray,
    n_keep: int,
) -> np.ndarray:
    """
```

```
    Truncated SVD inversion using largest n_keep singular values.
    """
    n_keep = int(np.clip(n_keep, 1, len(S)))
    S_inv = np.zeros_like(S)
    S_inv[:n_keep] = 1.0 / S[:n_keep]
    return Vh.conj().T @ (S_inv * (U.conj().T @ us))


def apply_noise_filtering(
    image: np.ndarray,
    threshold_percentile: float = 85.0,
    gaussian_sigma: float = 1.2,
    morph_disk_size: int = 3,
    min_component_size: int = 30,
    keep_largest_only: bool = True
) -> np.ndarray:
    """
    Apply noise filtering to enhance hemorrhage detection.

    Args:
        threshold_percentile: Keep only pixels above this percentile
        gaussian_sigma: Gaussian smoothing parameter
        morph_disk_size: Size of morphological operations
        min_component_size: Minimum size of connected components
        keep_largest_only: Keep only the largest connected component
    """
    # Gaussian smoothing to reduce noise
    if gaussian_sigma > 0:
        filtered_image = gaussian(image, sigma=gaussian_sigma, preserve_range=True)
    else:
        filtered_image = image.copy()

    # Threshold based on percentile
    if threshold_percentile > 0:
        threshold_value = np.percentile(filtered_image[filtered_image > 0], ...
                                        ... threshold_percentile)
        binary_mask = filtered_image >= threshold_value
    else:
        binary_mask = filtered_image > 0

    # Morphological operations for cleanup
    if morph_disk_size > 0:
        struct_elem = disk(morph_disk_size)
        binary_mask = binary_opening(binary_mask, structure=struct_elem)
        binary_mask = binary_closing(binary_mask, structure=struct_elem)

    # Connected component analysis
    if min_component_size > 0 or keep_largest_only:
        labeled_array, num_features = label(binary_mask)
        component_sizes = ndimage.sum(binary_mask, labeled_array, ...
                                      ... range(num_features + 1))

        if keep_largest_only and num_features > 0:
            largest_component_label = np.argmax(component_sizes[1:]) + 1
            binary_mask = labeled_array == largest_component_label
        else:
            large_components = component_sizes >= min_component_size
            binary_mask = large_components[labeled_array]

    # Apply cleaned mask to filtered image
    result = filtered_image.copy()
    result[~binary_mask] = 0

    return result


def main(
    s_file_empty: str,
    s_file_bleed: str,
    freq_idx: int = 0,
    n_keep: int = 50,
    grid_size: float = 0.3,
    n_grid_pts: int = 128,
    n_antennas: int = 16,
```

```
    ant_radius: float = 0.125,
    freq_hz: float = 0.9e9,
) -> None:
    """Main microwave imaging routine with interactive visualization."""

    # Physical constants
    wavelength = 3e8 / freq_hz
    k0 = 2 * np.pi / wavelength

    # Setup imaging domain and antennas
    _, _, _, _, mesh_pts = create_mesh_grid(grid_size, n_grid_pts)
    dx = dy = grid_size / n_grid_pts
    a = np.sqrt(dx * dy / np.pi)
    delta_z = 1j * np.pi * k0 * a * jv(0, k0 * a)
    ant_pos = antenna_positions(ant_radius, n_antennas)

    # Load S-parameters
    s_empty = load_s_parameters(s_file_empty)
    s_bleed = load_s_parameters(s_file_bleed)
    us = (s_bleed[freq_idx] - s_empty[freq_idx]).ravel()

    # Forward operator and SVD
    L = calculate_L_matrix(mesh_pts, ant_pos, k0, delta_z)
    U, S, Vh = svd(L, full_matrices=False)

    # Initial TSVD reconstruction
    chi = tsvd_invert(U, S, Vh, us, n_keep=n_keep)
    chi_real = chi.real.reshape(n_grid_pts, n_grid_pts)
    chi_imag = chi.imag.reshape(n_grid_pts, n_grid_pts)
    chi_mag = np.abs(chi).reshape(n_grid_pts, n_grid_pts)

    # Normalize magnitude to [0, 1]
    chi_mag_max = chi_mag.max()
    if chi_mag_max > 0:
        chi_mag_normalized = chi_mag / chi_mag_max
    else:
        chi_mag_normalized = chi_mag

    # Apply coordinate transformations
    chi_mag_normalized = np.rot90(chi_mag_normalized, 2)  # 180-degree rotation
    chi_mag_normalized = chi_mag_normalized.T  # Swap x-y coordinates
    chi_mag_normalized = np.flipud(chi_mag_normalized)  # Flip vertically

    # Create elliptical skull mask
    skull_radius_x = 0.10  # Horizontal radius
    skull_radius_y = 0.08  # Vertical radius

    x_coords = np.linspace(-grid_size / 2, grid_size / 2, n_grid_pts)
    y_coords = np.linspace(-grid_size / 2, grid_size / 2, n_grid_pts)
    X, Y = np.meshgrid(x_coords, y_coords)

    ellipse_distance = (X**2 / skull_radius_x**2) + (Y**2 / skull_radius_y**2)
    skull_mask = ellipse_distance <= 1.0

    # Apply skull mask
    chi_mag_skull = chi_mag_normalized.copy()
    chi_mag_skull[~skull_mask] = 0

    # Apply noise filtering
    chi_mag_filtered = apply_noise_filtering(
        chi_mag_skull,
        threshold_percentile=85.0,
        gaussian_sigma=1.2,
        morph_disk_size=3,
        min_component_size=30,
        keep_largest_only=True
    )

    # Display singular value spectrum
    fig_sv, ax_sv = plt.subplots(figsize=(10, 6))

    ax_sv.plot(S, marker="o", markersize=4, linewidth=1.5, color='blue')
    vline = ax_sv.axvline(n_keep - 1, color="red", linestyle="--", ...
                          ... linewidth=2, label=f"n_keep = {n_keep}")
```

```
ax_sv.set_xlabel("Singular-value index", fontsize=12)
ax_sv.set_ylabel(" (linear scale)", fontsize=12)
ax_sv.set_title("Singular-value spectrum", fontsize=14)
ax_sv.grid(True, alpha=0.3)
ax_sv.legend(fontsize=11)

plt.tight_layout()
plt.show()

# Setup interactive reconstruction plots
plt.close("all")
fig, (ax1, ax2, ax3) = plt.subplots(1, 3, figsize=(20, 6))
plt.subplots_adjust(bottom=0.25)

default_vmax = 0.9
vmax_init = default_vmax

# Original reconstruction
im1 = ax1.imshow(
    chi_mag_normalized,
    extent=[-grid_size / 2, grid_size / 2, -grid_size / 2, grid_size / 2],
    origin='lower',
    cmap="jet",
    vmin=0.0,
    vmax=vmax_init,
)
ax1.set_title("TSVD || - Original")
ax1.set_xlabel("x (m)")
ax1.set_ylabel("y (m)")
plt.colorbar(im1, ax=ax1)
ellipse1 = Ellipse((0, 0), width=2*skull_radius_x, height=2*skull_radius_y,
                   fill=False, linestyle="--", color="white", linewidth=2)
ax1.add_artist(ellipse1)

# Skull-masked reconstruction
im2 = ax2.imshow(
    chi_mag_skull,
    extent=[-grid_size / 2, grid_size / 2, -grid_size / 2, grid_size / 2],
    origin='lower',
    cmap="jet",
    vmin=0.0,
    vmax=vmax_init,
)
ax2.set_title("TSVD || - Skull Region Only")
ax2.set_xlabel("x (m)")
ax2.set_ylabel("y (m)")
plt.colorbar(im2, ax=ax2)
ellipse2 = Ellipse((0, 0), width=2*skull_radius_x, height=2*skull_radius_y,
                   fill=False, linestyle="--", color="white", linewidth=2)
ax2.add_artist(ellipse2)

# Filtered reconstruction
im3 = ax3.imshow(
    chi_mag_filtered,
    extent=[-grid_size / 2, grid_size / 2, -grid_size / 2, grid_size / 2],
    origin='lower',
    cmap="jet",
    vmin=0.0,
    vmax=vmax_init,
)
ax3.set_title("TSVD || - Noise Filtered")
ax3.set_xlabel("x (m)")
ax3.set_ylabel("y (m)")
plt.colorbar(im3, ax=ax3)
ellipse3 = Ellipse((0, 0), width=2*skull_radius_x, height=2*skull_radius_y,
                   fill=False, linestyle="--", color="white", linewidth=2)
ax3.add_artist(ellipse3)

# Interactive sliders
ax_vmax = plt.axes([0.25, 0.12, 0.5, 0.03])
vmax_slider = Slider(
    ax=ax_vmax,
    label="vmax (colour-bar upper limit)",
    valmin=0.0,
```

```
        valmax=1.0,
        valinit=vmax_init,
    )

    ax_cut = plt.axes([0.25, 0.05, 0.5, 0.03])
    cut_slider = Slider(
        ax=ax_cut,
        label="n_keep (TSVD cut-off)",
        valmin=1,
        valmax=len(S),
        valinit=n_keep,
        valstep=1,
    )

    # Slider callback functions
    def update_vmax(val):
        im1.set_clim(vmin=0.0, vmax=vmax_slider.val)
        im2.set_clim(vmin=0.0, vmax=vmax_slider.val)
        im3.set_clim(vmin=0.0, vmax=vmax_slider.val)
        fig.canvas.draw_idle()

    def update_cutoff(val):
        new_n_keep = int(cut_slider.val)

        # Perform new TSVD reconstruction
        chi_new = tsvd_invert(U, S, Vh, us, n_keep=new_n_keep)

        # Process new reconstruction
        chi_new_mag = np.abs(chi_new).reshape(n_grid_pts, n_grid_pts)
        chi_new_max = chi_new_mag.max()
        if chi_new_max > 0:
            chi_new_normalized = chi_new_mag / chi_new_max
        else:
            chi_new_normalized = chi_new_mag

        # Apply same coordinate transformations
        chi_new_normalized = np.rot90(chi_new_normalized, 2)
        chi_new_normalized = chi_new_normalized.T
        chi_new_normalized = np.flipud(chi_new_normalized)

        # Create updated skull mask
        x_coords = np.linspace(-grid_size / 2, grid_size / 2, n_grid_pts)
        y_coords = np.linspace(-grid_size / 2, grid_size / 2, n_grid_pts)
        X, Y = np.meshgrid(x_coords, y_coords)
        ellipse_distance_updated = (X**2 / skull_radius_x**2) + (Y**2 / ...
                                            ... skull_radius_y**2)
        skull_mask_updated = ellipse_distance_updated <= 1.0

        # Apply skull mask and filtering
        chi_new_skull = chi_new_normalized.copy()
        chi_new_skull[~skull_mask_updated] = 0

        chi_new_filtered = apply_noise_filtering(
            chi_new_skull,
            threshold_percentile=85.0,
            gaussian_sigma=1.2,
            morph_disk_size=3,
            min_component_size=30,
            keep_largest_only=True
        )

        # Update plot data
        im1.set_data(chi_new_normalized)
        im2.set_data(chi_new_skull)
        im3.set_data(chi_new_filtered)

        # Update singular value plot
        vline.set_xdata([new_n_keep - 1, new_n_keep - 1])
        vline.set_label(f"n_keep = {new_n_keep}")
        ax_sv.legend(loc="best")

        fig_sv.canvas.draw_idle()
        fig.canvas.draw_idle()
```

```
    def on_plot_click(event):
        """Click event handler to normalize vmax value."""
        if event.inaxes in [ax1, ax2, ax3]:
            normalized_vmax = 1

            vmax_slider.set_val(normalized_vmax)

            im1.set_clim(vmin=0.0, vmax=normalized_vmax)
            im2.set_clim(vmin=0.0, vmax=normalized_vmax)
            im3.set_clim(vmin=0.0, vmax=normalized_vmax)
            fig.canvas.draw_idle()

            print(f"Clicked! vmax normalized to: {normalized_vmax}")

    # Connect slider callbacks
    vmax_slider.on_changed(update_vmax)
    cut_slider.on_changed(update_cutoff)
    fig.canvas.mpl_connect('button_press_event', on_plot_click)

    plt.show()


# Main execution
if __name__ == "__main__":
    # Test files - uncomment the pair you want to usE

    s_file_empty = "1_noblood.s16p"
    s_file_bleed = "1_leftbottom.s16p"

    # Run imaging analysis
    for freq_idx in [0]:
        for n_keep in [52]:
            print(f"Processing with freq_idx={freq_idx}, n_keep={n_keep}")
            main(
                s_file_empty=s_file_empty,
                s_file_bleed=s_file_bleed,
                freq_idx=freq_idx,
                n_keep=n_keep,
            )
```

Listing 7.2: Python script used in the final TSVD part.

CURRICULUM VITAE

Name Surname: Burak Erdil Biçer

Place and Date of Birth: Altındağ, 21/07/2002

E-Mail: bicerb20@itu.edu.tr

EDUCATION:

- **B.Sc.:** 2025 (expected), Istanbul Technical University, Faculty of Electrical and Electronics Engineering, Electronics and Communication Engineering
- **B.Sc.:** 2025 (expected), Istanbul Technical University, Faculty of Aeronautics and Astronautics, Aeronautical Engineering (Double Major)

PROFESSIONAL EXPERIENCE:

- ITU Aerospace Research Center (ITU ARC) *Sep 2024 – Jun 2025*
- Baykar Technologies *Aug 2023 - Sep 2023*
- ASELSAN *Jun 2023 - Jul 2023*
- Bountenna Antennas & Propagation Research Laboratory *Nov 2022 - Jun 2023*
- Turkish Aerospace (TUSAŞ) *Nov 2022 - May 2023*

Name Surname: Nahid Gudratli

Place and Date of Birth: Aghdam, 02/09/2003

E-Mail: gudratli20@itu.edu.tr

EDUCATION:

- **B.Sc.:** 2025 (expected), Istanbul Technical University, Faculty of Electrical and Electronics Engineering, Electronics and Communication Engineering

PROFESSIONAL EXPERIENCE:

- Azerconnect Group (Packet Switching Team) *Aug 2024 - Oct 2024*
- Information and Communication Tech. Agency (ICTA) *Jul 2024 - Aug 2024*

Name Surname: Vurghun Ahmadov

Place and Date of Birth: Sabirabad, 01/01/2004

E-Mail: ahmadov21@itu.edu.tr

EDUCATION:

- **B.Sc.:** 2025 (expected), Istanbul Technical University, Faculty of Electrical and Electronics Engineering, Electronics and Communication Engineering

PROFESSIONAL EXPERIENCE:

- ITU Wireless Communication Research Laboratory *Apr 2025 - May 2025*
- Azercosmos LLC (RF and Antenna Unit) *Jan 2025 - Feb 2025*
- Smart Solutions Group *July 2024 - Aug 2024*